GEOMECHANICAL STUDIES
OF THE BARNETT SHALE, TEXAS, USA

A DISSERTATION
SUBMITTED TO THE DEPARTMENT OF GEOPHYSICS
AND THE COMMITTEE ON GRADUATE STUDIES
OF STANFORD UNIVERSITY
IN PARTIAL FULFILLMENT OF THE REQUIREMENTS
FOR THE DEGREE OF
DOCTOR OF PHILOSOPHY

SRB VOLUME 125

John P. Vermylen

May 2011

John P. Vermylen

I certify that I have read this dissertation and that, in my opinion, it is fully adequate in scope and quality as a dissertation for the degree of Doctor of Philosophy.

_____

Mark D. Zoback (Principal Adviser

I certify that I have read this dissertation and that, in my opinion, it is fully adequate in scope and quality as a dissertation for the degree of Doctor of Philosophy.

_____

Gregory Beroza

I certify that I have read this dissertation and that, in my opinion, it is fully adequate in scope and quality as a dissertation for the degree of Doctor of Philosophy.

_____

Anthony Kovscek

Approved for the Stanford University Committee on Graduate Studies.

_____

ABSTRACT

This thesis presents five studies of a gas shale reservoir using diverse methodologies to investigate geomechanical and transport properties that are important across the full reservoir lifecycle. Using the Barnett shale as a case study, we investigated adsorption, permeability, geomechanics, microseismicity, and stress evolution in two different study areas. The main goals of this thesis can be divided into two parts: first, to investigate how flow properties evolve with changes in stress and gas species, and second, to understand how the interactions between stress, fractures, and microseismicity control the creation of a permeable reservoir volume during hydraulic fracturing.

In Chapter 2, we present results from adsorption and permeability experiments conducted on Barnett shale rock samples. We found Langmuir-type adsorption of CH_4 and N_2 at magnitudes consistent with previous studies of the Barnett shale. Three of our samples demonstrated BET-type adsorption of CO_2, in contrast to all previous studies on CO_2 adsorption in gas shales, which found Langmuir-adsorption. At low pressures (600 psi), we found preferential adsorption of CO_2 over CH_4 ranging from 3.6x to 5.5x. While our measurements were conducted at low pressures (up to 1500 psi), when our model fits are extrapolated to reservoir pressures they reach similar adsorption magnitudes as have been found in previous studies. At these high reservoir pressures, the very large preferential adsorption of CO_2 over CH_4 (up to 5-10x) suggests a significant potential for CO_2 storage in gas shales like the Barnett if practical problems of injectivity and matrix transport can be overcome.

We successfully measured permeability versus effective stress on two intact Barnett shale samples. We measured permeability effective stress coefficients less than 1 on both samples, invalidating our hypothesis that there might be throughgoing flow paths within the soft, porous organic kerogen that would lead the permeability effective stress coefficient to be greater than 1. The results suggest that microcracks are likely the dominant flow paths at these scales.

In Chapter 3, we present integrated geological, geophysical, and geomechanical data in order to characterize the rock properties in our Barnett shale study area and to

model the stress state in the reservoir before hydraulic fracturing occurred. Five parallel, horizontal wells were drilled in the study area and then fractured using three different techniques. We used the well logs from a vertical pilot well and a horizontal well to constrain the stress state in the reservoir. While there was some variation along the length of the well, we were able to determine a best fit stress state of $P_P = 0.48$ psi/ft, $S_V = 1.1$ psi/ft, $S_{Hmax} = 0.73$ psi/ft, and $S_{hmin} = 0.65$ psi/ft. Applying this stress state to the mapped natural fractures indicates that there is significant potential for induced shear slip on natural fracture planes in this region of the Barnett, particularly close to the main hydraulic fracture where the pore pressure increase during hydraulic fracturing is likely to be very high.

In Chapter 4, we present new techniques to quantify the robustness of hydraulic fracturing in gas shale reservoirs. The case study we analyzed involves five parallel horizontal wells in the Barnett shale with 51 frac stages. To investigate the numbers, sizes, and types of microearthquakes initiated during each frac stage, we created Gutenberg-Richter-type magnitude distribution plots to see if the size of events follows the characteristic scaling relationship found in natural earthquakes. We found that slickwater fracturing does generate a log-linear distribution of microearthquakes, but that it creates proportionally more small events than natural earthquake sources. Finding considerable variability in the generation of microearthquakes, we used the magnitude analysis as a proxy for the "robustness" of the stimulation of a given stage. We found that the conventionally fractured well and the two alternately fractured wells ("zipperfracs") were more effective than the simultaneously fractured wells ("simulfracs") in generating microearthquakes. We also found that the later stages of fracturing a given well were more successful in generating microearthquakes than the early stages.

In Chapter 5, we present estimates of stress evolution in our study reservoir through analysis of the instantaneous shut-in pressure (ISIP) at the end of each stage. The ISIP increased stage by stage for all wells, but the simulfrac wells showed the greatest increase and the zipperfrac wells the least. We modeled the stress increase in the reservoir with a simple sequence of 2-D cracks along the length of the well. When using a spacing of one crack per stage, the modeled stress increase was nearly identical to the

measured stress increase in the zipperfrac wells. When using three cracks per stage, the modeled final stage stress magnitude matched the measured final stage stress magnitude from the simulfrac wells, but the rate of stress increase in the simulfrac wells was much more gradual than the model predicted.

To further investigate the causes of these ISIP trends, we began numerical flow and stress analysis to more realistically model the processes in the reservoir. One of our hypotheses was that the shorter total time needed to complete all the stages of the simulfrac wells was the cause of the greater ISIP increase compared to the zipperfrac wells. The microseismic activity level measured in Chapter 4 also correlates with total length of injection, suggesting leak off into the reservoir encouraged shear failure. Numerical modeling using the coupled FEM and flow software GEOSIM was able to model some cumulative stress increase the reservoir, but the full trend was not replicated. Further work to model field observations of hydraulic fracturing will enhance our understanding of the impact that hydraulic fracturing and stress change have on fracture creation and permeability enhancement in gas shales.

ACKNOWLEDGEMENTS

I would like to thank my adviser, Mark Zoback, for helping me follow my own path at Stanford. His support allowed me to experiment until I found the right place for me in science. It was a pleasure collaborating and problem solving with Mark. His emphasis to keep things simple and focused on the big picture will remain an inspiration.

Gregory Beroza, Peter Hennings, and Anthony Kovscek deserve great thanks for their guidance and insight as members of my dissertation committee. It was a pleasure working with them in so many different ways: as part of my committee, in classes at Stanford, and as colleagues in research. I would like to especially acknowledge Peter Hennings for the rock samples, well logs, and microseismic data that ConocoPhillips provided for the research in this dissertation.

I would like to thank the staff and administrators of the Department of Geophysics for all their help during my years in graduate school. Tara Ilich and Lauren Nelson were especially helpful in guiding me through all my academic requirements. Susan Phillips-Moskowitz deserves special mention for the support, care, and humor she provided me and our research group over the years.

It was a great pleasure being part of a research group composed of so many fantastic friends and colleagues: Naomi Boness, Jeremy Brown, Laura Chiaramonte, Indrajit Das, Amy Day-Lewis, Paul Hagin, Rob Heller, Owen Hurd, Madhur Johri, Amie Lucier, Ellen Mallman, Pijush Paul, Hannah Ross, Hiroki Sone, and Alec Yang. I would like to especially thank Ashley Enderlin for her fantastic engineering work in support of our lab efforts. Other friends at Stanford and beyond were crucial in getting me through the many ups and down of graduate school.

I cannot thank my family enough for believing in me and encouraging me all the way to the end. My own success is a reflection of the love and support they have given me throughout my entire life.

Above all, I would like to thank my wife Jiffy for being everything I could ask for and more in a partner and best friend. This dissertation is as much hers as it is mine.

TABLE OF CONTENTS

LIST OF FIGURES

LIST OF TABLES

Chapter 1

INTRODUCTION

1.1 Overview

This thesis presents five studies of a gas shale reservoir using diverse methodologies to investigate geomechanical and transport properties that are important across the full reservoir lifecycle. Using the Barnett shale as a case study, I investigated adsorption, permeability, geomechanics, microseismicity, and stress evolution in two different study areas within the Barnett. The main goals of this thesis can be divided into two parts: first, to investigate how flow properties evolve with changes in stress and gas species, and second, to understand how the interactions between stress, fractures, and microseismicity control the creation of a permeable reservoir volume during hydraulic fracturing. Increased understanding of gas shale reservoirs will allow us to make better decisions regarding the development of these resources in both the United States and around the world.

Analyses of a first Barnett shale study area are presented in Chapter 2. For this work, I conducted laboratory experiments on core samples from a study well in the Barnett Shale. These laboratory experiments focused on measuring two important rock properties: adsorption and permeability. Adsorption is the attraction of gas molecules to the surface of a solid, forming a dense layer distinct from the free gas molecules. In the case of organic-rich gas shales, a significant portion of the methane found in these rocks is stored as an adsorbed phase. In some organic-rich rocks, such as coal, carbon dioxide is more strongly attracted to the solid surface of the rock than methane. This creates the potential for enhanced recovery of methane through the injection of carbon dioxide into the reservoir and the sequestration of the carbon dioxide as an adsorbed phase. This process could be an important tool in reducing carbon dioxide emissions into the atmosphere. I quantified the amount of adsorption for methane, nitrogen, and carbon dioxide in rock samples from the first study area, providing a starting point for the study of enhanced recovery and carbon dioxide sequestration in the Barnett shale.

I also investigated the gas permeability of intact core samples from the same study well used in the adsorption experiments. As gas is produced in these reservoirs, the pore pressure declines, increasing the effective stress in the reservoir and potentially impacting the permeability and thus the ability to produce gas economically. To quantify how stress changes impact the flow of gas in the Barnett shale, I measured permeability at a wide range of pore pressures and confining pressures and then determined an effective stress law for permeability in these samples. I also measured permeability as a function of gas species, providing additional characterization of the feasibility of enhanced CH_4 recovery and CO_2 in these rocks.

In the second Barnett shale study area, I investigated a complex, multi-well, multi-stage hydraulic fracturing experiment that was comprehensively logged and then monitored for seismicity during the stimulation. Chapters 3, 4, and 5 present analyses from this second study area. After characterizing the geological and geophysical properties of this reservoir, I built a geomechanical model of the stress state in the reservoir before the hydraulic fracturing. Geomechanical modeling is important in understanding how fractures will either be created or enhanced by the hydraulic fracturing, and thus in understanding whether the hydraulic fracturing process will lead to successful gas production rates. The geomechanical model is used as a basis for modeling the evolution of stress both during and after hydraulic fracturing in the final analysis.

Using the microseismic data collected during hydraulic fracturing, I developed a methodology to characterize the robustness of a hydraulic fracturing project based on the magnitude distribution of microearthquakes generated during the stimulation. This methodology modifies the magnitude scaling analysis pioneered by Gutenberg and Richter (1944) to a form appropriate for the stimulation-induced microearthquakes, which are of much lower magnitudes and also follow different scaling relationships than the larger crustal earthquakes usually studied in traditional analyses. I used this stimulation activity level metric to compare different hydraulic fracturing methodologies, which varied across the five wells in the study area.

Lastly, I modeled the evolution of stress in the reservoir both during and after hydraulic fracturing in order to better understand the controls on hydraulic fracturing

success and permeable volume creation. This study is unique in that there is direct information on the actual magnitudes of stress change in the reservoir from pressure changes measured at the end of each fracturing stage. Using analytical and numerical models that combine the effects of crack opening and poroelastic-induced stress, I attempted to model the measured changes in reservoir stress and explain the variations in fracture generation and permeable volume creation seen in the study area.

In the remainder of this chapter, I will review the background and motivation for the five studies just discussed, and then provide a brief summary of the work and findings that will be presented in Chapters 2-5.

1.2 Project Motivations

Natural gas is the second largest source of primary energy in the United States, supplying 24.7% percent of primary energy in 2009 (EIA, 2010b). Composed principally of methane (CH_4), natural gas produces far fewer potentially hazardous pollutants than coal when combusted. It also produces 43% fewer carbon dioxide (CO_2) emissions per unit of produced energy than coal (EIA, 1998). Used for electricity generation, a combined cycle gas turbine power plant can achieve typical efficiencies greater than 50% (NETL, 2010). These environmental factors, combined with changes in natural gas markets, have led to the percentage of electricity supplied by natural gas nearly doubling over the last 20 years in the United States, increasing from 11.9% of electricity in 1989 to 23.2% in 2009 (EIA, 2010b). Similar trends can be observed globally, where annual natural gas consumption is expected to increase from 108 trillion cubic feet (TCF) in 2007 to 156 TCF in 2035 (EIA, 2010c).

Despite growing demand, production of natural gas from conventional sources in the United States has been declining for over 15 years (EIA, 2010a). Unconventional natural gas reservoirs have been making up the difference, and are expected to continue to do so in the future. Unconventional reservoirs are differentiated from conventional reservoirs by their low permeability (as in tight gas sands), an adsorbed gas phase (as in coalbed methane), or by both of these factors (as in gas shales). Technology development, particularly the hydraulic fracturing of densely spaced directionally drilled wells, enabled economic production from these unconventional reservoirs. This

dissertation focuses on gas shales, the unconventional reservoir with the greatest growth in production over the last decade.

1.2.1 Gas Shale Reservoirs

Though they exhibit considerable variability in composition and geologic history, the major gas shale reservoirs in the United States are all characterized by extremely small grain sizes, low natural permeability, and elevated total organic carbon. After the organic-rich rock was buried and heated, first to temperatures high enough to generate oil and then to temperatures high enough to generate natural gas, the methane created during gas generation remained within the rock, trapped in free space and adsorbed to organic kerogen and clay minerals.

The major gas shale reservoirs in the United States can be seen in Figure 1.1. With so many recent discoveries of gas shale resources, these reservoirs are projected to supply 6.0 TCF of natural gas in 2035, up from 2.4 TCF in 2009 (EIA, 2010a). This would equal 26% of total U.S. annual natural gas production by 2035, up from 11.5% in 2009. The total gas shale resource base in the U.S. was estimated in 2008 to be 2,074 TCF (Potential Gas Committee, 2008). Out of this resource base, 60.6 TCF was believed to be proven reserves at the end of 2009, which was 21.3% of the total 283.9 TCF of economically recoverable reserves in all U.S. natural gas reservoirs (EIA, 2010e). Gas shale reservoirs, therefore, will potentially supply almost 6% of all energy consumed in the United States in 2035, nearly as much as is predicted for nuclear power (EIA, 2010a).

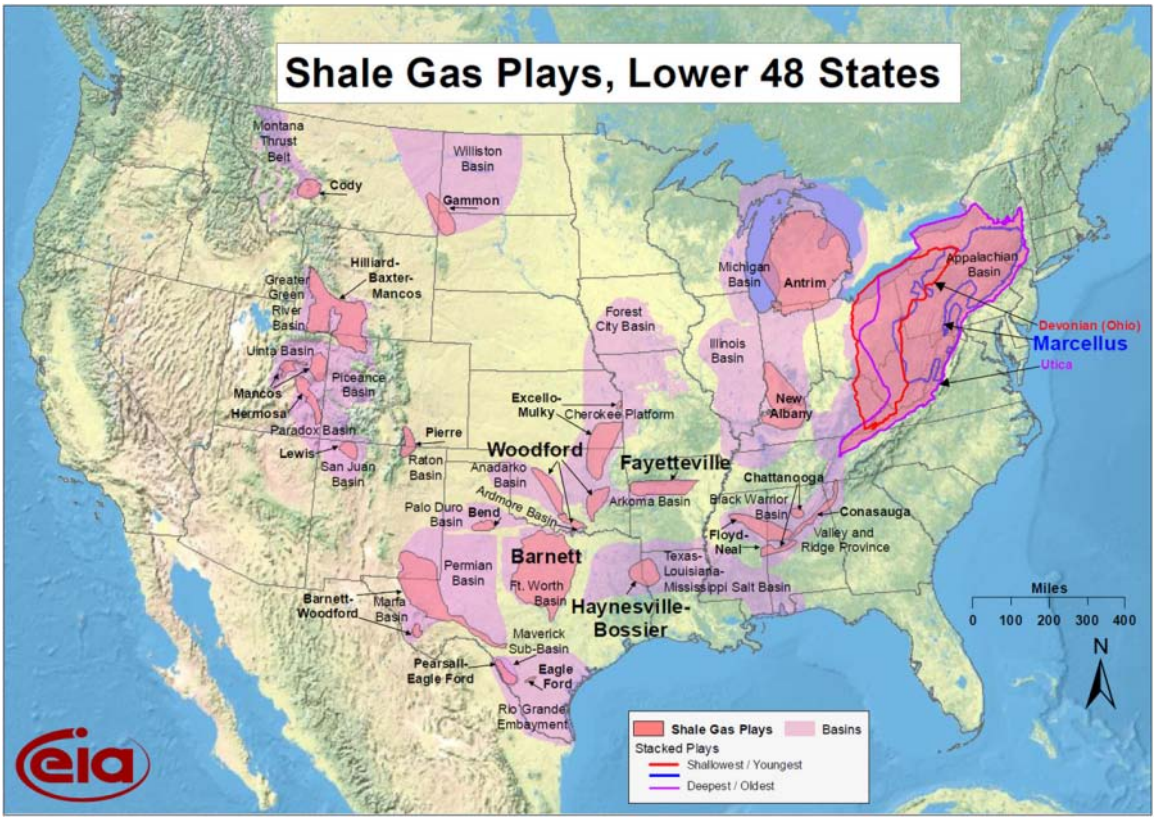

Figure 1.1: Map of major shale gas reservoirs in the United States, including the Barnett shale in the Ft. Worth Basin. Source: EIA (EIA, 2010d).

1.2.2 The Barnett Shale, Texas, USA

The Barnett shale has seen the most development of any gas shale reservoir in the world. The potential of the Barnett shale as a productive natural gas reservoir was discovered 1981 by Mitchell Energy (Martineau, 2007). Over the next 15 years, fewer than 400 wells were drilled in the Barnett, with limited success overall. However, in 1997, Mitchell Energy began to fracture wells using a slick-water fracturing fluid, rather than the viscous gel-based fracturing fluids used previously. Fracturing with water had two primary benefits. First, it was simply less expensive to use water as the primary fluid than to use a gel-based fluid. Second, water fracturing created a more widely distributed fracture network, thus allowing more of the reservoir to be accessed and drained. The success of slick-water fracturing (and the subsequent development of multi-stage fracturing in horizontal wells) led to a rapid growth in development over the last decade. The drilling and production history of the Barnett Shale can be seen Figure 1.2. In 2009,

the Barnett supplied 8.4% of domestic gas production (EIA, 2010b; Texas Railroad Commission, 2010).

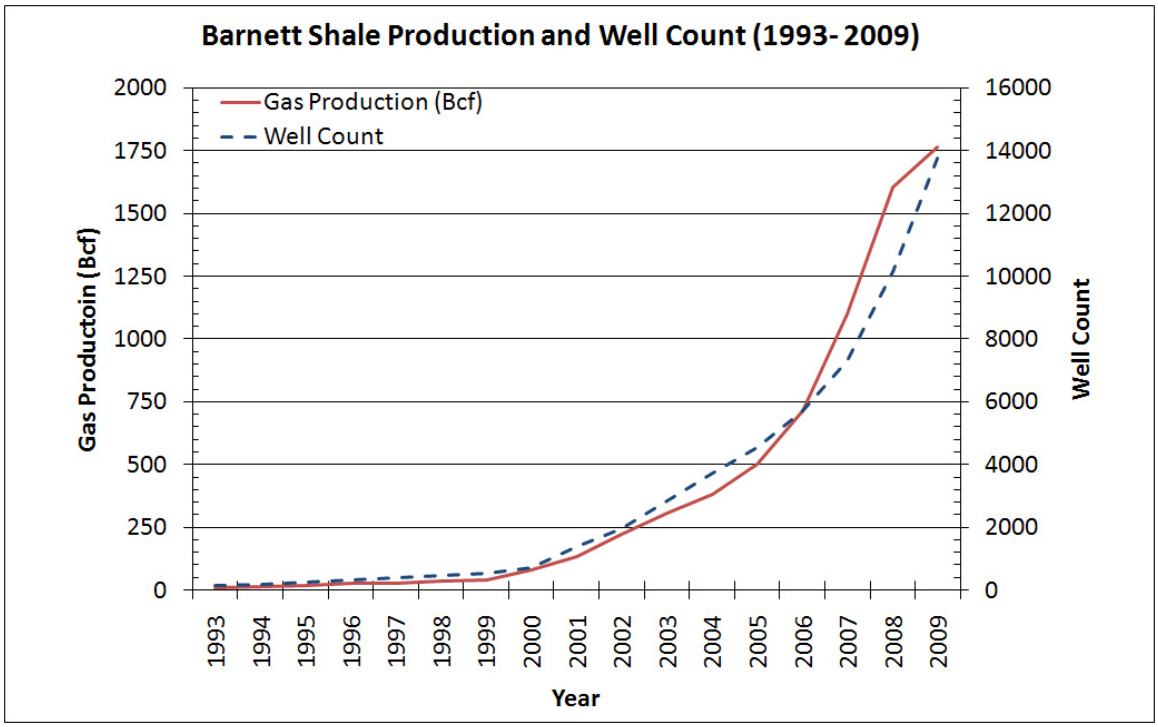

Figure 1.2: Barnett production history and well count, indicating rapid growth over the last 10 years. Source: Texas Railroad Commission (Texas Railroad Commission, 2010).

The Barnett shale is located in the Fort Worth Basin of northern Texas (Figure 1.1). The reservoir rock itself is a Mississippian age organic-rich shale. Composition can vary across the field and within the reservoir section, but the Barnett is noted for having generally high silica content (35-50%), relatively low clay content (<35%), and significant organic carbon content (3-10%) (Montgomery et al., 2005). Within the productive region of the field, the depth of the formation ranges from less than 4000 feet in the west to more than 8500 feet in the east, with net thickness increasing from 200 to 500 feet moving from the west to the east in the basin (Zhao et al., 2007).

The Barnett is typical of gas shale reservoirs in that production peaks early, and then declines rapidly (Figure 1.3). An important question for producers of the Barnett (and of other gas shale reservoirs) is how quickly this decline occurs and what controls the rate of decline. As gas is initially produced, the pore pressure in and around the fracture network is drawn down. This pressure decline results in an increase in the "effective stress" felt by the reservoir, potentially causing a reduction in permeability on

multiple scales. Thus, understanding the evolution of permeability in the reservoir with pore pressure and effective stress changes may be crucial to long term production and the ultimate success of the reservoir. Chapter 2 addresses the issue of pore pressure induced permeability change through extensive lab testing on intact Barnett Shale samples.

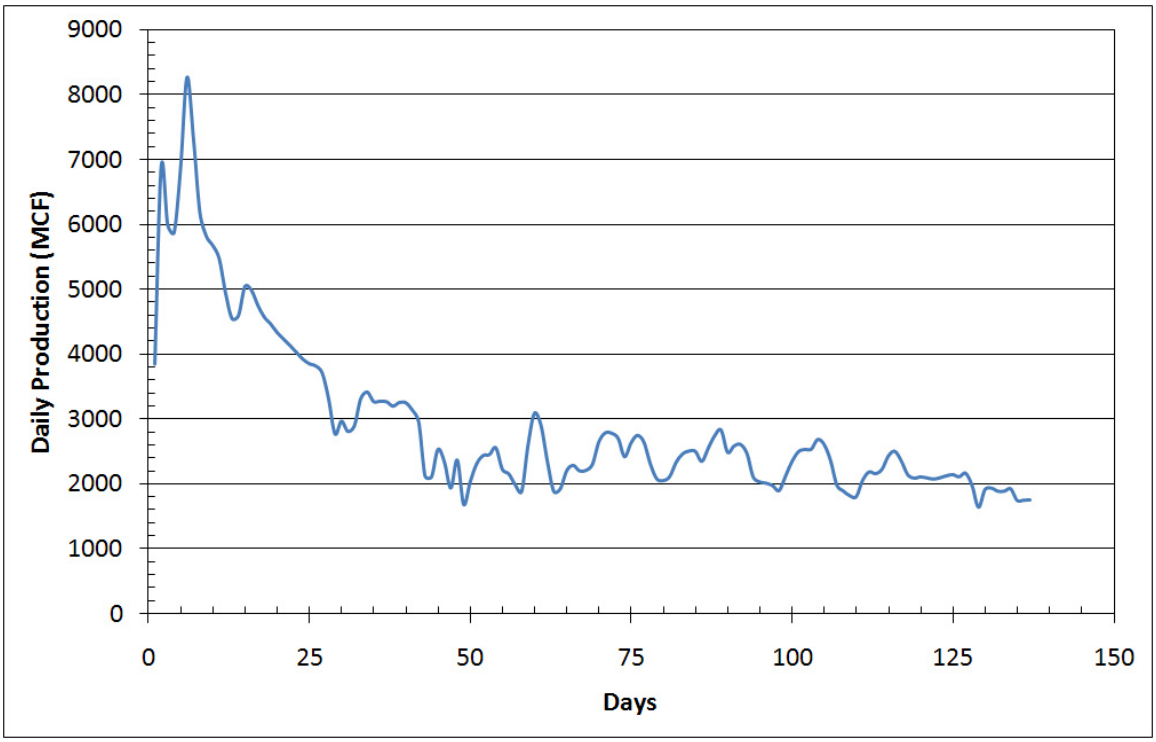

Figure 1.3: Combined daily production rate from the first four months of production of the Barnett shale study area wells A-E. Rapid decline in production after initial peak demonstrates the importance of reservoir transport properties to production success.

1.2.3 Hydraulic Fracturing and Production of Gas Shale Reservoirs

As discussed in section 1.2.2, water-based hydraulic fracturing led to successful production in the Barnett shale. By pumping large amounts of sand and water down the well, a network of fractures is created to access the trapped gas. Two things occur during the hydraulic fracturing process. First, a large planar hydraulic fracture is created in a direction perpendicular to the minimum horizontal stress. In addition to this planar tensile opening, significant numbers of shear failures (microearthquakes) are generated in the surrounding intact reservoir rock. As water leaks off from the main hydraulic fracture plane into the surrounding rock, the increased pore pressure leads to shear slip on pre-existing planes of weakness that are well-oriented for slip in the existing stress state (Cipolla et al., 2008; Palisch et al., 2008).

Despite this basic framework, the processes by which hydraulic fracturing leads to an interconnected, permeable fracture network are still poorly understood. The development of successful hydraulic fracturing methods is too often a trial and error process and our ability to even quantify the success of hydraulic fracturing is still in doubt. In addition, the relationship between stress change, fracturing, and permeable volume creation has been underexplored. To save time and energy as the next 10,000 gas shale wells are drilled, we need better knowledge of the fundamental interactions that occur in the reservoir as water and sand are injected and gas is produced. Chapters 3, 4, and 5 address these fundamental issues through a series of analyses on a case study project in the Barnett shale.

One major challenge in developing gas shale fields is to estimate the success of stimulation soon after, or even during, hydraulic fracturing. Adapting techniques commonly used in earthquake seismology, we developed a methodology to quantify the level of subsurface stimulation using the magnitude distribution of microearthquakes generated during the stimulation itself. This methodology and its application to microseismic data from the case study area are presented in Chapter 4.

Chapters 3 and 5 focus on geomechanical modeling of our Barnett shale study area. In Chapter 3, we analyze the stress state that existed in the field area before drilling or stimulation occurred. Despite stress being a key determinant to the success of gas shale stimulation, there have been few published case studies that provide a comprehensive analysis of the Barnett shale in situ stress. In Chapter 5, we measure the changes in reservoir stress that occurred during hydraulic fracturing and model these changes using analytical and numerical techniques. By both measuring and modeling the state of stress before, during, and after hydraulic fracturing, our analysis provides unique insight into the changes that occur in the reservoir as it is prepared for production.

1.2.4 CO_2 Sequestration and Enhanced Recovery Potential of Gas Shale Reservoirs

As stated previously, natural gas is a much cleaner fuel source than coal, with significantly lower CO_2 and pollutant emissions for an equal amount of energy. As the cleanest fossil fuel, natural gas has the potential to be a useful transition fuel while renewable energy technologies mature. However, coal reserves remain abundant in the

United States, China, and several other industrialized countries, leading to significant interest in finding cleaner ways to generate electricity from coal. To utilize the existing coal resources while limiting emissions, one option is to capture and sequester the emissions from a coal power plant, never allowing them to enter the atmosphere.

The three primary underground targets for carbon sequestration are saline aquifers, depleted petroleum reservoirs, and coalbed methane reservoirs (Figure 1.4), with the largest capacity for sequestration believed to be in saline aquifers. However, there are large cost constraints to producing energy through carbon capture and sequestration (CCS). For example, McKinsey (2008, 2009) has calculated that the average cost of sequestering CO_2 from a coal electric power plant with CCS will be $40-60 per ton of CO_2 in 2030, which is much more expensive as a CO_2 abatement measure than the deployment of other technologies, such as energy efficiency upgrades (Figure 1.5). In order to recoup some of the cost of capturing and sequestering the CO_2, the most economically promising projects may be those that generate an additional income stream through enhanced recovery of oil and natural gas.

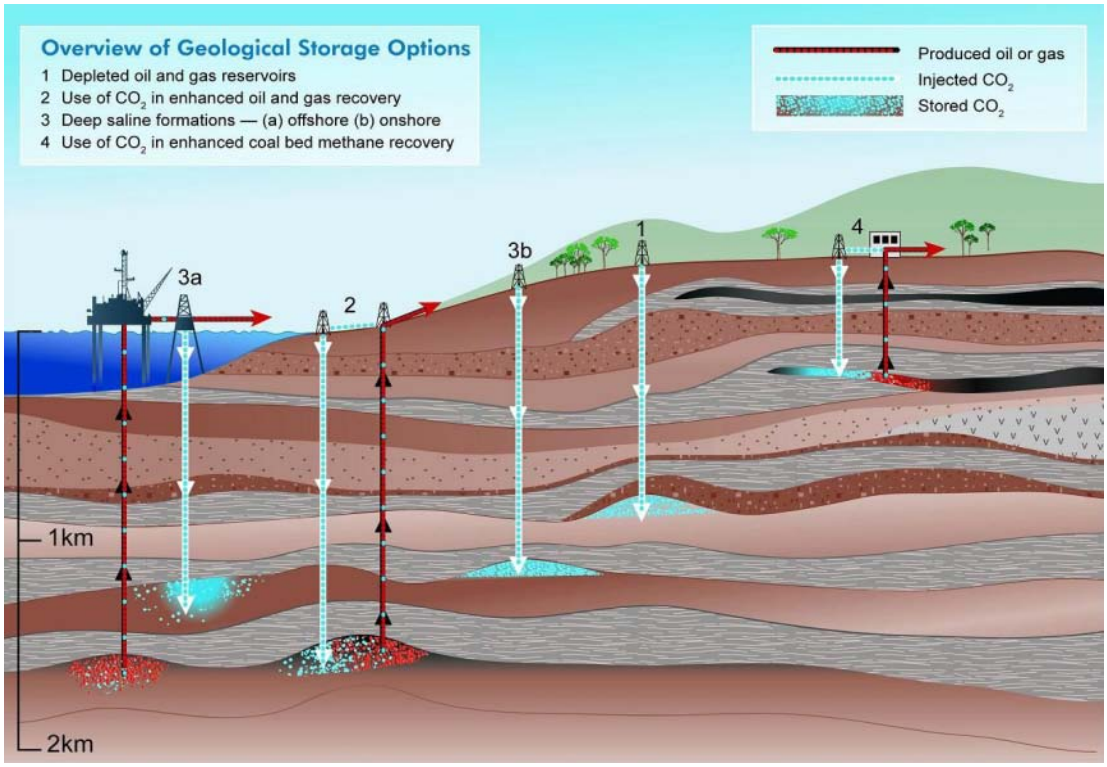

Figure 1.4: Conceptual overview of primary geologic carbon storage options, including enhanced coalbed methane recovery through CO_2 injection, a potential analogue for enhanced recover of methane in gas shales. Source: IPCC (2005).

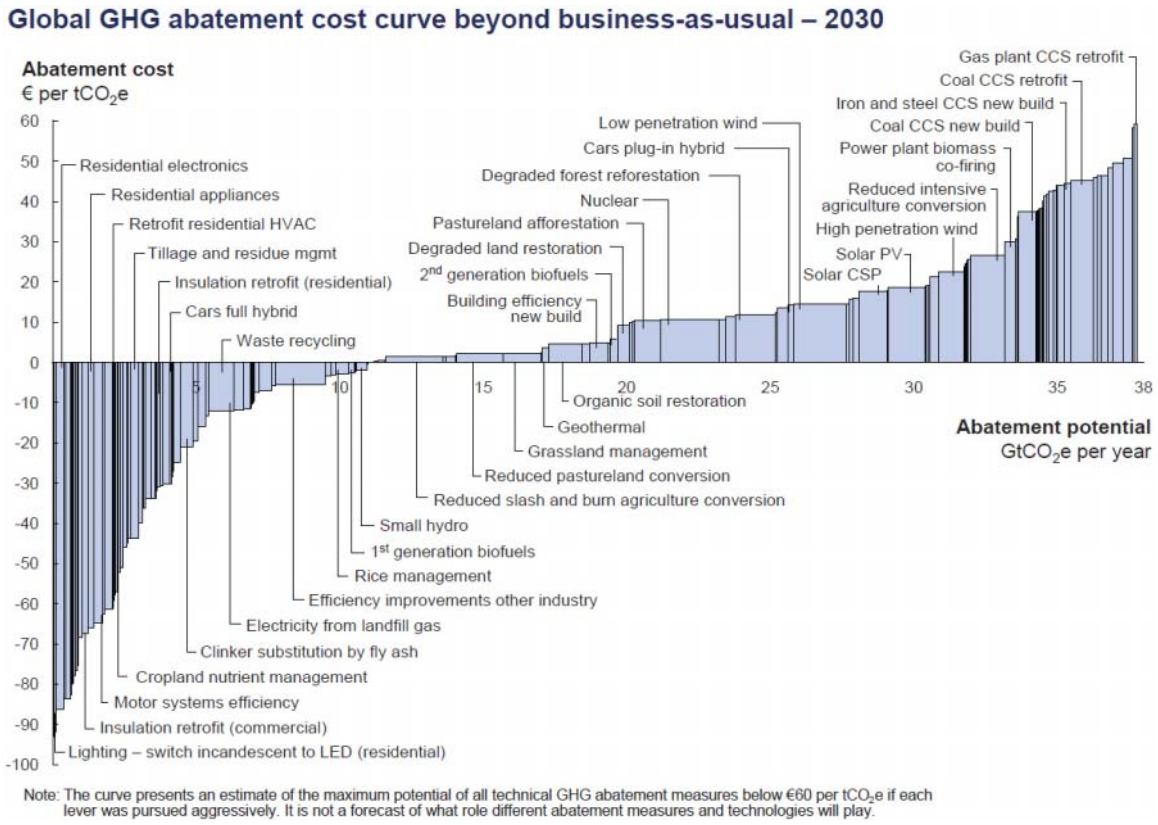

Figure 1.5: Global greenhouse gas abatement cost curve for 2030. The horizontal axis shows the abatement potential for a given technology (in units of $GtCO_2$ equivalent per year), while the vertical axis shows the cost in Euros per tCO_2e. While having a large abatement potential, "conventional" CCS is significantly more expensive than other abatement options. Source: McKinsey (2009).

Enhanced recovery of oil using CO_2 injection has been successfully deployed as a tertiary recovery process for several decades. In this process, injected CO_2 dissolves into the oil, reducing the viscosity of the oil and enhancing production. Much of the CO_2 is produced along with the oil, separated, and then re-injected into the reservoir. However, not all the CO_2 is recovered, leading to some net sequestration over time.

Enhanced recovery of natural gas appears to be promising only in unconventional reservoirs, such as coalbed methane. The idea of enhanced coalbed methane (ECBM) recovery is to inject CO_2 into the reservoir, releasing CH_4 from the coal surfaces due to the preferential adsorption of CO_2. This process has been extensively studied in recent years, with ongoing field tests to investigate the feasibility in real-world conditions.

Both gas shales and coalbed methane reservoirs are known to store methane as an adsorbed phase on the surface of organic carbon. Thus, gas shales may also have the potential for sequestration of CO_2 and enhanced recovery of CH_4. Moreover, with the

high well density in gas shale fields, additional wells may not need to be drilled to implement enhanced recovery, reducing the cost of sequestration. There are many challenges to proving the viability of sequestration and enhanced recovery in gas shales, the first of which is to determine the suitability of a rock for the actual process of preferential adsorption of CO_2 over CH_4. Previous studies have found promising results for Appalachian Devonian shales (Nuttall et al., 2005). In Chapter 2, I investigate the preferential adsorption of CO_2 and CH_4 on Barnett shale rock samples.

1.2.5 Environmental Impacts of Hydraulic Fracturing and Gas Shale Production

I want to make a special note about concerns over the environmental impact of hydraulic fracturing, an issue that has been moving to the forefront in discussions of gas shale development over the last year and that I expect will continue to be prominent. Reports of water contamination, gas leakage, and unexpected land use impacts appear to be caused primarily by operator error in cementing wells, handling produced water, and cleaning up drilling sites (Zoback et al., 2010). Due to the general depth of the gas reservoirs and the limited vertical extent of the fractures created during hydraulic fracturing, it is unlikely that the contaminations have occurred through direct migration out of the reservoir, through overlying formations, and into the near surface. In a sense then, hydraulic fracturing itself is “safe” – as long as all other drilling and operating procedures are correctly followed. However, with thousands of wells expected to be drilled in the coming years, many in pristine areas, there will undoubtedly be serious failures and accidents, even by the most diligent operators. To enable the public to make the best decisions about development of their lands, there is a need for increased transparency about the land use impacts, the processes used in drilling and fracturing, and the parties that are accountable for drilling and production operations. While this thesis does not directly touch on these issues, it is my hope that the research by my colleagues and myself will lead to better fundamental understanding of how to safely and successfully fracture and produce from a shale gas reservoir, thus allowing for more responsible use of this technology in the future.

Chapter 2

ADSORPTION, PERMEABILITY, AND EFFECTIVE STRESS IN THE BARNETT SHALE, TEXAS, USA

Abstract

We measured adsorption and permeability on Barnett shale samples. Our adsorption measurements focused on N_2, CH_4, and CO_2 with implications for potential storage of CO_2 and enhanced recovery of CH_4. Our permeability measurements were conducted with helium and focused on the stress-dependence of permeability in order to build an effective stress law for permeability.

We successfully measured adsorption on four Barnett shale samples. CH_4 and N_2 demonstrated Langmuir-type adsorption at magnitudes consistent with previous studies of the Barnett shale. Three of our samples demonstrated BET-type adsorption of CO_2 and one demonstrated Langmuir-type adsorption of CO_2, in contrast to all previous studies on CO_2 adsorption in gas shales that found Langmuir-adsorption. At low pressures (600 psi), we found preferential adsorption of CO_2 over CH_4 ranging from 3.6x to 5.5x. While our measurements were conducted at low pressures (up to 1500 psi), when our model fits are extrapolated to reservoir pressures they reach similar adsorption magnitudes as have been found in previous studies. At these high reservoir pressures, there is very large preferential adsorption of CO_2 over CH_4 (up to 5-10x) suggesting a significant potential for CO_2 storage in gas shales like the Barnett if practical problems of injectivity and matrix transport can be overcome.

We successfully measured permeability versus effective stress on two intact Barnett shale samples. Both samples demonstrated permeability effective stress coefficients less than 1, invalidating our hypothesis that there might be throughgoing flow paths within the soft, porous organic kerogen that would lead the permeability effective stress coefficient to be greater than 1. The results suggest that microcracks are likely the dominant flow paths at these scales, and further work is needed to understand

the size and distribution of these microcracks and how they are influencing permeability as the effective stress is changed.

2.1 Introduction

The Barnett shale is a complex rock, which makes accurate analysis of its geological, geophysical, petrophysical, and transport properties an ongoing challenge. The Barnett shows heterogeneity in composition and structure at all scales, from the basin-scale geology down to the nanometer-scale pore structure. Similarly, the production of natural gas from the Barnett and other gas shales is controlled by phenomena acting at many different scales, as has been recently reviewed by several authors (Bustin et al., 2008; Loucks et al., 2009; Wang and Reed, 2009; Sondergeld et al., 2010a; Sondergeld et al., 2010b).

One important property impacting production in the Barnett is the pressure-dependent adsorption of CH_4, which is controlled by the composition and microstructure of the rock. Gas is stored in the Barnett in both a free phase and a dense adsorbed phase, allowing for much greater total storage of gas than if there were a free phase alone. The amount of adsorption has a major impact on the total gas-in-place in the reservoir and therefore its potential as an economic producer. If preferential adsorption of CO_2 over CH_4 occurs in the Barnett, there may be the potential for enhanced recovery of CH_4 and sequestration of CO_2 in the reservoir, providing increased production of the cleanest fossil fuel and sequestration of the primary greenhouse gas. To investigate these questions, we conducted adsorption tests on a series of Barnett samples.

The permeability of a gas shale also has a major impact on its production potential. There is significant variation in permeability at all scales, from major faults at reservoir scale, to cracks at centimeter scale, to pores at nanometer-scale. At all these scales, the permeability is likely strongly controlled by the stresses and pore pressures in the reservoir. Since hydraulic fracturing and gas production can significantly alter these stresses and pore pressures, it is important to quantify the sensitivity of permeability to these large changes. Focusing on intact samples on the scale of a few centimeters, we conducted permeability tests over a broad range of confining and pore pressures. Using

the changes in permeability as a function of stress and pressure, we built permeability effective stress laws for Barnett shale samples.

2.1.1 Adsorption of Methane and CO_2 in Organic-Rich Rocks

Adsorption is the attraction of gas molecules to the surface of a solid, creating a high-density phase that is distinct from the surrounding free gas molecules. Microporous materials commonly exhibit high adsorption potential due to their significant internal surface area. Gas shales are composed of several percent microporous organic kerogen, and thus have been shown to adsorb reservoir gases like CH_4. Due to the high density of the adsorbed phase, adsorption is an important storage mechanism in gas shales.

To quantify the adsorption potential for a material, the amount of adsorption is measured at many different pressures, keeping temperature constant to generate an adsorption isotherm. The magnitude and shape of the adsorption isotherm gives insight into the mechanism of adsorption in the material. In general, the adsorption isotherm will be controlled by the distribution of pore sizes in the material, the effective molecular size of the adsorbing gas, and the combined attraction energy of the surface material and the adsorbing gas (Langmuir, 1916; Brunauer et al., 1938). For example, a material with a high internal surface area will have greater adsorption potential than a material with a lower internal surface area, all other properties being equal. For some materials, the equilibrium energy state for adsorption will allow for only a single monolayer of adsorbed gas molecules, while in other cases the equilibrium energy state will allow for multiple layers of adsorbed gas molecules. The number of layers of adsorbed gas molecules will be a function of both the material itself and the specific adsorbing gas.

Isotherms for rocks like coal or a gas shale are often fit by a Type I, or Langmuir, isotherm (Figure 2.1). The Langmuir isotherm represents the adsorption of a monolayer of molecules on the inner surfaces of the material (Langmuir, 1916). It can be fit with a two-parameter equation:

$$V(P) = \frac{V_L P}{P_L + P} \tag{2.1}$$

where $V(P)$ is the volume of adsorption at pressure P, V_L is the Langmuir volume, representative of total adsorption at infinite pressure, and P_L is the Langmuir pressure, which is the pressure at which half of the maximum amount has adsorbed. For materials that demonstrate a Langmuir isotherm for a specific gas, the equilibrium energy state for the gas-surface system would be a single (effective) layer of adsorbed gas molecules.

If multi-layer adsorption occurs, then a Type II, or BET, adsorption curve is used to fit the data (Figure 2.1). As with a Langmuir isotherm, a BET isotherm can also be fit with a two parameter equation (Brunauer et al., 1938):

$$V(P) = \frac{V_m C P}{(P_0 - P)\left[1 + (C-1)P/P_0\right]} \tag{2.2}$$

where P_0 is the vapor pressure of the gas, V_m is the maximum monolayer adsorption, and C is a parameter that controls the shape of the adsorption curve at low pressure.

However, the standard BET isotherm assumes that an infinite many number of adsorption layers are possible as pressure increases, despite the finite volume of free space in a rock and the finite capacity of a surface to adsorb gas layers. Thus, it is common to use an "N-layer" BET isotherm that assumes there are a maximum N layers that can be adsorbed onto the internal surfaces:

$$V(P) = \frac{V_m C P_R}{1 - P_R} \frac{1 - (N+1)P_R^N + N P_R^{N+1}}{1 + (C-1)P_R - C P_R^{N+1}} \tag{2.3}$$

where P_R is the ratio of the measured pressure (P) to the vapor pressure (P_0), and N is the maximum number of adsorption layers. For materials that demonstrate a BET or N-BET isotherm for a specific gas, the equilibrium energy state for the gas-surface system would be multiple (effective) layers of adsorbed gas molecules.

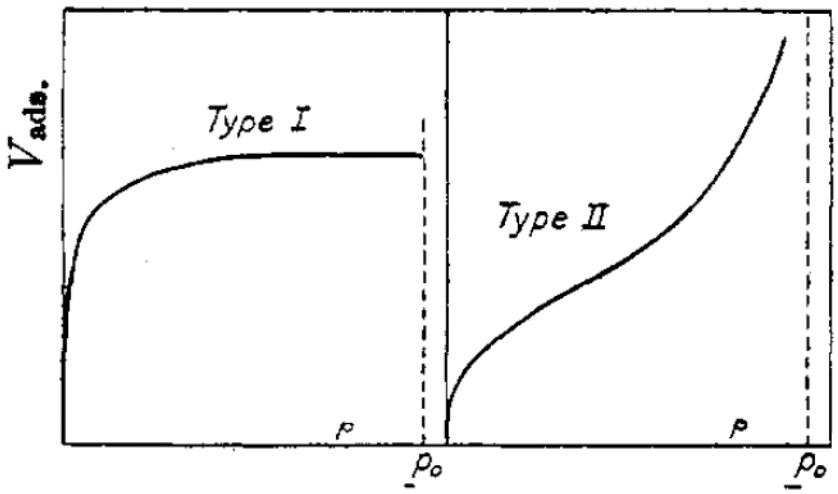

Figure 2.1: Type I (Langmuir) adsorption curve, representing monolayer adsorption, and Type II (BET) adsorption curve, representing multi-layer adsorption. Source: Brunauer et al. (1940)

The generation of CH_4 adsorption isotherms is important for gas-in-place calculations and reservoir modeling, and thus has been assessed previously for gas shales including the Barnett. Lu et al. (1995b; 1995a) found Langmuir-type adsorption of CH_4 for samples from Appalachian Devonian shales and from the Antrim shale. For Barnett shale samples, Montgomery et al. (2005) found Langmuir-type adsorption of CH_4.

While CH_4 adsorption has long been seen as important for gas production in unconventional reservoirs, CO_2 adsorption has only recently been studied in the context of enhanced recovery and sequestration. CO_2 adsorption in coal has been studied extensively, with researchers finding significant preferential adsorption of CO_2 over CH_4 and thus the potential for enhanced recovery and sequestration (Kovscek et al., 2005). To date there have been only two published papers on CO_2 adsorption in gas shales. Nuttall et al. (2005) found Langmuir-like adsorption of CO_2 that was five times greater than the amount of CH_4 adsorption. Kang et al. (2010) studied CO_2 adsorption on two Barnett shale samples, finding five to ten times greater adsorption of CO_2 than CH_4. However, Kang et al. (2010) only took five adsorption measurements per sample, all at high pressures above 2000 psi. They also assumed a priori that there would be Langmuir-like adsorption as part of their experimental method, while other authors have found non-Langmuir adsorption of CO_2 on coal and shale rocks (Busch et al., 2008; Lin, 2009). Thus, to further our understanding of adsorption in the Barnett shale, we conducted adsorption experiments using N_2, CH_4, and CO_2 on four Barnett shale samples.

2.1.2 Permeability and Effective Stress in Gas Shales

One of the primary characteristics of the Barnett shale and other gas shales is their very low intrinsic permeability. To produce gas from these reservoirs, it is necessary to hydraulically fracture the rock, creating additional fractures and surface area to access the gas in the rock matrix. As gas is produced, the permeability in both the fractures and the matrix is likely to decrease in the reservoir, leading to declining rates of production over time. This decrease in permeability is caused by an increase in the effective stress in the reservoir, which goes up as pore pressure goes down. The relationship between permeability and effective stress has been a focus of recent research in the Barnett, particularly on the sensitivity of fracture permeability to changes in stress. Kassis and Sondergeld (2010) found that the permeability of a propped fracture is more sensitive to stress changes than the permeability of a shear-offset fracture. The complementary stress sensitivity of the intact matrix permeability has been underexplored. While some studies have measured the sensitivity of gas shale matrix permeability at a single pore pressure (Bustin et al., 2008) or at a single confining pressure (Kang et al., 2010), no studies have measured permeability across a full range of effective stresses. In particular, a full permeability effective stress law has yet to be developed for any gas shale rocks, including the Barnett shale.

The techniques to formalize an effective stress law for low permeability rocks have been well established (Zoback and Byerlee, 1975; Bernabe, 1986; Bernabe, 1987; Warpinski and Teufel, 1992; Kwon et al., 2001; Li et al., 2009). It is first necessary to measure permeability over a wide range of pore pressures and confining pressures. The permeability data is then fit to a function $k\left(\sigma_{eff}\right)$, where k is permeability and σ_{eff} is the effective stress. The effective stress is defined as $\sigma_{eff} = C_p - \chi P_p$, where C_p is the confining pressure, P_p is the pore pressure, and χ is the effective stress coefficient for permeability. χ therefore determines the relative sensitivity of permeability to changes in confining pressure and pore pressure.

Most rocks have been shown to have $\chi \leq 1$, indicating that changes in reservoir stress have a greater impact than changes in pore pressure. However, some authors have

found $\chi > 1$ for clay-bearing sandstones (Zoback and Byerlee, 1975; Walls and Nur, 1979). The explanation for the behavior of these rocks is that the matrix through which fluid flows has a higher compressibility than the granular framework that supports the confining stress (Figure 2.2). If pore pressure and confining pressure go up by an equal amount, the compressible flow paths feel more of the pore pressure change than the confining pressure change, increasing the overall permeability for the rock.

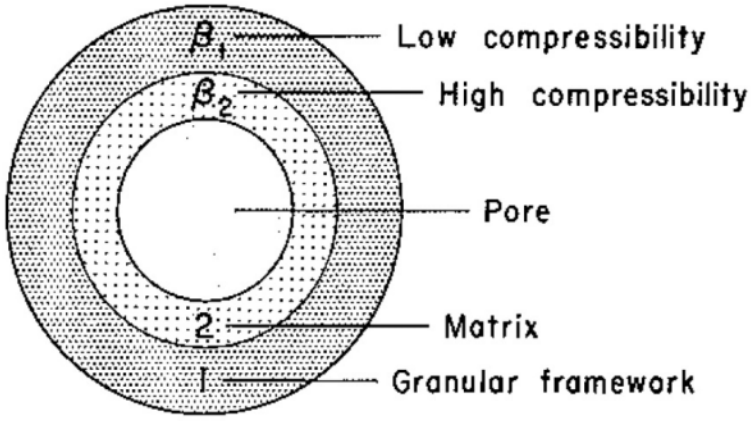

Figure 2.2.: Conceptual model of a compressible flow path within a stiff, stress-bearing framework. Source: Zoback and Byerlee (1975).

Recent imaging (Figure 2.3) has revealed that in the Barnett the majority of porosity is in the organic kerogen (Loucks et al., 2009; Wang and Reed, 2009; Sondergeld et al., 2010a). If the soft, compressible kerogen were a throughgoing fluid pathway, Barnett shale samples might exhibit $\chi > 1$, like has been seen in clay-bearing sandstones. However, if the kerogen were merely the supplier of gas to a network of microcracks and larger pore throats, a gas shale would behave like a typical rock with $\chi \leq 1$. Our research on effective stress laws for permeability in gas shales therefore addresses this fundamental question of dominant flow paths and also provides permeability-effective stress relationships as inputs to production analysis and reservoir simulation.

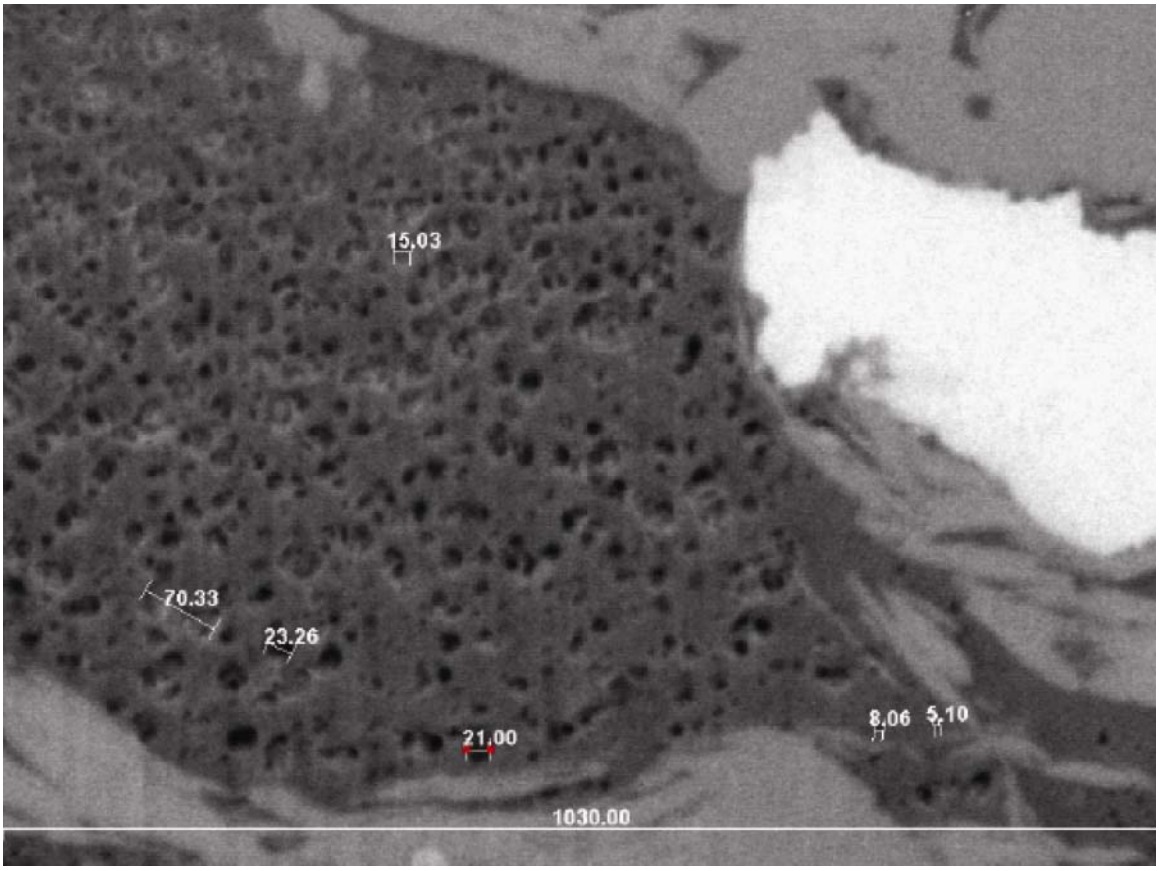

Figure 2.3: Backscattered SEM image of porous kerogen in the Barnett shale, demonstrating the concentration of porosity in the soft kerogen. Pore throat dimensions are in nanometers and the image itself is 1030 nanometers across. Source: Sondergeld et al. (2010a)

2.2 Data and Samples

The samples we used are from a Barnett shale well drilled in 2008 and then cored through the reservoir interval. We evaluated well logs and inspected the core in person to identify locations that were representative of the rock property diversity seen in the core. 1-inch diameter plugs were then drilled from these locations to be used for our permeability and adsorption experiments and also complementary mechanical experiments by Stanford colleagues. It is important to note that the Barnett samples we tested were stored in open air and at room temperature. Thus, the evaporation of volatiles and intrusion of atmospheric moisture and gases may have affected rock properties compared to the true in situ values. In addition, our permeability measurements were done on samples removed from deep within the subsurface (which is known to create stress relief microcracking) and plugged using a drill bit (another potential source of microcrack creation). Both of these factors may have influenced measured permeability

compared to in situ permeability. As discussed below, we attempted to address these issues by vacuum drying of all samples and rigorously pre-stressing all permeability samples.

In the following sections, we provide background on the geological properties of the samples and also discuss the results of a compositional analysis on the sample set.

2.2.1 Geology and Well Logs in Barnett Shale Study Well

While a more detailed geologic history of the Barnett shale is discussed in Chapter 3, we will give a brief overview here on the geologic context of the samples we used in our laboratory experiments. Interpreted well logs from the cored well are shown in Figure 2.4a. The well is from the region where the Barnett is divided by the Forestburg limestone into upper and lower zones and the Viola limestone separates the Barnett from the Ellenberger formation. The lower Barnett is approximately 900 ft thick in this region.

The samples we analyzed for adsorption and permeability are from the depth locations noted in Figure 2.4b. With an average depth of 8600 ft and a pore pressure gradient of approximately 0.5 psi/ft, the pore pressure in the reservoir section was approximately 4300 psi in situ. Sone and Zoback (2010b) determined stress magnitudes for this region, finding an S_v of 9500 psi, an S_{hmin} of 6800 psi, and an S_{Hmax} of 8,500 to 12,000 psi. The average stress in the reservoir was therefore about 9000 psi, giving a 4000 psi difference in average stress and pore pressure. To prevent new permanent deformation in our samples, we limited the maximum difference between confining pressure and pore pressure to 4000 psi in our experiments.

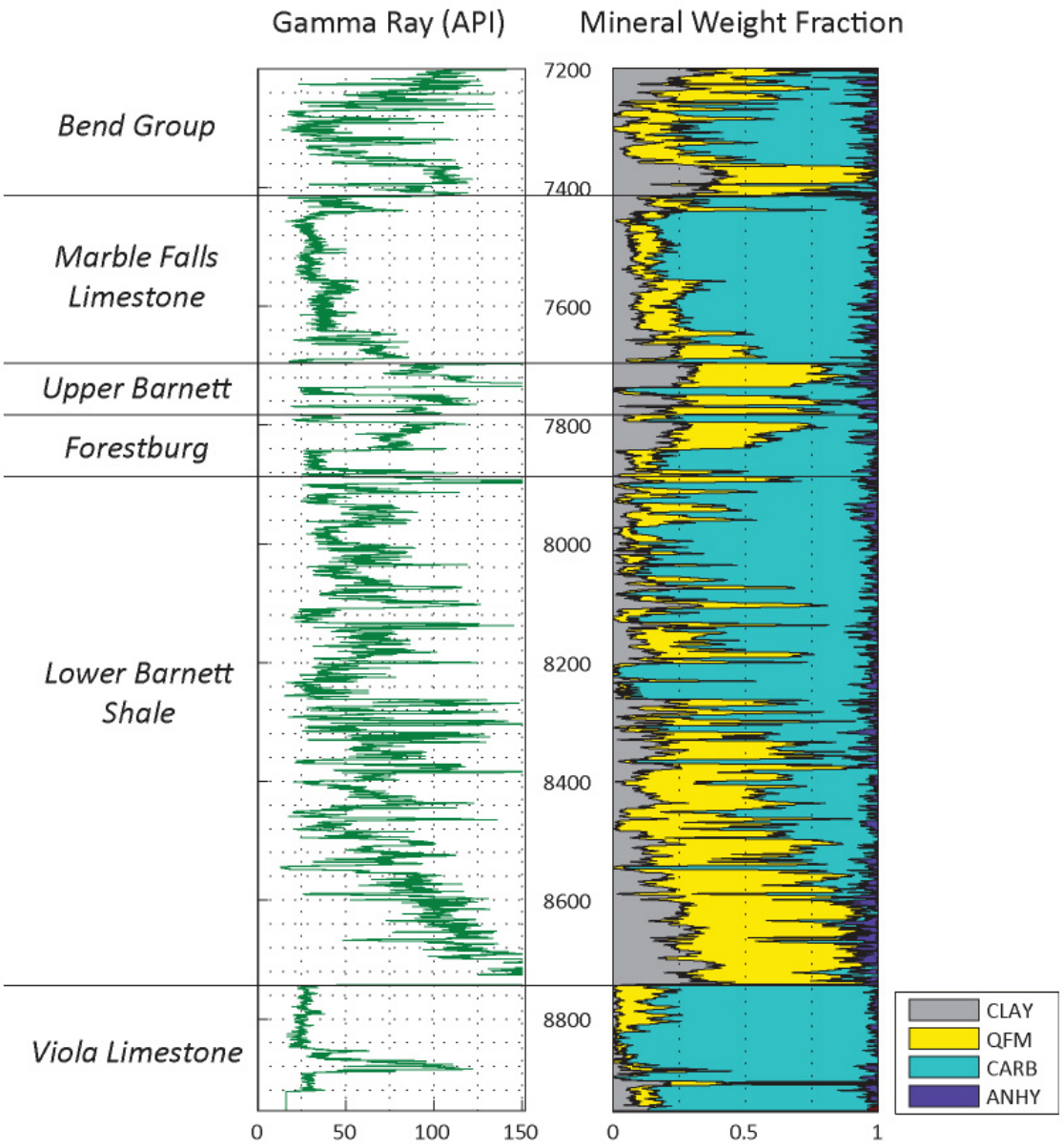

Figure 2.4a: Formation depths, gamma ray, and interpreted mineralogy from cored study well. Well is in region of basin where the Barnett is divided by the Forestburg limestone into upper and lower sections. Mineral fraction based on SpectroLith technique to interpret well log suite. Anhydrite detection may be an interpretation artifact as it was not found in the cored samples. (CLAY: clay minerals; QFM: quartz, feldspar, and mica; CARB: carbonates; ANHY: anhydrite)

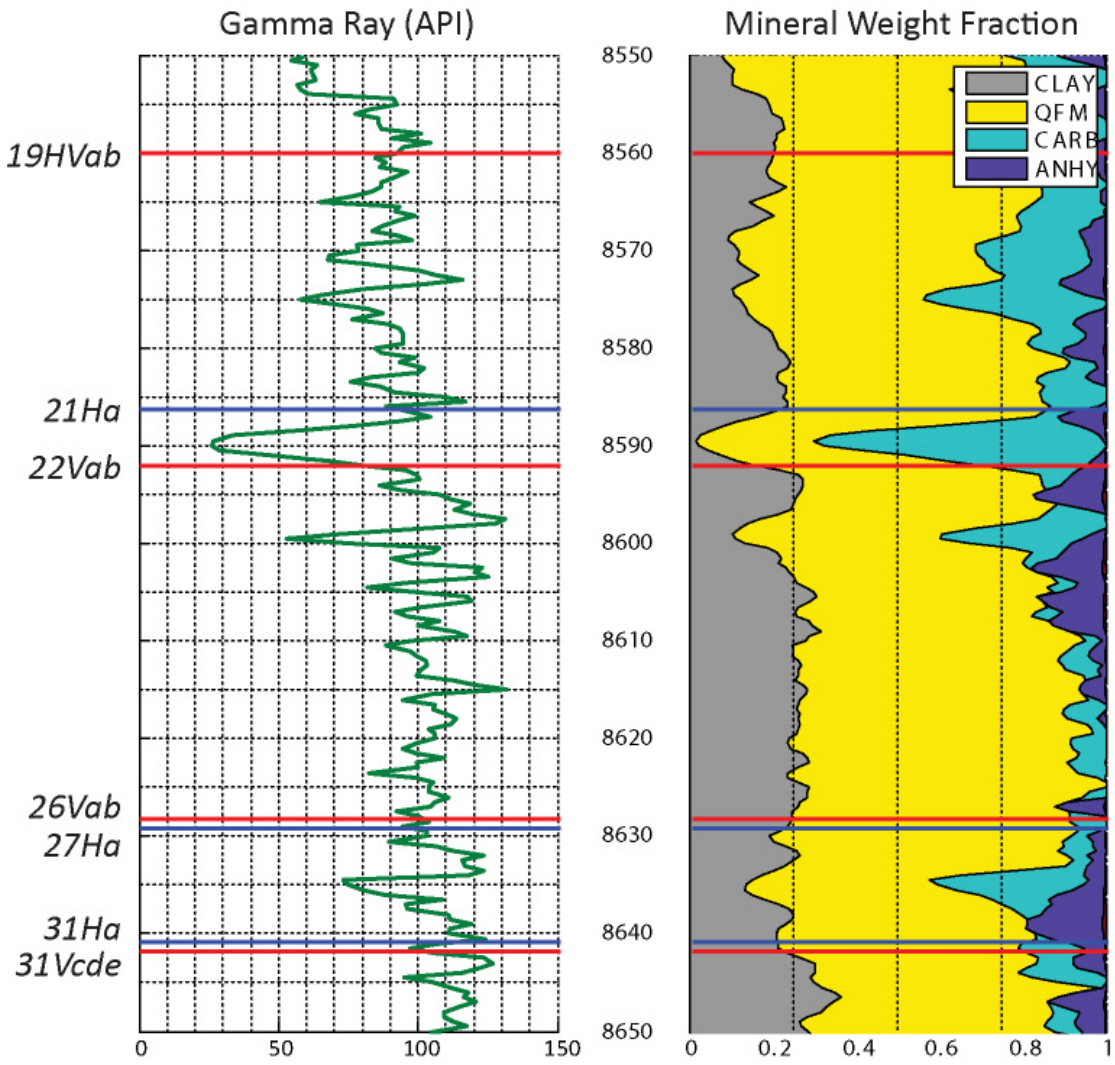

Figure 2.4b: Locations of lab samples plotted on gamma ray and mineralogy log. Red lines are adsorption samples; blue lines are permeability samples. XRD mineralogy gives significantly more accurate compositional analysis of core samples due to the coarse resolution of well log tools.

2.2.2 Composition and Mineralogy of Tested Samples

We analyzed each core plug visually for fractures or heterogeneities, and selected samples to represent different compositions found in the well. While ideally we would have tested the same samples for both permeability and adsorption, the need to run adsorption and permeability experiments in parallel on our separate systems prevented the combined testing of any of our samples for this study.

The samples were analyzed by ConocoPhillips for mineral composition using standard XRD methods (Warren, 1969). Pyrolysis and TOC were conducted by

Weatherford Laboratories using Rock-Eval methods (Peters, 1986; Peters and Cassa, 1994). The mineralogical properties of the samples used for laboratory students are presented below in Table 2.1 and Table 2.2 and graphically in Figure 2.5a and Figure 2.5b. All samples show high quartz concentration (43.5-56.7%) as is typical of the productive areas of the Barnett shale. TOC varies from 3.0% to 5.7% in the sample set, while total carbonate content varies from 0.4% to 14.3%. Clay minerals vary from a low of 23.8% to a high of 39.6%. There is minor pyrite in nearly every sample. All samples are in the oil window for maturity based on pyrogram peak temperatures. Kerogen type is between Type III (gas-prone) and Type II-III (oil-gas prone) for all samples except 21Ha, which is closer to Type IV (inert) based on its low hydrogen index and high oxygen index.

Table 2.1: Mineralogical properties of adsorption samples.

	19HVab	22Vab	26Vab	31Vcde
Depth (ft)	8560.0	8592.0	8628.2	8641.8
Depth (m)	2609.1	2618.9	2629.9	2634.0
Mass (g)	22.6	34.3	31.6	34.6
TOC (%)	3.4	3.6	4.0	5.7
Quartz (%)	49.2	48.8	43.5	48.2
Plagioclase Feldspar (%)	3.7	4.2	5.3	4.3
Calcite (%)	4.2	10.7	11.3	0.3
Dolomite (%)	10.1	1.1	2.3	0.2
Ankerite (%)	0.0	0.8	0.0	0.1
Illite (%)	21.9	19.0	19.3	25.2
Illite/Smectite (%)	6.1	9.3	8.4	13.6
Pyrite (%)	1.3	1.6	2.0	1.8
Apatite (%)	0.0	0.9	4.1	0.5
S1 (mg HC/g rock)	3.3	5.1	6.2	4.2
S2 (mg HC/g rock)	4.1	4.1	4.3	6.9
S3 (mg HC/g rock)	0.3	0.4	0.5	0.6
Tmax (°C)	452.0	450.5	447.0	452.3
HI (mg HC/g TOC)	119.5	112.3	109.0	119.8
OI (mg CO2/g TOC)	10.5	11.2	12.0	9.8

Table 2.2: Mineralogical properties of permeability samples.

	27Ha	31Ha	21Ha
Depth (ft)	8629.2	8640.8	8586.3
Depth (m)	2630.2	2633.7	2617.1
Length (in)	0.95	0.64	1.63
Length (cm)	2.40	1.61	4.14
Mass (g)	29.8	19.4	51.9
Sample Density (g/cc)	2.45	2.37	2.47
Mineral Density (g/cc)	2.68	2.66	2.72
Density Porosity (%)	0.086	0.107	0.090
TOC (%)	3.8	5.3	3.0
Quartz (%)	56.7	51.3	42.7
Plagioclase Feldspar (%)	3.8	4.0	4.8
Calcite (%)	7.7	0.0	2.9
Dolomite (%)	1.4	0.4	2.8
Ankerite (%)	0.0	0.0	2.3
Illite (%)	15.7	23.6	26.7
Illite/Smectite (%)	8.1	13.8	12.9
Pyrite (%)	1.8	1.7	2.0
Apatite (%)	1.0	0.0	0.0
S1 (mg HC/g rock)	4.8	4.4	3.0
S2 (mg HC/g rock)	4.5	6.1	3.2
S3 (mg HC/g rock)	0.3	0.3	0.8
Tmax (°C)	448	452	450
HI (mg HC/g TOC)	119	115	106
OI (mg CO2/g TOC)	8	6	25

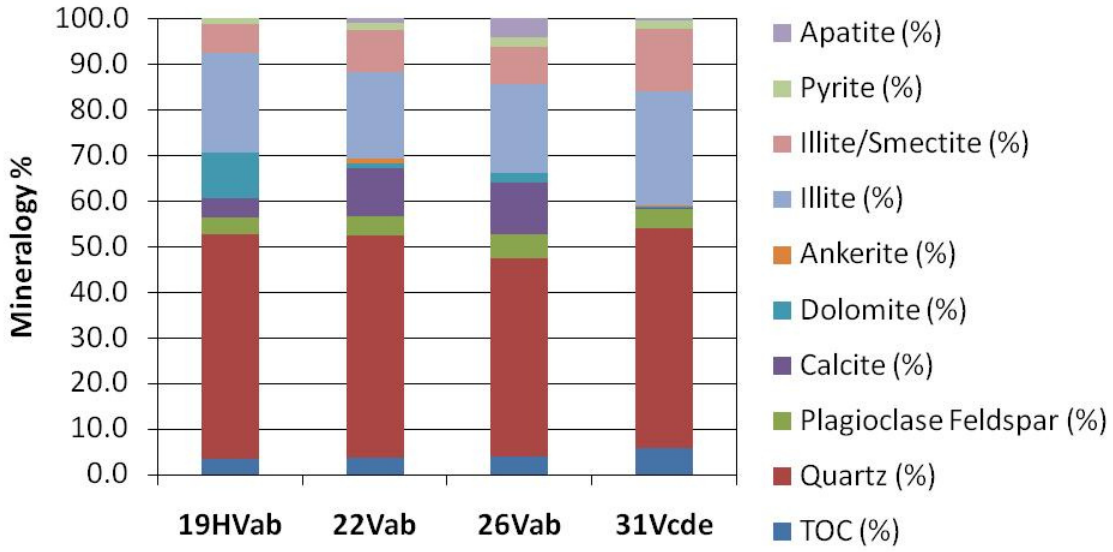

Figure 2.5a: Bar charts of mineralogical properties of the four Barnett shale samples used for adsorption experiments.

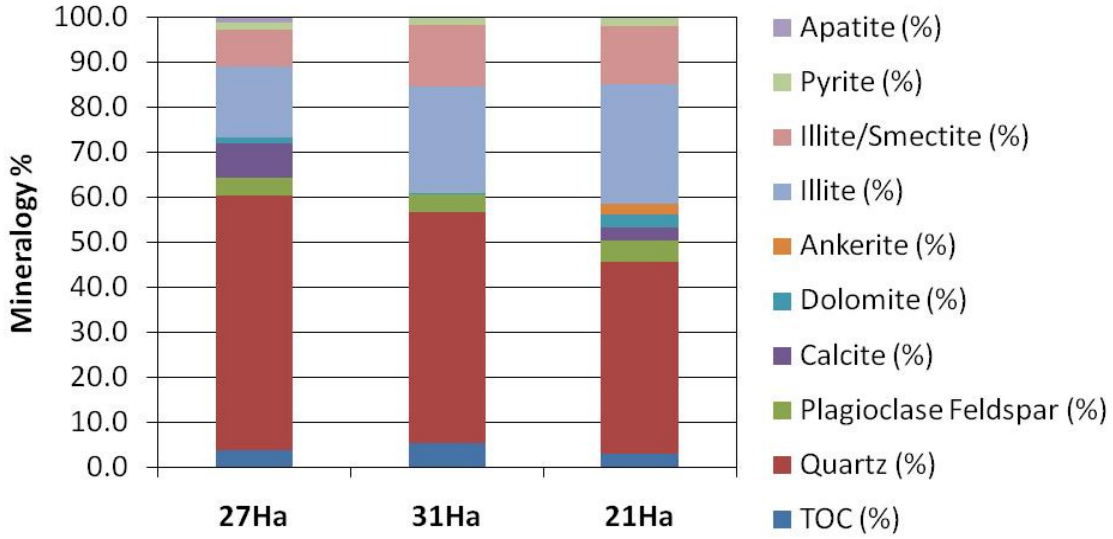

Figure 2.5b: Bar charts of mineralogical properties of the three Barnett shale samples used for permeability experiments.

2.3 Methodology

We conducted a series of adsorption and permeability tests on Barnett shale samples to answer the questions discussed above in section 2.1. All tests were done in our own lab using equipment built and/or modified ourselves. In the following sections, we describe our laboratory setup and detail the techniques we used to measure both adsorption and permeability.

2.3.1 Laboratory Equipment

2.3.1.1 Modified Tri-Axial System

We specially modified an NER Autolab 2000 tri-axial press to measure adsorption at a range of confining and pore pressures. While this machine is typically used for rock mechanics experiments, we found the confining pressure control and precise tracking of deformation to be beneficial in investigating the mechanical effects of adsorption on the sample. We use a Quizix QX-1500 to control and precisely record gas pressures. Valves are used to deliver gas from an upstream reference volume to the downstream sample volume. A schematic of the adsorption system is shown in Figure 2.6. We calibrated the upstream reference volume using multiple gas expansions from the known volume of the Quizix pump. Following the procedure in section 2.3.2, we calculated the upstream reference volume to be 29.98 ± 0.08 ml. We measured gas leakage rates at a range of pressures and corrected our adsorption calculations for this loss. We also record gas temperatures for use in equation of state calculations.

2.3.1.2 Hydrostatic Permeability System

We built a hydrostatic system to measure permeability on our Barnett shale samples. The layout of this system is shown in Figures 2.7 and 2.8. The pressure vessel is a Temco HCH bi-axial, hydrostatic core holder, with a floating plug on one end to provide even confining pressure and also to accommodate samples of differing length. The confining pressure is controlled by a manual high pressure generator using silicone oil as the confining fluid. The pore pressure is controlled by a Quizix QX-6000, with two pistons capable of applying constant pressures, constant flow rates, or pulses of gas pressure. In addition to the pressure transducers in the Quizix, we put high-precision Heise DXD pressure transducers close to the upstream and downstream ends of the pressure vessel in order to precisely measure the differences in pore pressure across the sample during testing. A Heise DXD transducer also measures the confining pressure. Temperature in the upstream and downstream sides is measured with thermocouples. All data is recorded in LabView on a dedicated PC. Using multiple gas expansions from the Quizix pump, we calculated the downstream reservoir volume to be 14.80 ± 0.07 ml.

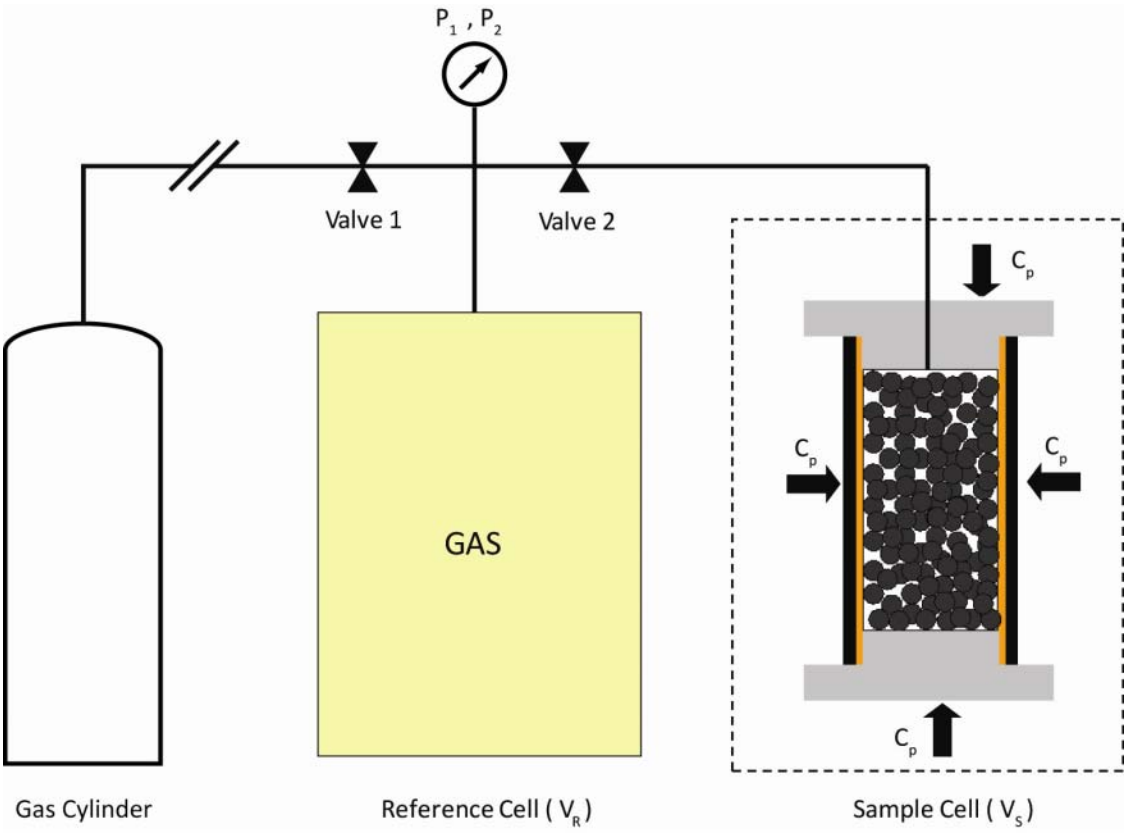

Figure 2.6: Schematic of system used for adsorption experiments. For the reference cell (V_R), a cylinder of the Quizix pump is used. The sample cell (V_S) is shown on the right, encased by a copper and viton jacket to isolate the sample and pore fluid from the confining fluid. Pressure is measured by a digital transducer within the Quizix pump. Gas temperature is measured close to where the gas lines enter the tri-axial press.

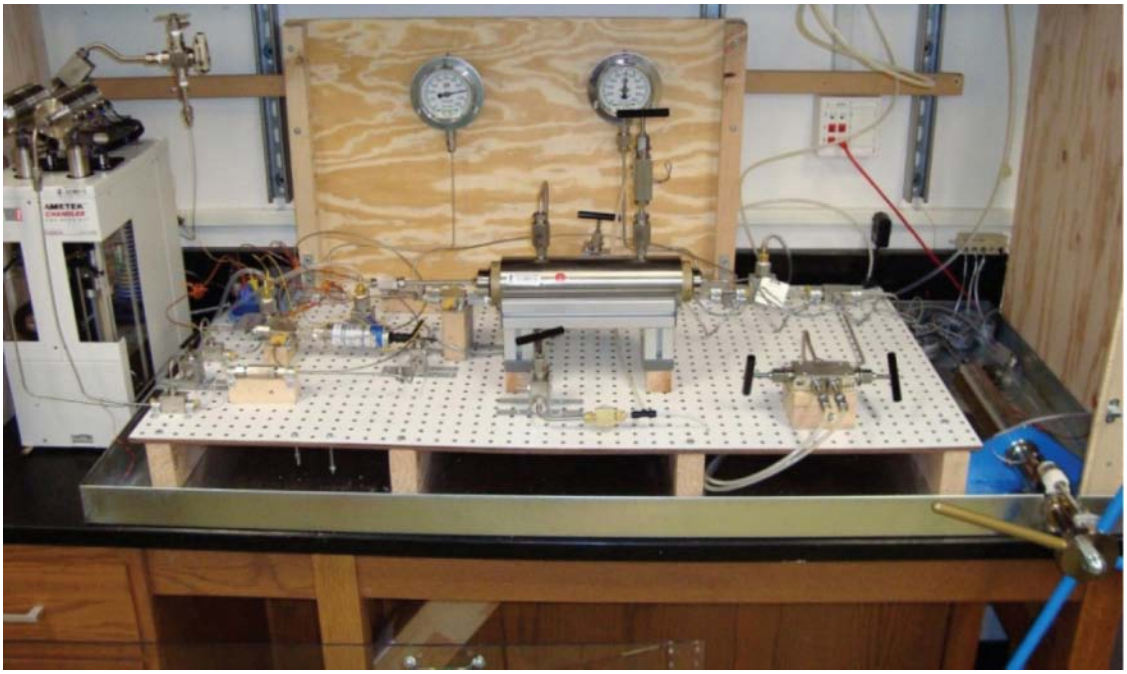

Figure 2.7: Photograph of hydrostatic permeability system. Quizix pump is on far left, Temco core holder is in the middle, and manual pressure generator is on the far right.

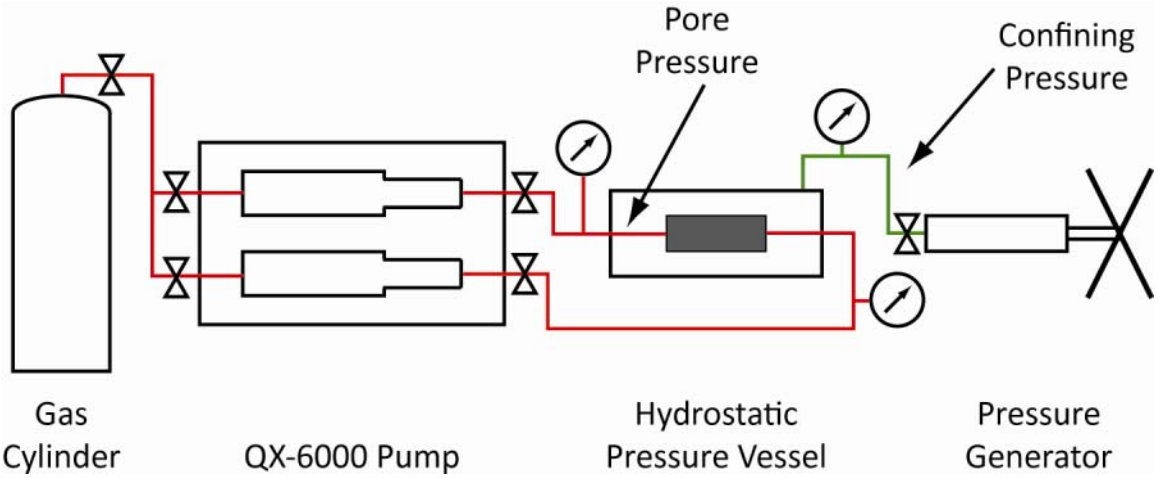

Figure 2.8: Schematic of hydrostatic permeability system. Pore pressure lines are in red and confining pressure lines are in green. Gas flows from one end of the rock sample to the other using the Quizix pump.

2.3.2 Adsorption Measurement Technique

We performed our adsorption experiments on crushed, dried Barnett shale samples. As is common in adsorption experiments, the samples were crushed to speed up adsorption equilibrium and dried to remove the effect of open storage conditions. After crushing the sample to between 100 and 250 microns, it was dried under vacuum at 105°C for at least three days, or until the weight of the sample stabilized. Approximately 30g of the crushed sample was placed into a 1-inch diameter copper jacket that had been soldered into a cylinder and placed on top of a stainless steel coreholder. Copper was used as the material next to the sample to prevent CO_2 interaction with an outer, heat-shrinkable viton jacket. Fine mesh screens were placed between the core holders and the sample to ensure that no particles were lost into the pore lines. After loading the second core holder on top of the sample, the viton was shrunk with a heat gun and o-rings and hose clamps were used to seal the jacket against grooves in the core holder. After loading the sample into the tri-axial system, the confining pressure was cycled up and down to 30 MPa until the sample exhibited only elastic deformation. The old jacket was removed and a new viton jacket was then shrunk around the compressed sample. After loading the system again, the sample was placed under vacuum to remove water and gas that may have contaminated the sample during final preparation.

The first step in the adsorption test was to measure the pore volume of the sample. The calibrated upstream reference cell, with volume V_R, was filled with He (a non-

adsorbing gas) at a given pressure. After waiting for equilibrium pressure, P_1, valve 2 was opened and the pressure dropped and stabilized at a lower pressure, P_2. The volume of the downstream sample cell V_S, which includes both the sample pore volume and the volume in the lines and core holders, was calculated as follows:

$$n = \frac{P_1 V_R}{Z_1 R T_1} \tag{2.4}$$

$$V_S = \frac{n Z_2 R T_2}{P_2} - V_R \tag{2.5}$$

where n is the total number of moles of He, Z is the compressibility factor, R is the universal gas constant, and Z is the temperature.

Having previously measured the volume in the pore lines and the core holders, the pore volume itself could be backed out. This process of gas expansion was repeated until a curve of pore volume versus pressure was generated for the entire pressure range to be measured for adsorption. While the difference in the confining pressure and the pore pressure was held constant at 3 MPa throughout all experiments, the pore volume of the sample may decrease as confining pressure increases because the Biot coefficient for the compacted sample is less than 1. In contrast, Ross and Bustin (2007) found a pressure-dependent increase in pore volume in gas shales due to what they argue is increased access to low aperture pores at higher pressures. With these two impacts potentially counteracting each other, it is important to directly measure pore volume at all pressures. We directly measured pore volume using helium and then corrected these helium-based pore volumes for additional changes in sample volume that we directly measured with mechanical sensors during the tests with N_2, CH_4, and CO_2. The sample deformations measured by the mechanical sensors can be caused by additional permanent plastic strain of the compacted sample, swelling during gas adsorption, or temperature variations within the pressure vessel. In our experiments, these corrections never exceeded 2% of the pore volume as measured with helium, and were generally well under 1%, indicating that the sample did not significantly deform during the tests.

Having measured the sample pore volume, it is possible to measure the amount of adsorption by expanding a known quantity of gas into the sample chamber and calculating the expected pressure, P_{exp} (if there were no adsorption) with the measured pressure, P_{meas}. If adsorption occurs, P_{meas} will be less than P_{exp} due to the high-density of the adsorbed phase. The amount of adsorption, n_{ads} is calculated as follows:

$$n_{ads} = n_{exp} - n_{meas} \tag{2.6}$$

$$n_{ads} = n_{exp} - \rho\left(P_{meas}, T_{meas}\right)\left(V_R + V_S\right) \tag{2.7}$$

where n_{exp} is the known quantity of gas first measured in the reference cell, n_{meas} is the calculated quantity of gas using P_{meas}, and ρ is the molar density of the gas at pressure P_{meas} and temperature T_{meas}.

The procedure above will calculate the excess, apparent adsorption. To calculate the absolute amount of adsorption, $n_{ads,absolute}$, we correct for the effect of the adsorbed phase reducing the available free pore space:

$$n_{ads,absolute} = \frac{n_{ads,apparent}}{1 - \dfrac{\rho_{gas}}{\rho_{ads}}} \tag{2.8}$$

where $n_{ads,apparent}$ is the apparent adsorption, ρ_{ads} is the density of the adsorbed phase, and ρ_{gas} is the density of the free gas phase. To estimate the density of the adsorbed phase, we use the hard sphere term, b, in the Redlich-Kwong-Soave equation of state, which is equivalent to the density at the critical temperature and pressure (Lin, 2009).

All molar densities were calculated using NIST's REFPROP program (NIST, 2007), which includes tables of the most accurate equations of state available for each of the gases used. After calculating the adsorption at the first pressure, the same procedure is repeated at a higher pressure each time, thus generating an entire adsorption isotherm. We measured adsorption isotherms on multiple samples using N_2, CH_4, and CO_2, the

most relevant gases for the issues of production performance, enhanced recovery, and greenhouse gas sequestration.

2.3.3 Permeability Measurement Techniques

We conducted our permeability experiments on intact, 1-inch diameter rock plugs. The ends of each sample were ground to be flat and parallel, and some samples were cut to smaller lengths to facilitate faster measurements. Each sample was dried under vacuum at 105°C until the weight stabilized to remove the effect of open storage conditions. The sample was placed into a thick Viton jacket and loaded into the core holder and pressure vessel. The sample was placed under vacuum for at least 24 hours and then saturated with the testing gas until reaching pressure equilibrium. We chose helium as our primary testing gas in order to remove adsorption effects from our measurements and to test effective stress impacts only. Separate tests were conducted to compare the permeability of a sample to He, CH_4, and CO_2 under identical conditions.

2.3.3.1 Static Darcy Flow Tests

We used a static, darcy flow measuring technique on a sample with higher permeability, greater than ~1 microdarcy for a ~1.5 inch sample. At that permeability, we were able to apply a constant pressure difference on the upstream and downstream sides and create flow rates that stabilized quickly and were large enough for our Quizix pump to measure accurately. The difference in pressure between upstream and downstream was usually 50 psi. The lowest pore pressures measured in our Darcy flow tests were 1000 psi; thus, the difference between upstream and downstream pressures was at most 5% of the average pore pressure, and usually much lower. We calculated permeability using the modified Darcy's law for a compressible gas:

$$k = \frac{2\mu Q P_{up} L}{A\left(P_{up}^{\ 2} - P_{down}^{\ 2}\right)} \tag{2.9}$$

where k is the permeability, μ is the viscosity of the fluid, Q is the flow rate, L is the sample length, A is the sample cross-sectional area, P_{up} is the upstream pressure, and P_{down} is the downstream pressure.

2.3.3.2 Dynamic, Pulse-Permeability Tests

For our lower permeability samples, a few hundred nanodarcy or lower, we used dynamic, pressure pulse testing. This technique was first developed by Brace et al. (1968) to measure permeability on granites. The principal is to create a dynamically changing flow across the sample and then fit the resulting pressure curves to a flow model, thus backing out permeability. In our case, we stepped the pressure on the upstream side by only 50 psi to minimize the impact of a non-uniform effective stress (and thus a non-uniform permeability) along the length of the sample. While it is typical to increase the upstream pressure by a certain initial amount and then allow the upstream pressure to decline as the downstream rises, we \ set up our experiments with a constant pressure on the upstream side, creating an effective infinite reservoir volume. This was done primarily to compensate for gas leakage problems on the upstream side of our system.

An example pulse-permeability test is shown in Figure 2.9. When the logarithm of the difference in pressure between the upstream and downstream sides is plotted versus time, the decay clearly follows a linear trend. This line can be fit by the following equation, after Brace et al.:

$$\Delta P(t) = \Delta P_0 \, e^{-\alpha t} \tag{2.10}$$

$$\alpha = \frac{k\,A}{\beta V_{down} L\,\mu} \tag{2.11}$$

where $\Delta P(t)$ is the difference in pressure between the upstream and downstream sides at time t, ΔP_0 is the difference in pressure between upstream and downstream at time $t = 0$, β is the compressibility of the gas, and V_{down} is the volume of the downstream reservoir.

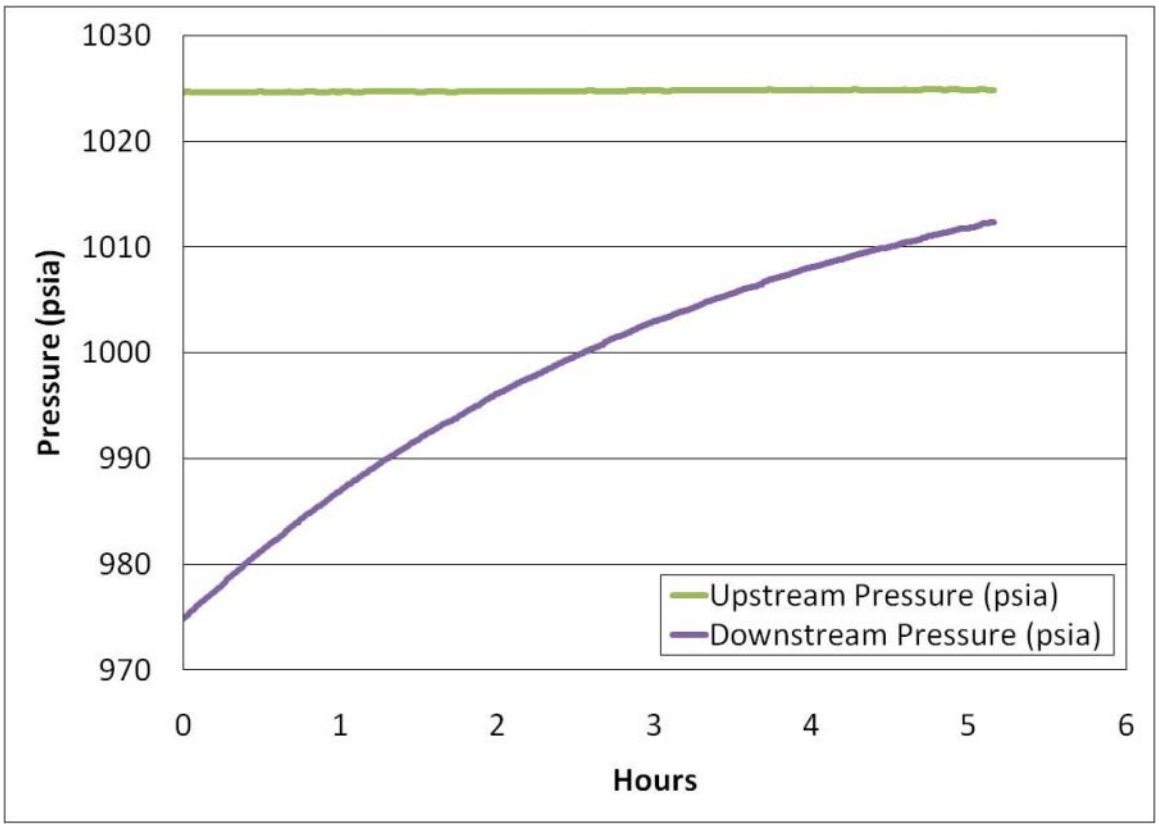

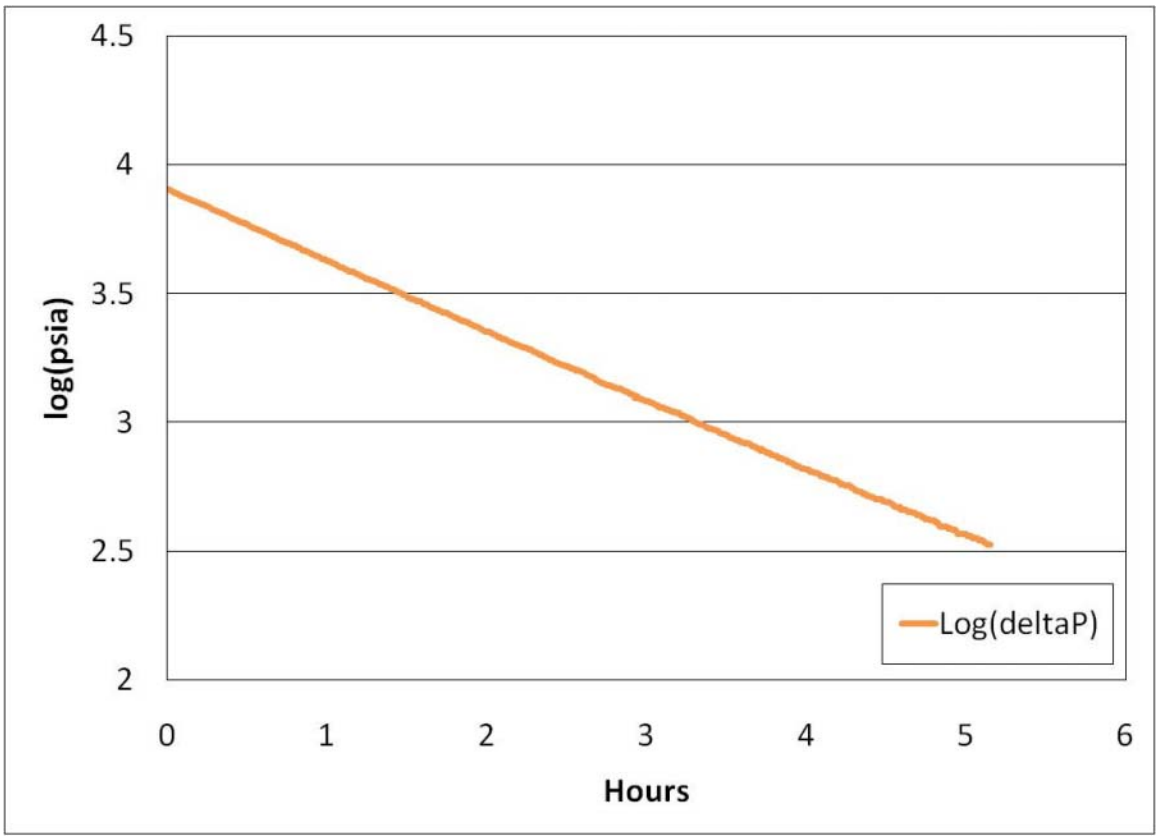

Figure 2.9: Pulse permeability example, showing the upstream and downstream pressure curves (top) and the logarithmic decay of the difference in pressure between the two reservoirs (bottom).

2.3.3.3 Effective Stress Law for Permeability

To calculate the relationship between effective stress and permeability, it is necessary to measure the permeability over a wide P_p and C_p space. An example of the stress space tested for a sample is shown in Figure 2.10. To calculate the effective stress parameter for permeability, we use the ratio of slope method following Kwon et al. (2001), using the following equation:

$$\chi = -\frac{\left(\partial \log k / \partial P_p\right)}{\left(\partial \log k / \partial C_p\right)} \tag{2.12}$$

The change in permeability with change in pore pressure at a given confining pressure is divided by the change in permeability with change in confining pressure at a given pore pressure. This ratio defines the relative sensitivity of permeability to changes in pore and confining pressures. The use of the logarithm of permeability is based purely on empirical fitting of the permeability decline as effective stress increases.

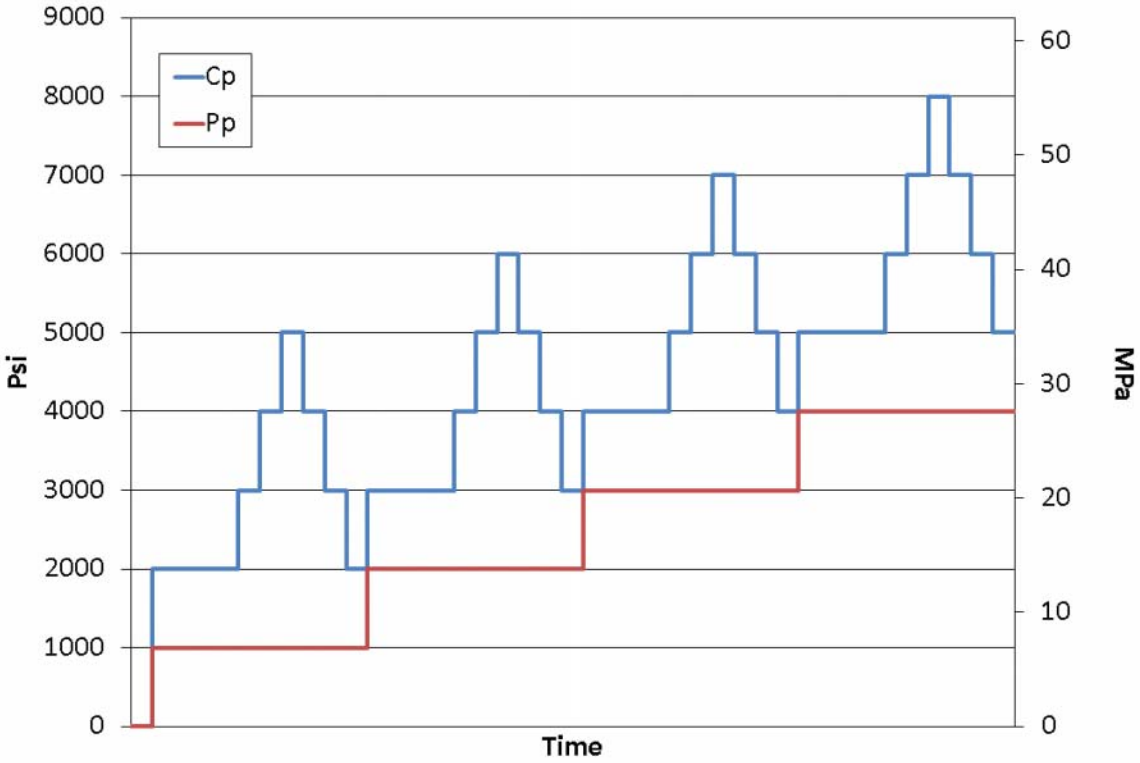

Figure 2.10: Confining pressure and pore pressure steps during permeability testing. There is a long hold for equilibrium after each pore pressure change. Tests are conducted with increasing effective stress and decreasing effective stress in order to control for hysteresis affects.

2.4 Adsorption Results

We measured adsorption on four Barnett samples: 19HVab, 22Vab, 26Vab, and 31Vcde. Adsorption of CH_4, CO_2, and N_2 were measured on samples 26Vab and 31Vcde, while only CH_4 and CO_2 were measured on 19HVab and 22Vab. While our experimental goals were to measure CH_4, CO_2, and N_2 adsorption on all samples, we were unable to complete adsorption measurements of N_2 on the latter two samples due to limited available time for experimentation on our shared tri-axial system. Fitted adsorption parameters are shown below in Table 2.3. Plots of measured absolute adsorption and model fits are shown below in Figures 2.11a-d.

Table 2.3: Fitted Langmuir and N-BET adsorption parameters.

	19HVab	22Vab	26Vab	31Vcde (adjusted)
Nitrogen				
P_L (psia)	-	-	1087	244
V_L (scf/ton)	-	-	11.8	12.0
Methane				
P_L (psia)	1281	702	1596	335
V_L (scf/ton)	47.4	55.0	39.2	45.4
Carbon Dioxide				
P_L (psia)	-	-	1254	-
V_L (scf/ton)	-	-	183.6	-
V_m (scf/ton)	27.9	35.3	37.5	55.5
C	2.7	10.1	4.0	9.0
N	9.5	9.3	3.4	10.2

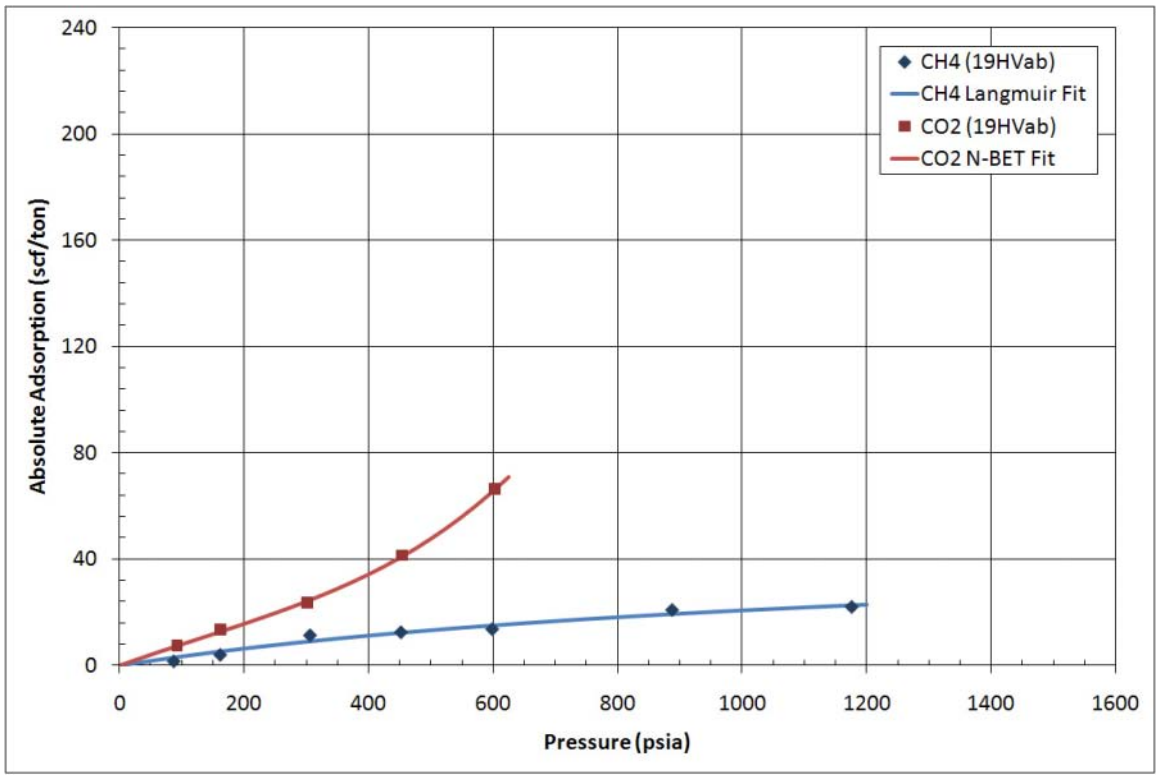

Figure 2.11a: Absolute adsorption of CH_4, and CO_2 for sample 19HVab. Measured data shown as points; fitted models shown as lines.

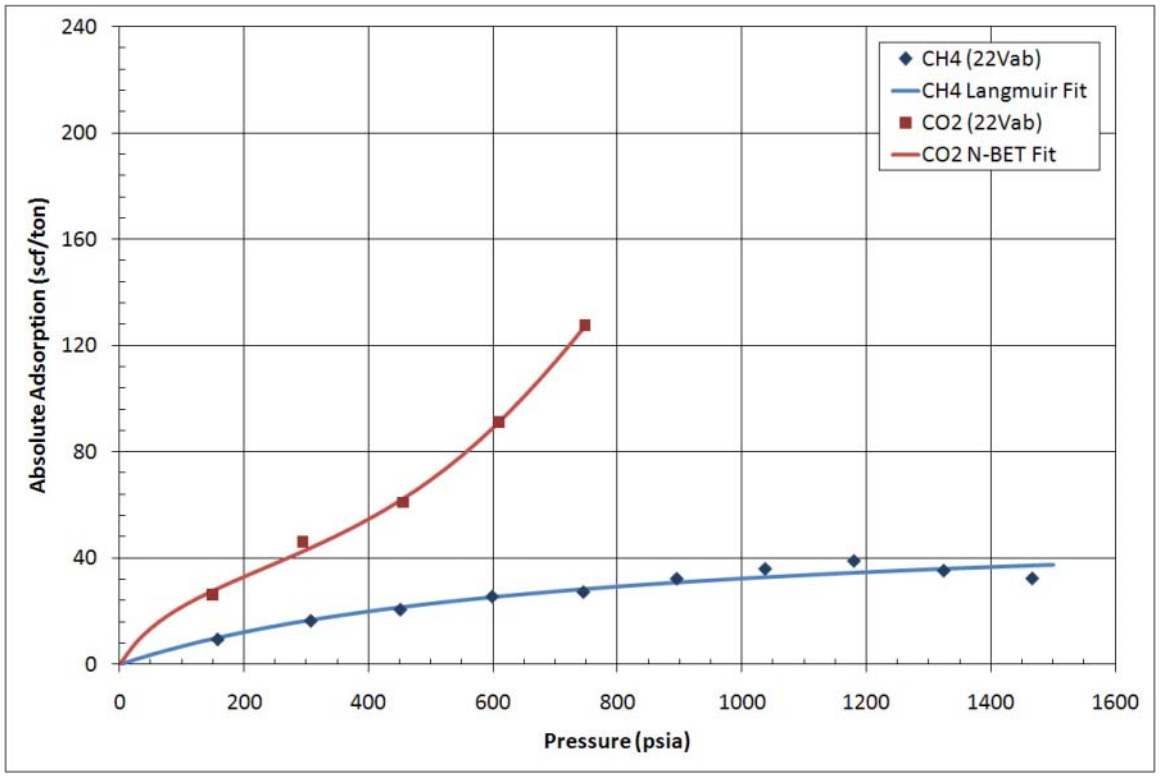

Figure 2.11b: Absolute adsorption of CH_4, and CO_2 for sample 22Vab.

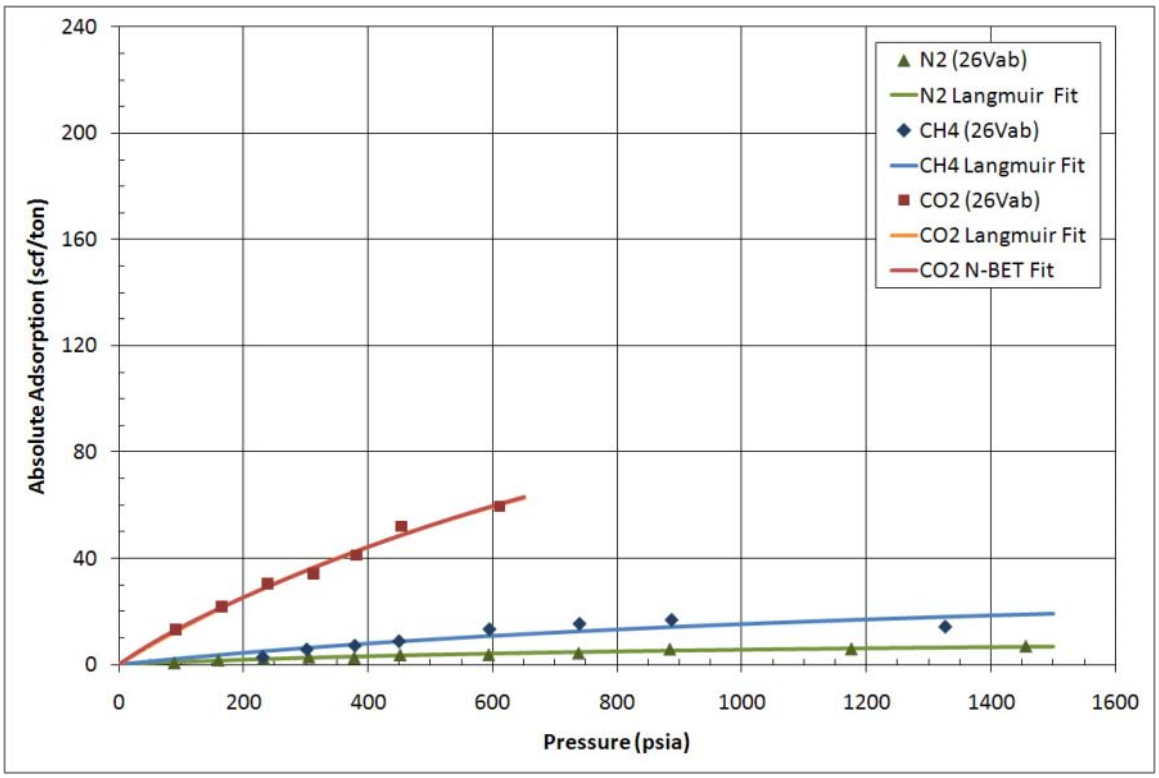

Figure 2.11c: Absolute adsorption of N_2, CH_4, and CO_2 for sample 26Vab.

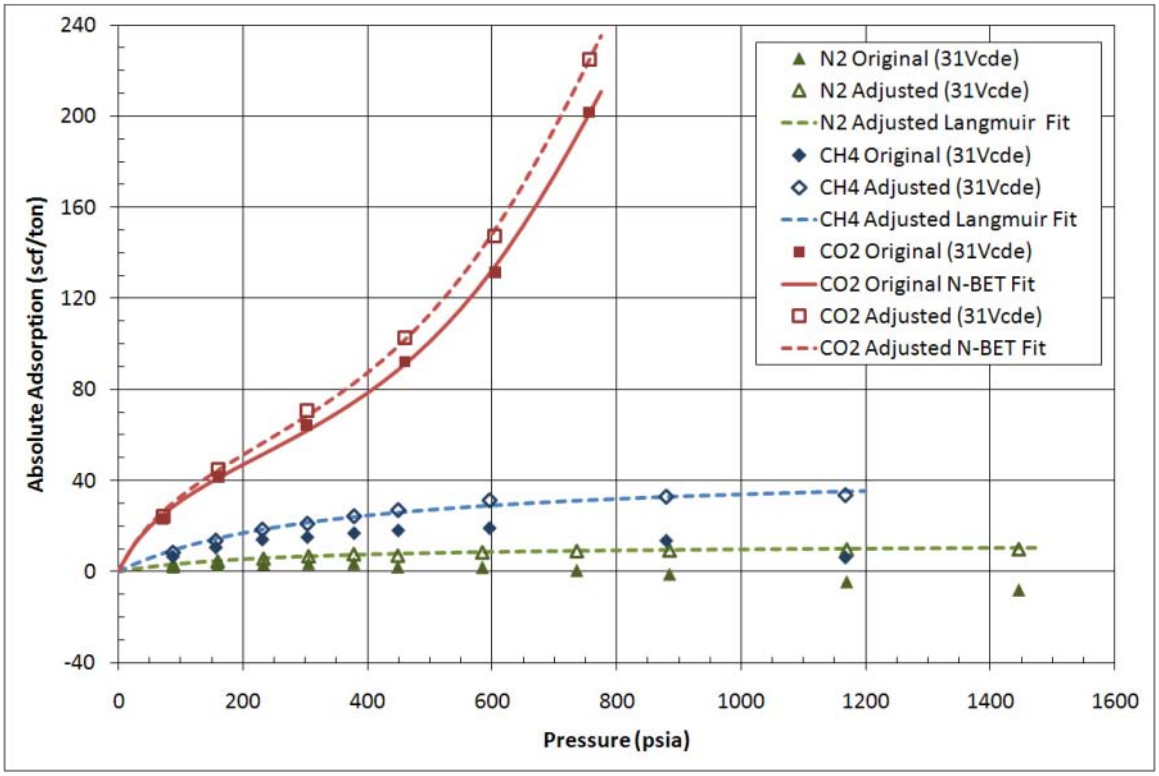

Figure 2.11d: Absolute adsorption of N_2, CH_4, and CO_2 for sample 31Vcde. Measured data shown as solid points; data adjusted with pore volume correction shown as hollow points. Fitted models of the adjusted data shown in dashed lines.

2.4.1 Sample 19HVab

As seen in Figure 2.11a, we measured adsorption of CH_4 and CO_2 on sample 19HVab. This sample demonstrated Langmuir-type adsorption of CH_4 and BET-type adsorption of CO_2, which we fit to an N-BET model. At 600 psi, sample 19HVab adsorbed 4.8x more CO_2 than methane.

2.4.2 Sample 22Vab

As seen in Figure 2.11b, we measured adsorption of CH_4 and CO_2 on Sample 22Vab. This sample demonstrated Langmuir-type adsorption of CH_4 and BET-type adsorption of CO_2, which we fit to an N-BET model. At 600 psi, sample 22Vab adsorbed 3.6x more CO_2 than CH_4.

2.4.3 Sample 26Vab

As seen in Figure 2.11c, we measured adsorption of N_2, CH_4, and CO_2 on Sample 26Vab. This sample demonstrated weak Langmuir-type adsorption of N_2, less than 4 scf/ton at 600 psi. This sample also demonstrated Langmuir-type adsorption of both CH_4 and CO_2, in contrast to the N-BET CO_2 adsorption seen for Samples 19HVab and 22Vab. At 600 psi, sample 26Vab adsorbed 5.5x more CO_2 than CH_4, the largest difference in preferential adsorption of the four tested samples.

2.4.4 Sample 31Vcde

As seen in Figure 2.11d, we calculated negative amounts of CH_4 and N_2 adsorption when using the original helium-derived pore volumes for Sample 31Vcde. Negative adsorption calculation has no physical meaning, so we spent significant time processing and analyzing the data from this sample to ensure that there were no measurement errors or sample volume changes during the test. Unable to create realistic adsorption curves despite this careful review, we sought explanations from the literature as to why apparent negative adsorption could occur. Ross and Bustin (2007) also found apparent negative adsorption. They suggested that negative adsorption could be the result of “molecular sieving”, where the pore space is not equally accessible to all molecules, in particular to CO_2 and CH_4 which have a larger molecular diameter than He. Kang et al. (2010) also report a possibly similar effect in a Barnett shale sample.

In the molecular sieving model, the pore volume that is available to He can be much larger than the pore volume accessible to an adsorbing gas. When using He-derived values of pore volume, adsorption will be cumulatively underestimated, especially if at high pressures He gains significant access to pore spaces that are not accessible to an adsorbing gas. At a given pressure, the pore volume available to an adsorbing gas like CH_4 would be lower than was available to He during calibration. Thus, the measured pore pressure of CH_4 after reaching equilibrium would be higher than expected, leading to a lower, or perhaps even negative, estimate of adsorption.

Ross and Bustin (2007) suggested that the pore volume estimate for the adsorbing gas tests could be adjusted until the measured adsorption reaches an expected shape, such as a Langmuir-type isotherm. Following this procedure, we adjusted the estimated pore volumes until reaching Langmuir-type isotherms. Figure 2.11d shows both the original data for sample 31Vcde as well as the corrected data points and curve fits. For the N_2 experiment, the pore volume estimate for the sample was reduced by 5.7%. For the CH_4 and CO_2 experiments, the pore estimate was reduced by 9.3%. These corrections create Langmuir-type results for the N_2 and CH_4 experiments and increase the total adsorption quantity for the CO_2 experiment. After the adjustments, sample 31Vcde shows greater N_2, CH_4, and CO_2 adsorption than any other sample. At 600 psi, 4.7x more CO_2 adsorbs than CH_4. Given the assumptions made in these corrections, the quantitative results for sample 31Vcde are accordingly more uncertain than for the other samples.

2.5 Permeability Results

We present permeability versus effective stress results for three Barnett shale samples, 27Ha, 31Ha, and 21Ha.

2.5.1 Sample 27Ha

Sample 27Ha was plugged parallel to the bedding of the Barnett shale. It was taken from a core section that is from approximately 8,621 feet true vertical depth (TVD). Images of sample 27Ha can be seen in Figure 2.13. This sample was somewhat unique in having an interbedded carbonate layer surrounded by organic shale matrix.

Compositionally, the sample was 56.7% quartz, 9.1% carbonate, 23.8% clay, and 3.8% TOC. The porosity of the sample as measured through density analysis was 8.6%.

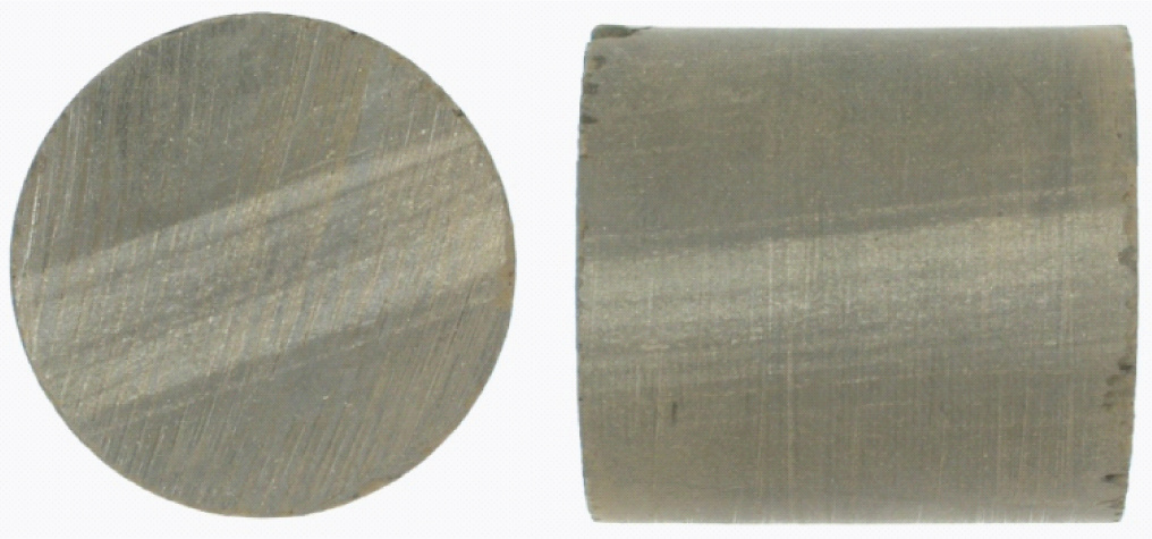

Figure 2.13: Sample 27Ha, demonstrating interbedded carbonate streak that seems to have a controlling impact on permeability. Sample diameter is 1-inch.

Figure 2.14 shows the permeability of sample 27Ha as a function of confining pressure and pore pressure. Tests on sample 27Ha were conducted using traditional darcy flow techniques. At 2000 psi confining pressure and 1000 psi pore pressure, permeability was approximately 1,850 nanodarcy (1.85 microdarcy). By the time the confining pressure reached 5000 psi, permeability declined by more than half to 850 nanodarcy. The curves for the other pore pressures follow a very similar shape, which means that a single function can fit the whole data set.

Applying the effective stress law calculation methods discussed above, the permeability effective stress coefficient for sample 27Ha is best fit as $\chi = 0.82 \pm 0.12$. Re-plotting the permeability results as a function of $\sigma_{eff} = C_P - 0.82P_P$ gives the result seen in Figure 2.15, demonstrating greatly improved fit versus the single effective stress parameter.

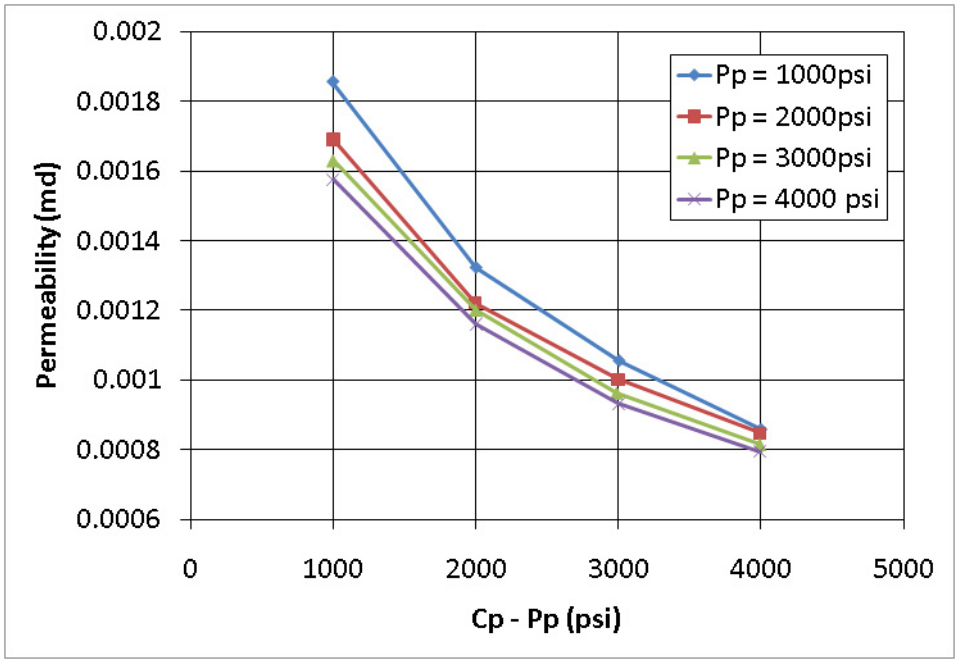

Figure 2.14: Permeability of sample 27Ha versus simple effective stress (Cp-Pp).

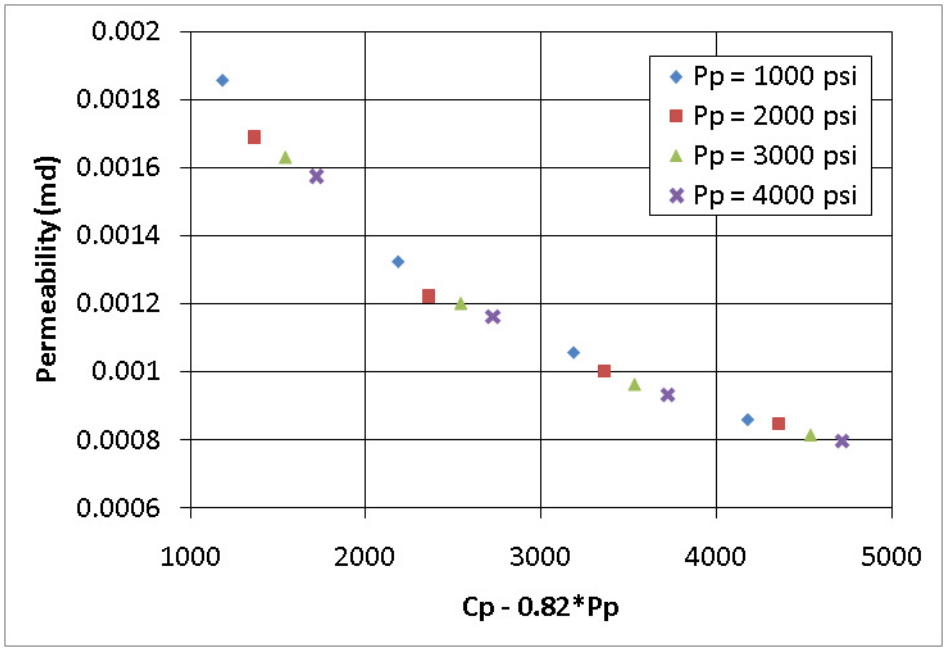

Figure 2.15: Permeability of sample 27Ha versus effective stress using empirically determined effective stress coefficient (Cp-0.82*Pp).

2.5.2 Sample 31Ha

Sample 31Ha was also plugged parallel to the bedding of the Barnett shale, like sample 27Ha. It is from a core section that was taken from approximately 8,634 feet TVD. Images of sample 31Ha can be seen in Figure 2.16. Originally 1.35 inches long,

sample 31Ha was cut in half before testing. This sample was of typical black, organic-rich Barnett shale composition, commonly seen in our sample population. Compositionally, the sample was 51.3% quartz, 0.5% carbonate, 37.3% clay, and 5.3% TOC. Its porosity was approximately 10.7% based on density analysis.

Figure 2.16: Sample 31Ha, a typical dark, organic-rich Barnett shale sample.

Figure 2.17 shows the permeability of sample 31Ha as a function of confining pressure and pore pressure. These measurements were taken using pulse-permeability techniques. At 2000 psi confining pressure and 1000 psi pore pressure, permeability is approximately 160 nanodarcy, 10x lower than permeability in sample 27Ha at the same conditions. By the time the confining pressure reached 5000 psi, permeability declined by almost half to 80 nanodarcy, a similar percentage decline as was seen in sample 27Ha for an equivalent confining pressure increase. The permeability curves at other pore pressures for sample 31Ha follow similar trends.

Using the techniques previously discussed, we found the permeability effective stress coefficient for sample 31Ha is best fit as $\chi = 0.68 \pm 0.17$. Re-plotting the permeability results as a function of $\sigma_{eff} = C_P - 0.68P_P$ gives the result seen in Figure

2.18, demonstrating greatly improved fit versus the single effective stress parameter, just as was seen for sample 27Ha.

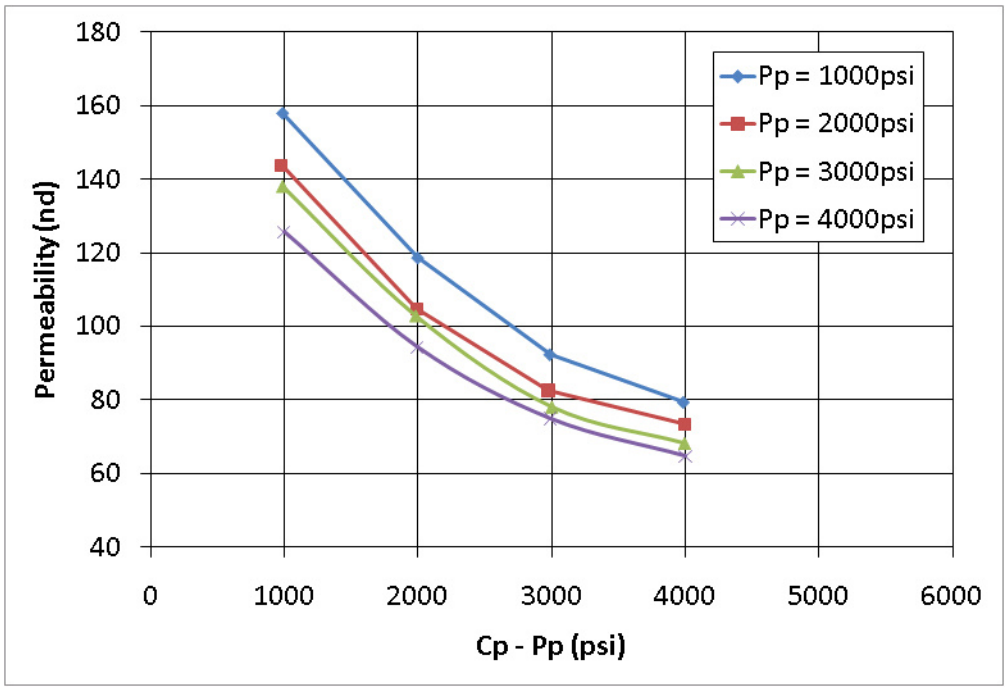

Figure 2.17: Permeability of sample 31Ha versus simple effective stress (Cp-Pp).

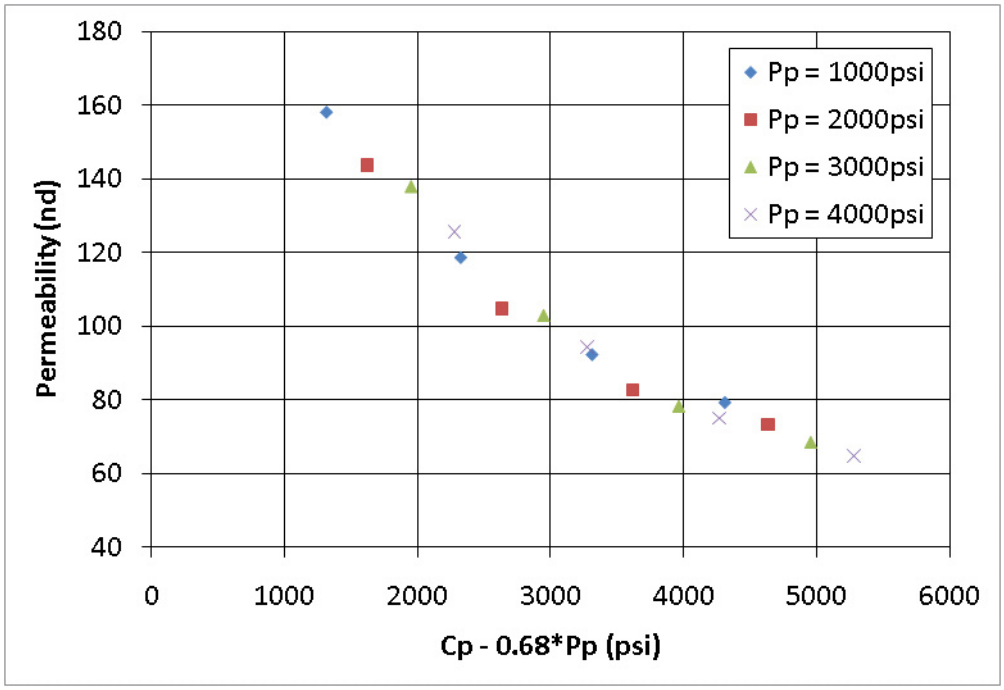

Figure 2.18: Permeability of sample 31Ha versus effective stress using empirically determined effective stress coefficient (Cp-0.68*Pp).

2.5.3 Sample 21Ha

Sample 21Ha was plugged parallel to bedding from a core section that was taken from approximately 8,586 feet TVD. Images of sample 21Ha can be seen in Figure 2.16. Compositionally, the sample was 42.7% quartz, 5.7% carbonate, 39.6% clay, and 3.0% TOC. This was the lowest % quartz, lowest % TOC, and highest % clay of any tested sample. In addition, the pyrolysis analysis indicated that the kerogen was more inert than in other samples. Porosity was approximately 9.0% based on density analysis.

Figure 2.19: Sample 21Ha, with lowest % quartz, lowest % TOC, and highest % clay of any tested sample.

Figure 2.20 shows the permeability the sample 21Ha as a function of confining pressure and pore pressure. Despite pre-stressing the sample before testing, the permeability declined permanently during a loading-unloading cycle with pore pressures at both 500 psi and 1000 psi. This permanent hysteresis made calculation of an effective stress coefficient for sample 31Vcde impossible. Possible compositional causes of this effect are discussed below in section 2.6.2.

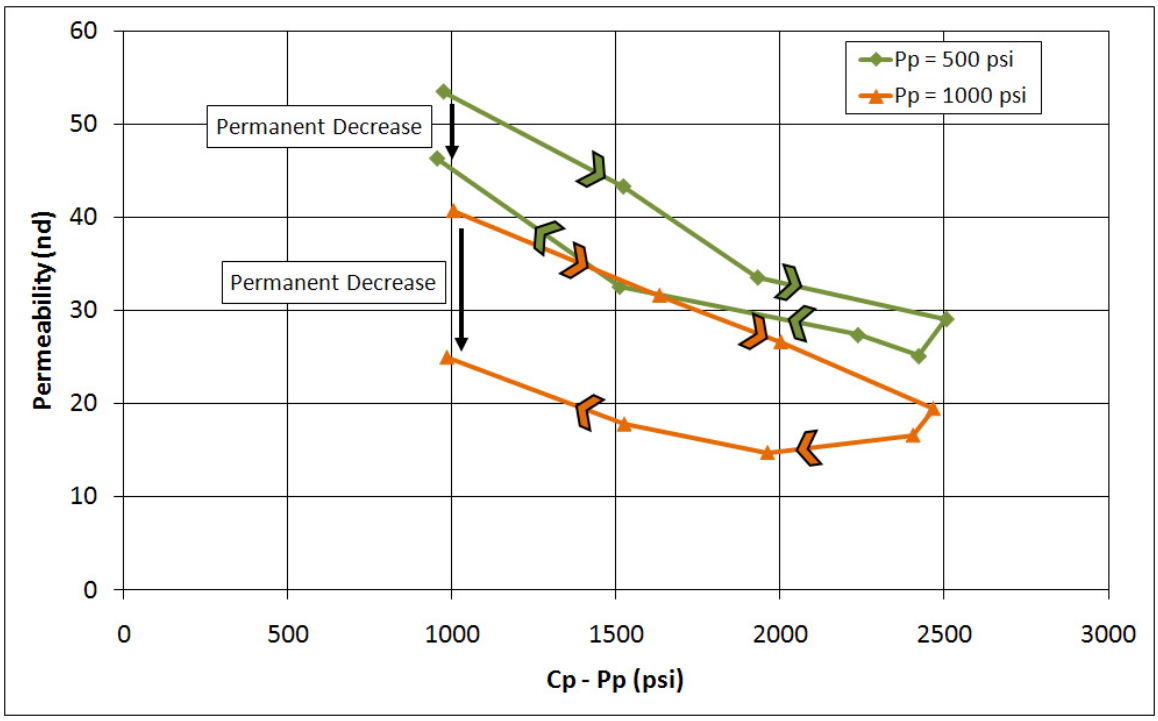

Figure 2.20: Permeability of sample 21Ha versus simple effective stress (Cp-Pp). Despite pre-stressing, permeability permanently declined as confining pressure was increased and then relieved. Calculation of a permeability effective stress coefficient was therefore impossible.

2.5.4 Permeability of CH_4 and CO_2 in the Barnett

At the end of primary permeability versus effective stress testing on samples 31Ha and 21Ha, we took a final permeability measurement at 2500 psi confining pressure and 500 psi pore pressure. After this test we evacuated the sample chamber under vacuum for several days and then filled it with CH_4, waiting up to a week for equilibrium. We then measured permeability at 2500 psi confining pressure and 500 psi pore pressure using the same techniques discussed above. CO_2 was then tested at the same conditions after another extensive period of vacuum and pressure equilibrium. Due to the extremely low ratio of sample pore volume to system reservoir volume, we expect errors resulting from gas adsorption to be less than 2%, and thus negligible for the analysis here (Cui et al., 2009).

As seen in Figure 2.21, permeability declined by about 30% when switching from He to CH_4 in both samples. When testing CO_2 as the pore fluid, permeability declined only slightly for sample 31Ha, but declined by more than half for sample 21Ha. The contrasting results on the impact of CO_2 on permeability suggest that further careful

study of CH_4 versus CO_2 permeability on the Barnett and other gas shales would be beneficial. Given the problems of hysteresis we saw in sample 21Ha while testing with He, it is possible that the decline in permeability with CO_2 is not a real effect. If this decline is real, however, it will have important implications for the injection of CO_2 into gas shales as well as the role organic-rich shales could play as a cap rock above carbon storage projects.

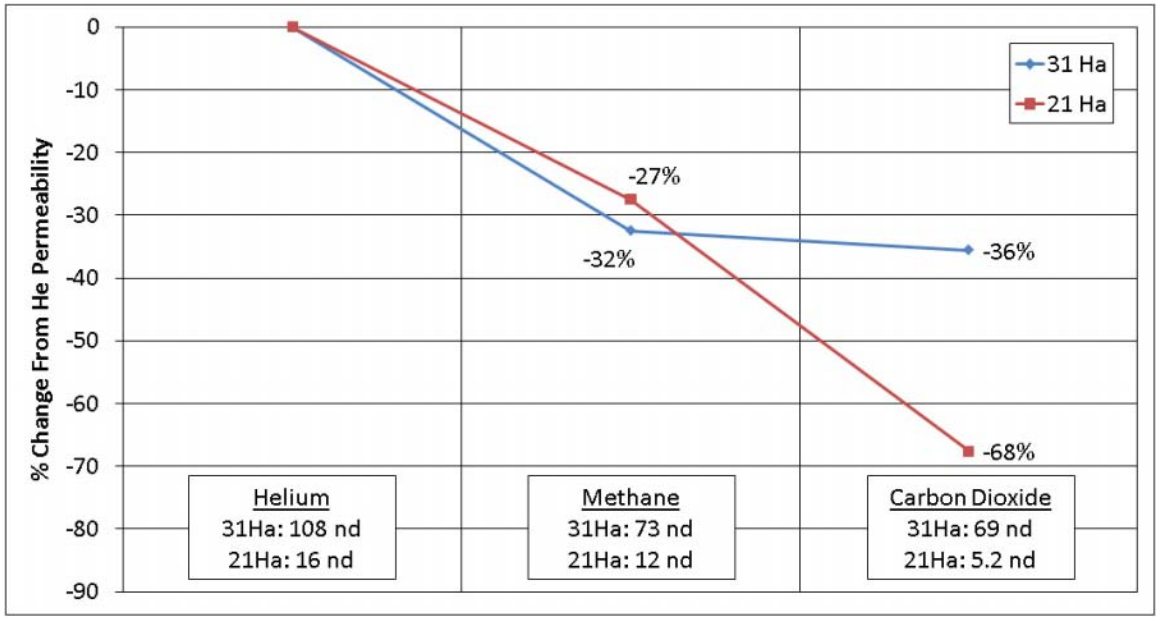

Figure 2.21: Permeability of samples of 31Ha and 21Ha with varying gas compositions. All tests conducted at same pore pressure (500 psi) and confining pressure (2500 psi).

2.6 Discussion

2.6.1 Adsorption

Our adsorption experiments are the first measurements of non-Langmuir adsorption on gas shale samples. As discussed above, adsorption is controlled by the distribution of pore sizes in the material, the effective molecular size of the adsorbing gas, and the combined attraction energy of the surface material and the adsorbing gas. We fit our results using a simple N-BET model that implies multilayer adsorption of CO_2 in these samples. However, we have no direct evidence for multilayer adsorption and have not provided a quantitative analysis for why multilayer adsorption might be occurring for CO_2, but not CH_4, in these samples. It may be possible to combine separate analysis of pore size distribution with detailed energy modeling to provide independent estimates of

the preferred energy state (and thus distribution of adsorption layers) for our gas shale samples. This work would provide greater insight into the rock properties that control the types of adsorption isotherms we found in our sample set.

Our measured adsorption capacities varied by as much as 50% among the four samples. It is likely that composition was the major controlling factor of these differences. Sample 31Vcde had the highest amount of TOC (5.7%) of any tested sample and also the largest measured adsorption capacity. As discussed above, this sample may also have exhibited “molecular sieving” of the different gases, perhaps caused by the pore size distribution in this high TOC sample.

Due to limitations of our modified tri-axial system, our adsorption studies were conducted at pressures well below the in situ pressures found in the Barnett shale. Nevertheless, the results are consistent with studies on gas shales conducted at both high and low pressure. Nuttall et al. (2005) found average CO_2 adsorption of 25-60 scf/ton on Appalachian gas shale samples. Our Barnett results show similar magnitudes within this pressure range, except with 3 out of 4 samples exhibiting BET-like adsorption isotherms, in contrast to the Langmuir behavior found by Nuttall et al. (2005). While we were running our experiments, Kang et al. (2010) published results of Barnett CH_4 and CO_2 adsorption at high pressures. As seen in Figure 2.22, if we extrapolate our own low pressure results out to the in situ pressures found in the Barnett, we find that for both CH_4 and CO_2 our results are reasonably predictive of the same adsorption capacities found by Kang et al. When extrapolated out to Barnett reservoir pressures, our N-BET models of CO_2 adsorption behave similarly to Langmuir-type models. Thus, it is possible that Kang et al. would have also found BET behavior had they measured adsorption at low pressures and not assumed a priori that adsorption would demonstrate Langmuir-type behavior. Studies that measure adsorption at both low and high pressures on the same samples would be beneficial in clarifying the full behavior of CO_2 adsorption in the Barnett shale.

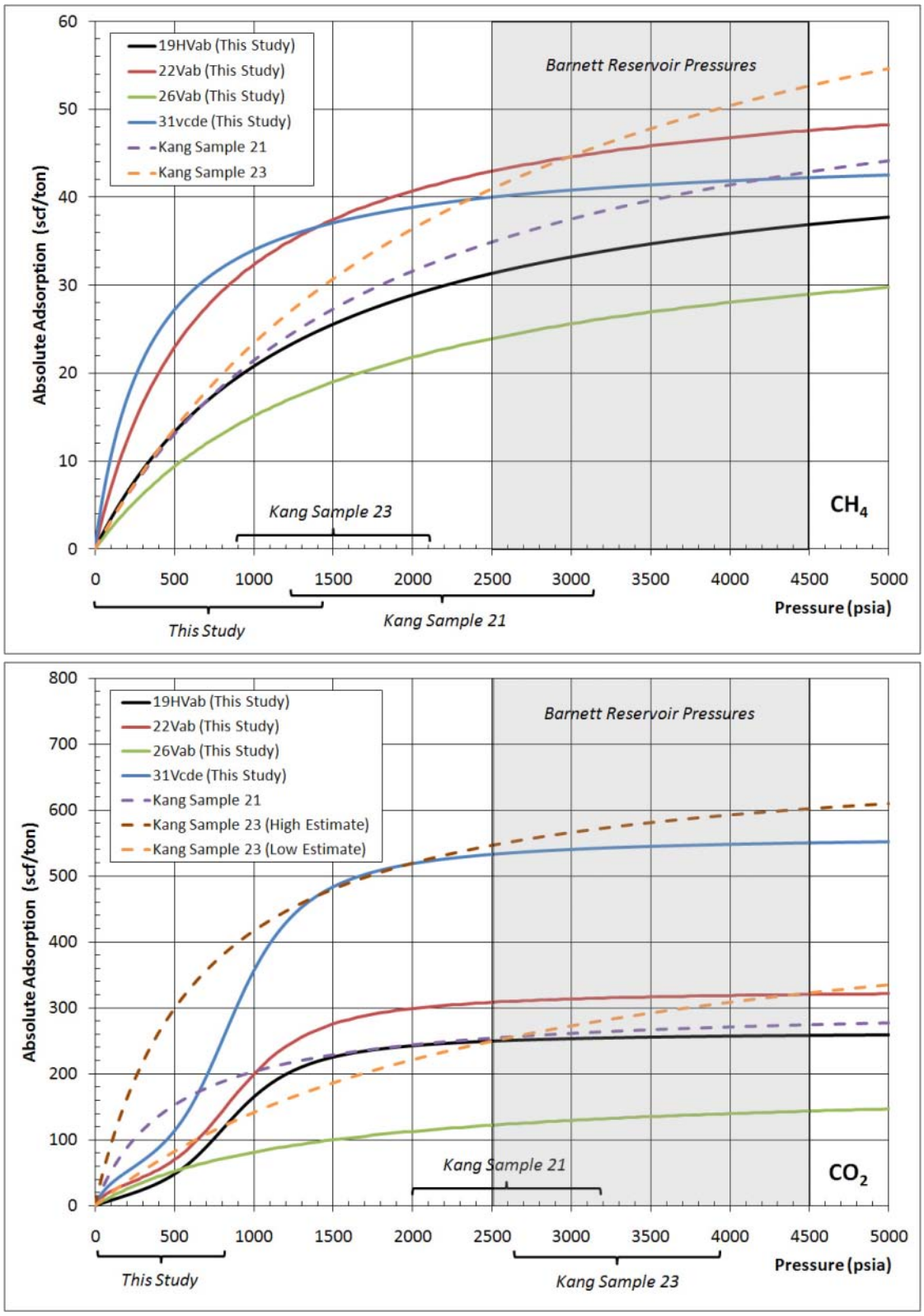

Figure 2.22: Comparison of adsorption results from this study with Barnett shale adsorption results reported in Kang et al. (2010). The ranges on the bottom axis show the spread of actual pressures measured for each tested sample. The extrapolation of our low-pressure results to in situ Barnett pressures lies within the same region as directly measured by Kang et al. for both CH_4 (top) and CO_2 (bottom).

If the extrapolations of our adsorption measurements are correct, we have demonstrated significant preferential adsorption of CO_2 over CH_4 at reservoir pressures. For example, at 4000 psi, sample 19HVab would show 7.1x preferential adsorption of CO_2, sample 22Vab would show 6.8x preferential adsorption, sample 26Vab would show 5.0x preferential adsorption, and sample 31vcde would show 13.1x preferential adsorption. With Kang et al. (2010) showing similar 5-10x preferential adsorption of CO_2, there is likely very significant capacity for CO_2 storage in the Barnett shale.

With these promising adsorption capacity results, further work on the practical feasibility of CO_2 injection and storage in the Barnett is necessary. Additional adsorption experiments are needed to determine if reservoir temperatures will significantly decrease the amount of adsorption or if in situ moisture inhibits or enhances the amount of adsorption. Important questions, such as the permeability of CO_2 in the Barnett and the time scale over which adsorption of CO_2 and replacement of CH_4 occurs, will need to be answered before the potential of the Barnett as a carbon storage reservoir is proven.

2.6.2 Permeability

Our initial hypothesis that Barnett shale rocks might demonstrate a permeability effective stress coefficient >1 does not appear to be correct. Both successful samples demonstrated permeability effective coefficients significantly <1. One caveat is that a Klinkenberg-type effect could be causing the reduction in permeability as pore pressure is increased that we observed in our samples (Klinkenberg, 1941). With the Klinkenberg effect, at low gas pressure the permeability is artificially elevated above the “true” permeability due to slippage of gas molecules along pore surfaces. In our experiments, we deliberately chose to measure permeability only at pore pressures of 1000 psi or above. These high pressures do not guarantee that the Klinkenberg effect has no impact, but it does likely minimize it compared to the effective stress effect (Cui et al., 2009). Further work is needed to separate Klinkenberg effects from effective stress effects on permeability in gas shales.

On the scale of these small intact samples, our estimates of the permeability effective stress coefficient indicate that compliant kerogen pores are likely not contiguous flow paths. In addition, we were able to successfully fit our experimental data using

methods derived from Darcy's law, suggesting that Darcy flow is still the major flow regime even in the very low permeability samples we tested. Sample 27Ha, with a heterogeneous, high permeability flow path, and sample 31Ha, a nearly homogenous organic-rich Barnett sample, behaved very similarly despite their significantly different compositions. Sample 31Ha, in particular, is likely from a section of the reservoir with very high productive capacity due to high TOC, high quartz, and low carbonate content. The measured permeability of sample 31Ha is also close to the typically quoted 100 nanodarcy permeability for Barnett shale matrix permeability. Other sections of the Barnett shale, therefore, are very likely to behave similarly to sample 31Ha.

Our relatively large, Darcy-type permeability measurements suggest that the dominant flow paths in our samples are likely much larger than typical gas shale pore sizes. We suggest that microcracks are likely to be the dominant flow path in these samples. The porous kerogen would then only be acting as a storage location of gas rather than an actual conduit of gas at this scale. To investigate the importance of these microcracks, further work combining permeability measurements with tracking of mechanical deformation would help elucidate the distribution and stress-sensitivity of these dominant flow paths. By tracking stress-strain relationships and then applying models of crack closure, it should be possible to directly match the mechanical changes with the measured permeability data. Given the damage that can be created in an intact sample during drilling and handling, it is important that future experimental work be conducted on samples treated as delicately as possible.

Since all of our studies were conducted on samples plugged parallel to bedding, it is important that the stress-sensitivity of permeability also be measured on a sample plugged perpendicular to bedding. While the Barnett does not exhibit particularly visible bedding planes, it is well known that vertical permeability can be significantly lower than horizontal permeability. Thus, if the dominant flow paths in the vertical direction differ from the flow paths in the horizontal direction, the relationship between effective stress and vertical permeability may follow a different trend than the relationship between effective stress and horizontal permeability.

As discussed above, we measured permanent decreases in permeability in sample 21Ha despite repeated pre-stressing. The composition of this sample may have influenced this behavior. This sample had the lowest % quartz, lowest % TOC, and highest % clay of any sample tested in this study. The low amount of quartz and high amount of clay suggest that this rock was mechanically weaker than the other tested samples, perhaps weak enough to deform plastically and creep during the long periods under stress during our testing. Sone and Zoback (2010a) continue to investigate creep in the same sample set discussed in this study. Our results on sample 21Ha suggest that measuring mechanical creep during a permeability test may be necessary to understand the behavior of samples similar to 21Ha.

2.7 Conclusions

We measured adsorption and permeability on Barnett shale samples. Our adsorption measurements focused on N_2, CH_4, and CO_2 with implications for potential storage of CO_2 and enhanced recovery of CH_4. Our permeability measurements were conducted with helium and focused on the stress-dependence of permeability in order to build an effective stress law for permeability.

We successfully measured adsorption on four Barnett shale samples. CH_4 and N_2 demonstrated Langmuir-type adsorption at magnitudes consistent with previous studies of the Barnett shale. Three of our samples demonstrated BET-type adsorption of CO_2 and one demonstrated Langmuir-type adsorption of CO_2, in contrast to all previous studies on CO_2 adsorption in gas shales that found Langmuir-adsorption. At low pressures (600 psi), we found preferential adsorption of CO_2 over CH_4 ranging from 3.6x to 5.5x. While our measurements were conducted at low pressures (up to 1500 psi), when our model fits are extrapolated to reservoir pressures they suggest similar adsorption magnitudes as have been found in previous studies. At these high reservoir pressures, there is very large preferential adsorption of CO_2 over CH_4 (up to 5-10x) suggesting a significant potential for CO_2 storage in gas shales like the Barnett if practical problems of injectivity and matrix transport can be overcome.

We successfully measured permeability versus effective stress on two intact Barnett shale samples. Both samples demonstrated permeability effective stress

coefficients less than 1, invalidating our hypothesis that there might be throughgoing flow paths within organic kerogen. The results suggest that microcracks are likely the dominant flow paths at these scales, and further work is needed to understand the size and distribution of these microcracks and how they are influencing permeability as the effective stress changes.

Chapter 3

GEOLOGICAL, GEOPHYSICAL, AND GEOMECHANICAL CHARACTERIZATION OF BARNETT SHALE STUDY AREA

Abstract

We integrated geological, geophysical, and geomechanical data in order to characterize the rock properties in our study area and model the stress state in the reservoir before hydraulic fracturing occurred. Five parallel, horizontal wells were drilled in the study area and then fractured using three different techniques. Only the middle well (Well C) was comprehensively logged, including both image and sonic logs. Using the image logs from the Well C vertical pilot and the Well C horizontal section, we mapped natural fractures and wellbore failures. We then used the principles of geomechanical modeling to constrain the stress state in the reservoir. While there was some variation in the stress state along the length of the well, we were able to determine a best fit stress state of $P_P = 0.48$ psi/ft, $S_V = 1.1$ psi/ft, $S_{Hmax} = 0.73$ psi/ft, and $S_{hmin} = 0.65$ psi/ft. Applying this stress state to the mapped natural fractures indicates that there is significant potential for induced shear slip on natural fracture planes in this region of the Barnett, particularly close to the main fracture plane where the pore pressure increase during hydraulic fracturing is likely to be very high. The geological, geophysical, and geomechanical analyses presented in this chapter provide input parameters to the modeling and analysis conducted in Chapters 4 and 5, as well as general context for our studies of this region of the Barnett shale.

3.1 Introduction

Chapters 3, 4, and 5 of this dissertation are focused on a microseismically monitored hydraulic fracturing project in the Barnett shale that was conducted in the fall of 2008. The goal of the project was to directly compare three different methods of hydraulic fracturing on wells that were drilled in the same small field area. While our

primary analysis of this fracturing project is presented in Chapters 4 and 5, we present in this chapter background characterizations of the field area to help with the interpretation of results from our primary analyses. After reviewing the drilling, completion, and data collection programs of the project, we present the geological, geophysical, and geomechanical characterization of the study area.

3.2 Overview of Study Area Wells

3.2.1 Drilling and Completions Program

Five horizontal wells were drilled as part of the project. A map view of the well paths is presented in Figure 3.1. The horizontal well sections were drilled at a depth between 5700-5750 ft and at an azimuth of approximately 325°. Each well is ~3000 feet long and separated by ~500 feet from the other wells. Well C was first drilled as a vertical pilot through the Barnett and then backed off and drilled horizontally. Within the Barnett, each well was drilled with a 7 7/8 inch bit, lined with steel casing, and then cemented in place.

After drilling, each well was hydraulically fractured in either 10 or 11 stages. Each stage represented an isolated section of the well, ~300 feet long, with six perforation clusters spaced 50 feet apart. A more detailed description of the fracturing program is presented in Chapter 4, but a brief overview is presented here. Wells A and B were fractured using a "simulfrac" technique, where the stages of both wells were fractured at the same time, moving from toe to heel in 10 stages overall. Wells D and E were fractured using a "zipperfrac" technique, where the stages of the two wells were alternately fractured, moving from toe to heel in 10 stages for each well. Well C was fractured last of the five wells in 11 total stages. To isolate each stage a packer and plug system was used, with a ceramic plug at the toe of each stage and an inflatable packer at the heel end. After fracturing, each well had the plugs drilled out and was shut-in before production began. Production for the wells did not begin until almost a year later in November of 2009, despite the completion of drilling and fracturing in November of 2008.

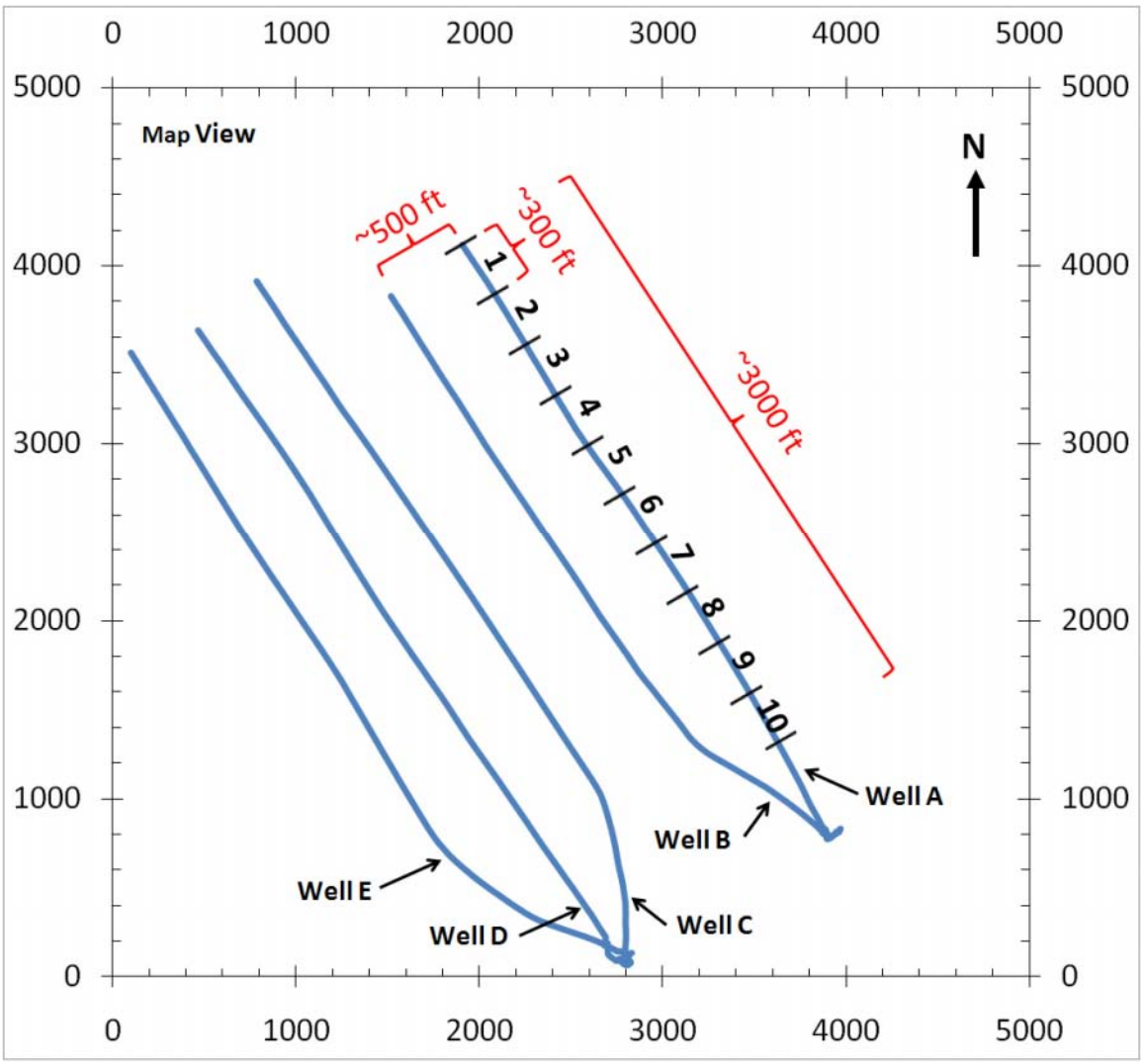

Figure 3.1: Project area well paths. The producing sections of each well were ~3000 ft long and divided into stages 300 ft long. The lateral spacing between wells was ~500 ft.

3.2.2 Data Collection Program

While all wells had a gamma ray and mud log taken during drilling, Well C was the only one of the five wells to be comprehensively logged. The Well C vertical pilot section was logged with Formation MicroImager (FMI), dipole shear sonic imager (DSI), gamma ray, neutron porosity, density, and resistivity tools. The Well C horizontal section was logged with an FMI, but not with any other tools. Simultaneous to the hydraulic fracturing, a seismic array was deployed to detect microseismic events in the reservoir generated during fracturing. More details of this program are presented in Chapter 4.

3.3 Geological Characterization

To place the work presented in Chapters 2, 4, and 5 in a fuller context, we present here an overview of the geology of the Barnett shale and detail the reasons it has been such a prolific and successful gas producer. After reviewing this general history, we will place the project analyzed in Chapters 4 and 5 into its own specific geological context.

3.3.1 Geology of the Barnett Shale

There are several comprehensive reviews of the geology of the Barnett shale, including Montgomery et al. (2005), Bowker (2007), Loucks and Ruppel (2007), and Pollastro et al. (2007). This geologic overview is a summary of the information presented in these four papers.

The Barnett shale is an organic and silica-rich black mudstone of middle to late Mississippian age. Long considered the probable source rock for several regional oil and gas reservoirs, it is located in the Forth Worth Basin of north-central Texas. The location and structural setting can be seen in Figure 3.2. The basin is bounded to the east by the Ouachita fold and thrust belt, to the north by basement uplift arches, to the west by the Bend arch, and to the south by the Llano uplift. The basin was formed during the late Paleozoic Ouachita orogeny, a thrust-fold deformation sequence related to the formation of Pangaea. Structural features within the basin itself include the Mineral Wells fault in the northeast, a basement fault that was periodically reactivated during the late Paleozoic. Minor normal-faults and graben blocks, present throughout the basin, locally impact basin structure and lithology. Open fractures and faults are rare within the Barnett, with nearly all fractures seen in core and logs filled with calcite.

A generalized stratigraphic profile of the Ft. Worth Basin and the Barnett shale can be seen in Figure 3.3. The Barnett itself is of Mississippian age, and lies on top of two Ordovician carbonate groups, the dense, crystalline Viola-Simpson formation and the porous, water-bearing Ellenberger formation. The Viola-Simpson thins when moving NE to SW in the basin and eventually pinches out completely, leaving the Barnett directly on top of the Ellenberger. Also pinching out from NE to SW is the Forestburg limestone, a carbonate debris flow formation dividing the Barnett into upper and lower intervals. The

Barnett itself thickens to the northeast, reaching a maximum thickness of more than 500 feet at depths greater than 8000 feet.

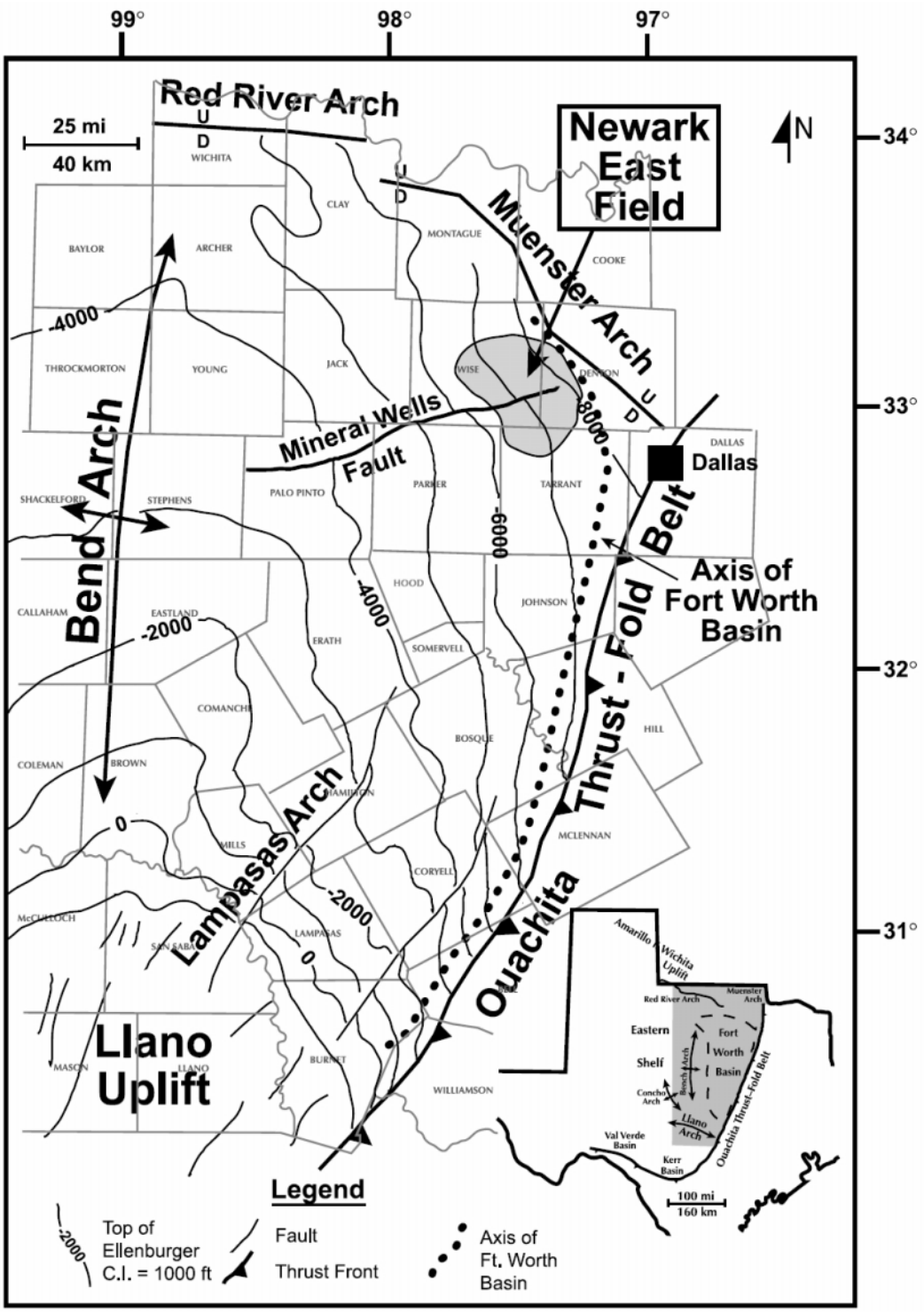

Figure 3.2: Ft. Worth Basin location and major structural features. Contour lines show depth to bottom of Barnett shale. Newark East Field was the original core Barnett producing area. Source: Montgomery et al. (2005).

The Barnett shale consists of siliceous organic-rich mudstone, limestone, and minor dolomite. The shale intervals generally contain high silica (35-50%), relatively low clay (<35%), and significant organic carbon (3-10%). Thin carbonate debris flow layers are common in some areas of the basin. The organic-rich portions of the reservoir average 5-6% porosity and generally less than 25% water saturation. The deeper portions of the reservoir have seen greater thermal maturity, with dry gas and gas-oil maturities found in the productive NE portions of the reservoir.

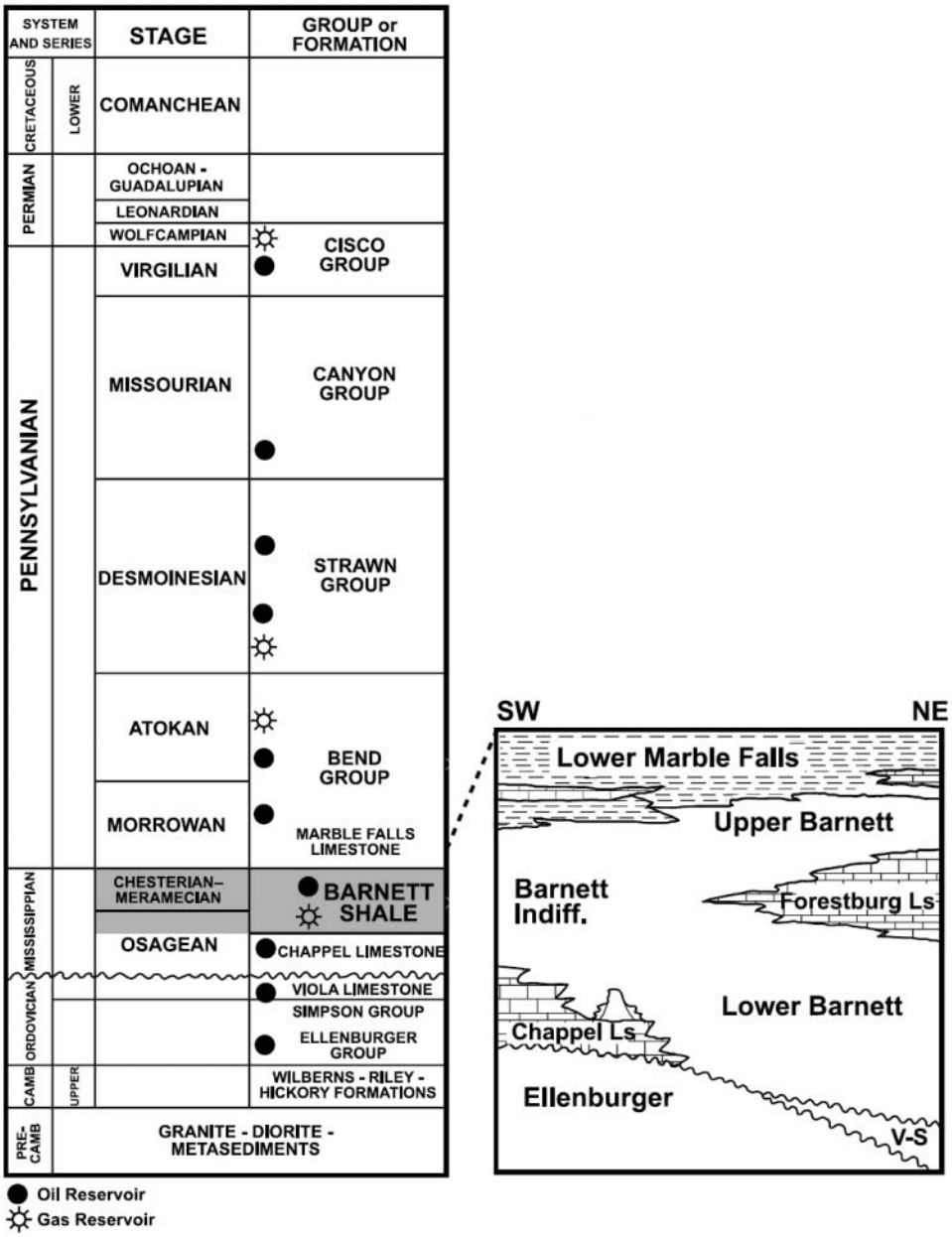

Figure 3.3: Generalized stratigraphy of the Ft. Worth Basin. Inset shows detailed stratigraphy above, below, and within the Barnett shale. Source: Montgomery et al. (2005)

3.3.2 Study Area Geological Context

A lithologically interpreted gamma ray log for the study area analyzed in Chapters 3, 4, and 5 is shown in Figure 3.4. The Barnett is ~320 ft thick in the study area, with the top of the reservoir at ~5620 ft and the bottom at ~5940 ft. The study area is in the region of the basin where there is an undifferentiated Barnett directly overlying the Ellenberger. Thus, to avoid fracturing into the Ellenberger and producing excessive water, the horizontal sections of Wells A-E were drilled into the upper portion of the reservoir at ~5725 feet. Since no core was taken at this location, geologic characterization is based on the comprehensive set of well logs taken in the Well C vertical pilot. The FMI log, discussed in detail below, indicates that there are fairly regular healed fractures in the formation.

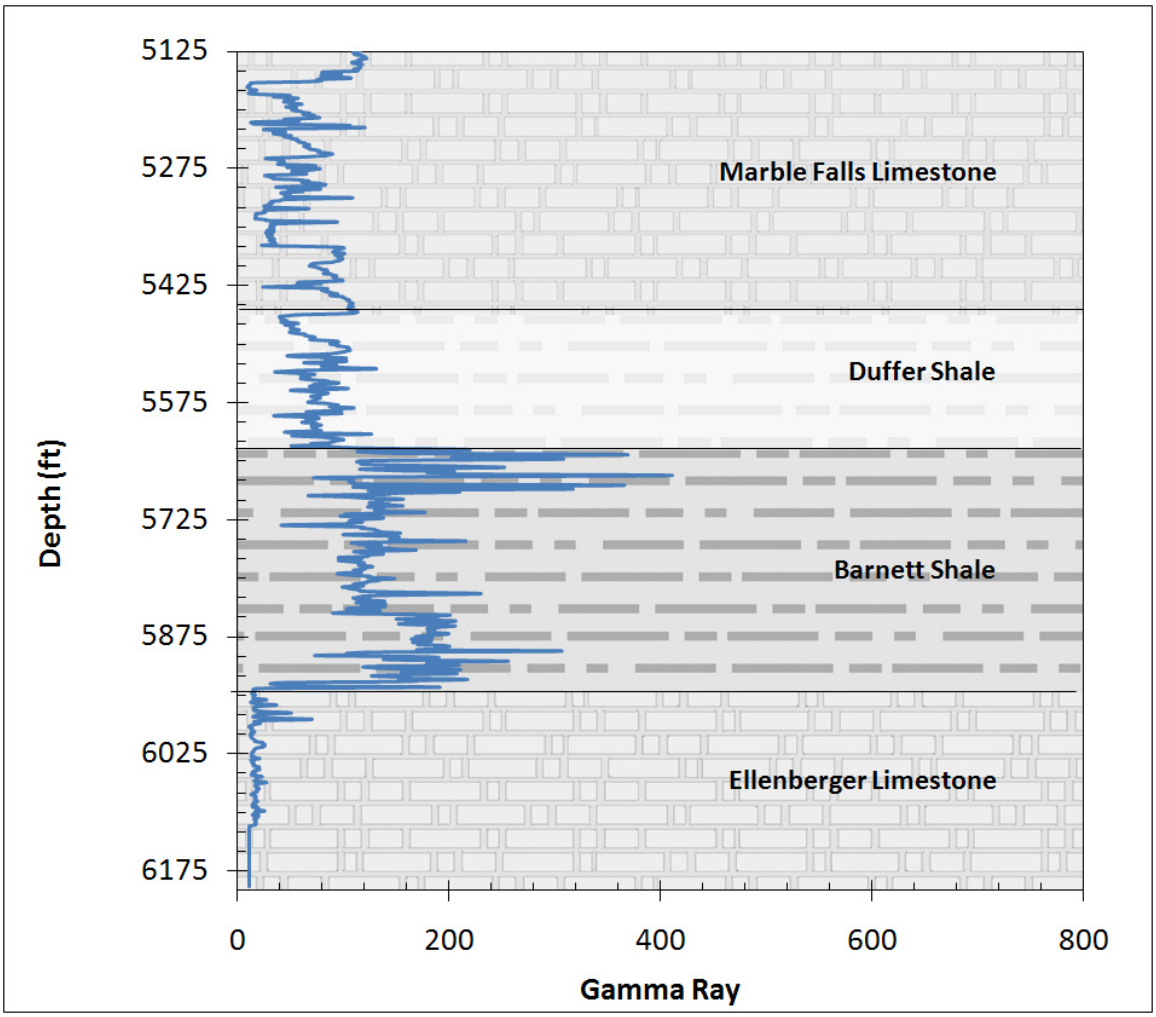

Figure 3.4: Gamma ray log from the Well C vertical pilot, showing interpreted geologic intervals.

3.4 Geophysical Characterization

In support of the microseismic analysis done by the microseismic contractor, the Barnett study area was also analyzed for its geophysical properties. The primary goal of this analysis was to develop velocity models to be used in locating detected microseismic events. The dipole shear sonic log, along with the geological data collected by the rest of the logging suite, was used to build a velocity model for the Well C stages by the microseismic contractor. These 1-D velocity models (Figure 3.5) were calibrated on a stage-by-stage basis using the perforation shots deployed during the fracturing procedure. The velocities estimated within the Barnett are comparable to values reported in the literature (Goodway et al., 2006) and also those measured in the lab (Sone and Zoback, 2010a). Similar 1-D velocity models were built for the stages of the other wells, but without access to sonic logs these models relied on the gamma ray logs, perforation shot calibrations, and geologic inferences. The 1-D models for the Well C stages contained four separate velocity intervals within the Barnett section, while the models for the other wells contained only 1 or 2 intervals for the Barnett. Thus, it is likely that the systematic location errors from velocity structure misfit are smaller for the Well C microseismic events than for events from the other wells. Velocity anisotropy was not incorporated in the microseismic location analysis, likely adding additional systematic error to the mapped event locations.

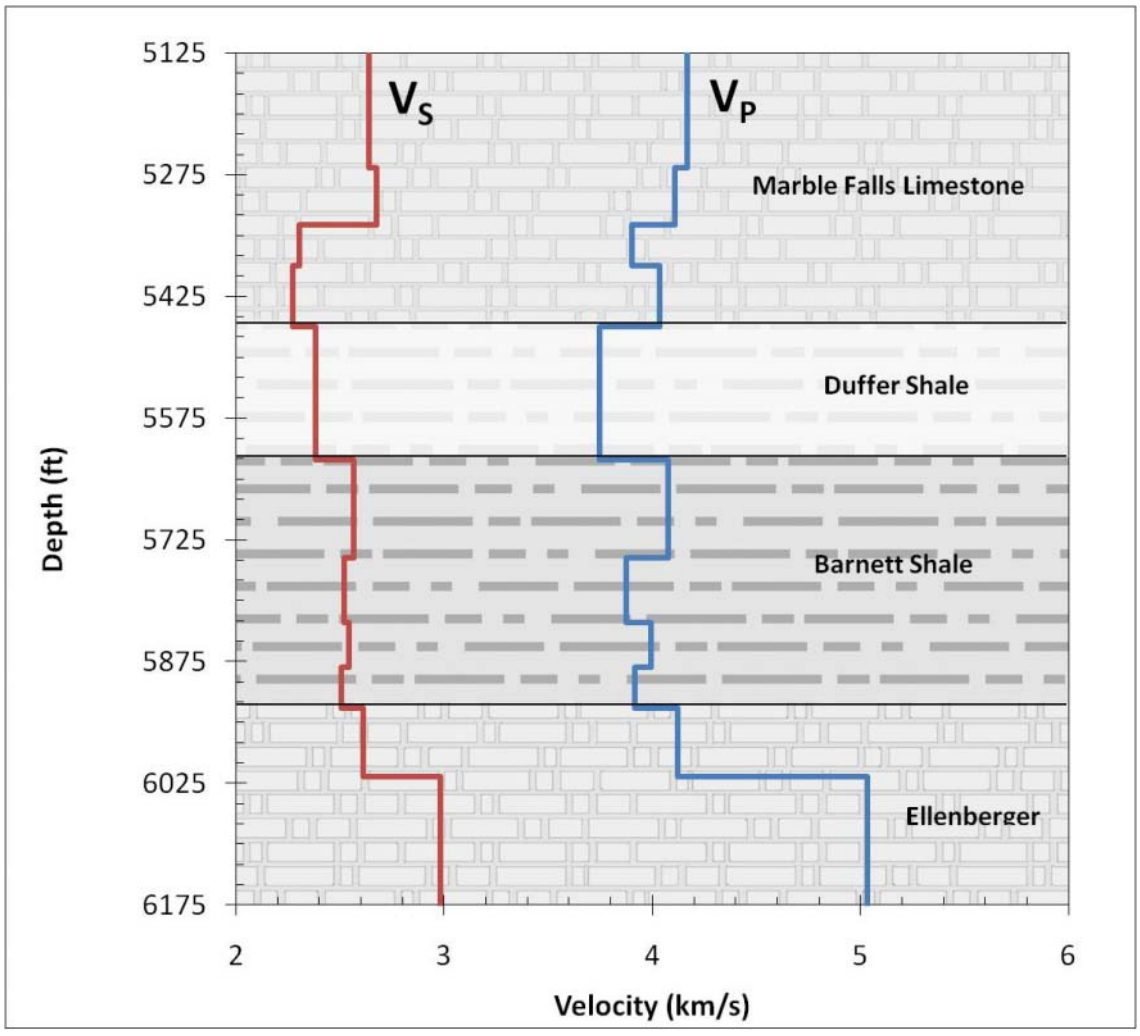

Figure 3.5: Velocity model used for stages 4-10 of the Well C microseismic location analysis.

3.5 Geomechanical Characterization

To properly interpret the hydraulic fracturing and microseismicity data from the study area, it is necessary to build a geomechanical model of the reservoir that includes the mechanical rock properties along with the state of in situ stress. This model is particularly useful in understanding the evolution of stress before, during, and after hydraulic fracturing. After giving a conceptual overview of geomechanical model creation, we will cover the methods, data, and results of the individual properties analyzed for our Barnett shale study area. We follow the general procedure outlined in Zoback et al. (2003) to determine the orientation and magnitudes of the principal stresses in the reservoir. Additional rock properties used in the stress determination are based on well logs, lab tests, or the published literature on the Barnett shale.

3.5.1 Mechanical Properties

The mechanical properties we used in our geomechanical modeling are listed in Table 3.1 We estimated these mechanical properties using the well logs from the study area, lab analyses from other Barnett samples, and reasonable estimates from the gas shale and rock mechanics literature.

Table 3.1: Mechanical properties used in geomechanical modeling.

Poisson's Ratio	Young's Modulus (GPa)	Coefficient of Thermal Expansion (1/degC)	Biot Coefficient	Sliding Friction	Internal Friction
0.23	40	0.0000072	1	0.75	1

3.5.2 Pore Pressure

The in situ pore pressure (P_P) within a gas shale like the Barnett is very difficult to measure accurately due to its very low intrinsic permeability. The P_P is often assumed to be roughly equal to the mudweight when there is neither gas intrusion nor loss of circulation at that weight. In the Well C vertical pilot, the static mudweight used while drilling through the Barnett shale ranged from 9.25 ppg (0.482 psi/ft) to 9.30 ppg (0.484 psi/ft), with no lost circulation or gas intrusion reported at these values. In the Well C horizontal sections, the static mudweight ranged from 9.4 ppg (0.489 psi/ft) to 9.75 ppg (0.507 psi/ft), again with no lost circulation or gas intrusion reported. Montgomery et al. (2005) reported overpressure up to 0.52 psi/ft based on one of the few attempts to directly measure the pore pressure in the Barnett shale. While there is uncertainty in the pore pressure in our field area, we used a lower bound for P_P of 0.48 psi/ft based on the mudweight constraints.

3.5.3 Vertical Stress Magnitude

Due to the free surface of the earth, one of the principal stresses is usually oriented vertically. The magnitude of this principal stress can be calculated from the weight of the overburden:

$$S_V = \int_0^z \rho(z)\, g\, dz \tag{3.1}$$

where S_V is the vertical stress magnitude, $\rho(z)$ is the density at depth z and g is gravity (Zoback et al., 2003). The density log from the Well C vertical pilot is shown in Figure 3.6a and the corresponding S_V plot is shown in 3.6b. (Since the density log began at 100 ft MD, a density of 1.9 g/cc was assumed for the first 100 ft.) Within the reservoir interval of 5620 to 5940 ft, S_V is nearly constant at 1.1 psi/ft.

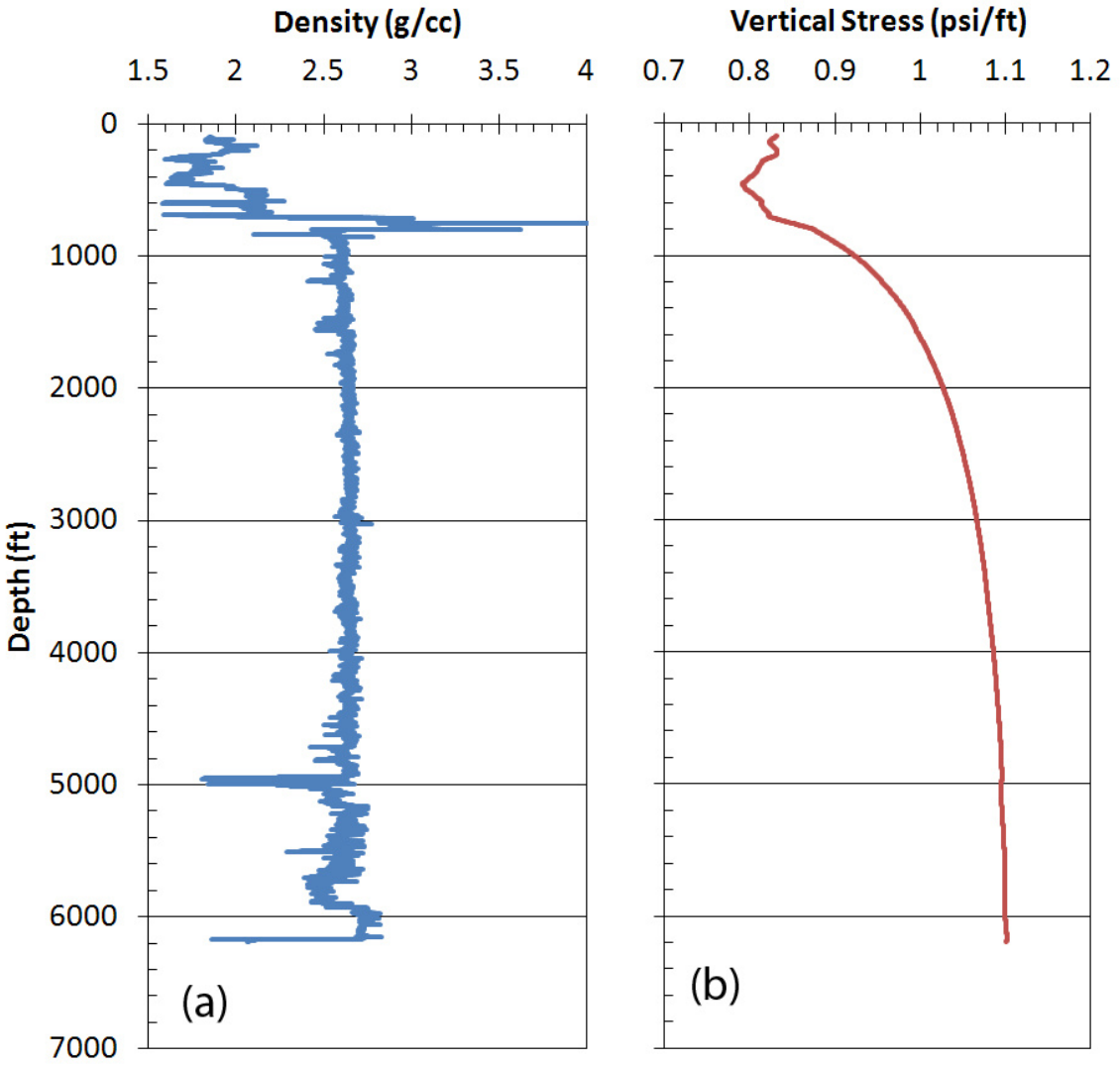

Figure 3.6: (a) Density log from the Well C vertical pilot. (b) Calculated vertical stress magnitude.

3.5.4 Image Logs and Horizontal Stress Orientation

An FMI log was taken in the Well C vertical pilot section and the Well C horizontal section. For stress modeling, the primary observables in an image log are wellbore failures caused by concentrations of compressive or tensile stresses at the walls

of the open borehole. Borehole breakouts are compressive failures on the walls of the borehole that occur when the maximum resolved compression exceeds the rock failure strength. Drilling induced tensile fractures are tensile failures on the wellbore wall that occur when the minimum resolved effective stress becomes negative and the wall fails in tension. The effective stresses at the well face of a vertical wellbore in a linear isotropic elastic medium are described by the Kirsch equations:

$$\sigma_{\theta\theta} = S_{Hmax} + S_{hmin} - 2\left(S_{Hmax} - S_{hmin}\right)\cos 2\theta - 2P_p - \Delta P - \sigma^{\Delta T} \tag{3.2}$$

$$\sigma_{rr} = \Delta P \tag{3.3}$$

$$\sigma_{zz} = S_V - 2\nu\left(S_{Hmax} - S_{hmin}\right)\cos 2\theta - P_p - \sigma^{\Delta T} \tag{3.4}$$

where ΔP is the difference between the pore pressure and the mudweight, $\sigma^{\Delta T}$ is the thermal stress from the temperature contrast between the reservoir and the drilling fluids, and $\theta = 0$ is the direction of S_{Hmax} (Zoback et al., 2003).

For a vertical well in an area where S_V is a principle stress, the maximum compression on the wellbore wall occurs in the direction of S_{hmin} and the maximum tension occurs in the direction of S_{Hmax}. When the principal effective stresses at the wellbore wall exceed the compressive strength of the rock, borehole breakouts will form in the direction of S_{hmin}. When the principal effective stresses at the wellbore wall are lower than the tensile strength of the rock, tensile fractures will form in the direction of S_{Hmax}. Using the Kirsch equations and the occurrence (or lack of occurrence) of compressive and tensile wellbore failures, it is possible to determine the orientations of the principal stresses and to constrain their magnitudes.

We analyzed the FMI image logs for both the vertical and horizontal sections of Well C, mapping natural fractures and recording any wellbore failures. Both the vertical and horizontal sections were free of borehole breakouts, indicating that compressive stresses on the wellbore wall never reached the failure strength of the rock. The Well C vertical pilot section was generally free of tensile failures, except for a few regions within the Barnett, as seen in Figure 3.7. Occurring on opposite sides of the well, these failures

indicate that the azimuth of horizontal stress is approximately 45°. This direction is consistent with the general trends of microseismicity mapped in the 51 hydraulic fracture stages (Figure 4.5). The limited occurrence of drilling induced tensile fractures indicates that tensile failure is close to occurring in this section but that the stresses are not such that tensile failure is widespread or extensive.

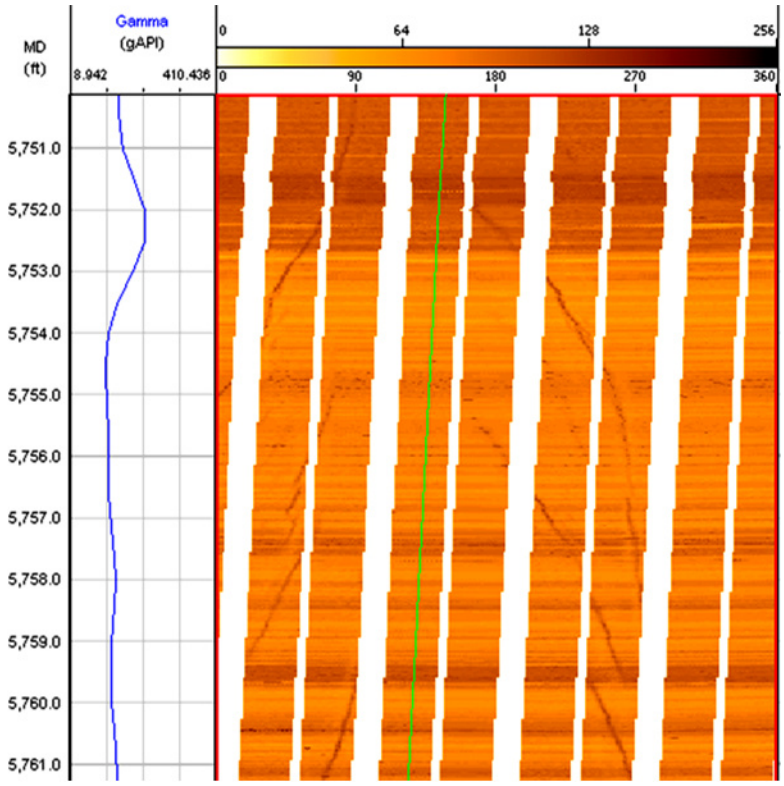

Figure 3.7: Well C vertical pilot FMI. Tensile fractures at opposite sides of the well indicating S_{Hmax} direction of N45E.

The Well C horizontal section exhibited extensive drilling induced tensile fractures on the top and bottom sides of the well, consistent with S_V being the maximum principal stress and the stress state being normal faulting. These tensile failures were a mixture of axial, transverse, and curved en echelon fracture sets, indicating variation in the magnitude and direction of the horizontal stresses along the length of the well. A summary of these failures and their variation is shown in Figure 3.8. This type of tensile failure has been reported before in Barnett shale horizontal wells, indicating that the stress state in our field area appears typical for the Barnett shale (Waters et al., 2006). Modeling of stress magnitudes and directions to fit these failures is discussed below.

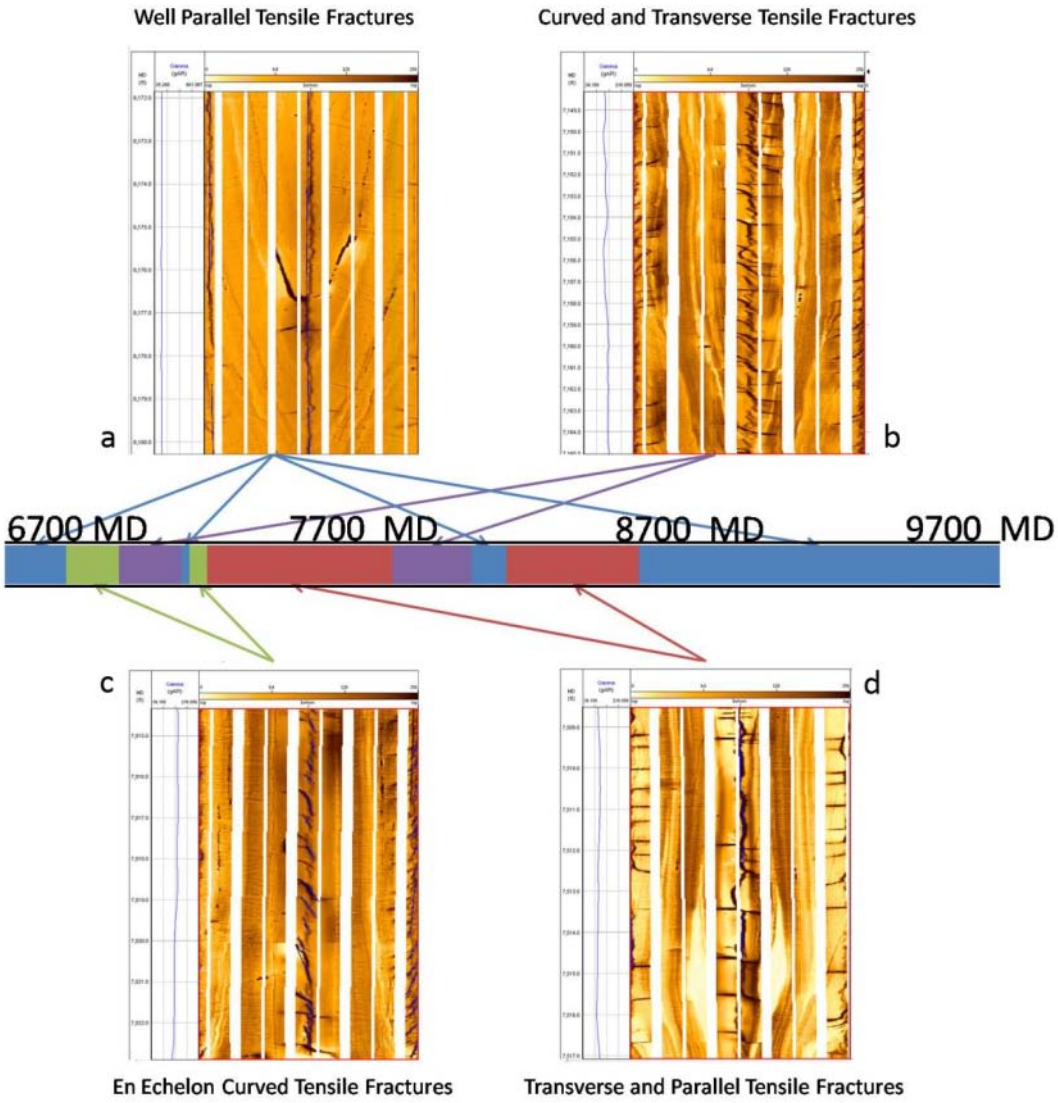

Figure 3.8: FMI image from the Well C horizontal section demonstrating multiple modes of tensile failure.

3.5.5 Constraining Horizontal Stress Magnitudes

Given that faults, fractures, and planar weaknesses are widely distributed in nearly all crustal volumes of reasonable size, including the Barnett shale, if the differences in the stresses in a location get too large, slip on faults will occur and the difference in stresses will be relaxed. Thus, there is a maximum difference between the principal stresses beyond which the system will relax back to equilibrium through shear failure events. The limiting ratio of maximum principal effective stress $\left(\sigma_1 = S_1 - P_p\right)$ to

minimum principal effective stress $\left(\sigma_3 = S_3 - P_p\right)$ is as follows:

$$\sigma_1/\sigma_3 = \left(\sqrt{\mu^2+1}+\mu\right)^2 \tag{3.5}$$

where μ is the coefficient of sliding friction (Jaeger, 1979).

While no leak off tests or mini-fracs were conducted during the Barnett shale project we are analyzing, we can use the hydraulic fracturing data to put upper bounds on S_{hmin} through analysis of the instantaneous shut-in pressure (ISIP) at the end of a fracturing stage. ISIPs are discussed in significantly more detail in Chapter 5 in the context of measuring stress changes from the hydraulic fracturing process itself. Since the pumping rates in the wells were so high (much higher than what is typically used for a leak off test or mini-frac), friction effects will elevate the pumping pressures, leading to possible overestimation of the S_{hmin} magnitude. In addition, the shut-in of each fracturing stage occurred after ~325,000 gallons of water and ~400,000 pounds of sand were pumped into the well, altering the stress state from the initial, pre-drilling stress state. Nevertheless, we can estimate S_{hmin} by measuring the ISIPs from Stage 1 of each of the five wells. The ISIP measurement for Well C Stage 1 is shown in Figure 3.9. For Stage 1 of Wells A-E, the ISIPs ranged from 3600 to 3900 psi, or 0.63 to 0.68 psi/ft at reservoir depth. Thus, a reasonable upper bound for the S_{hmin} magnitude is 0.68 psi/ft.

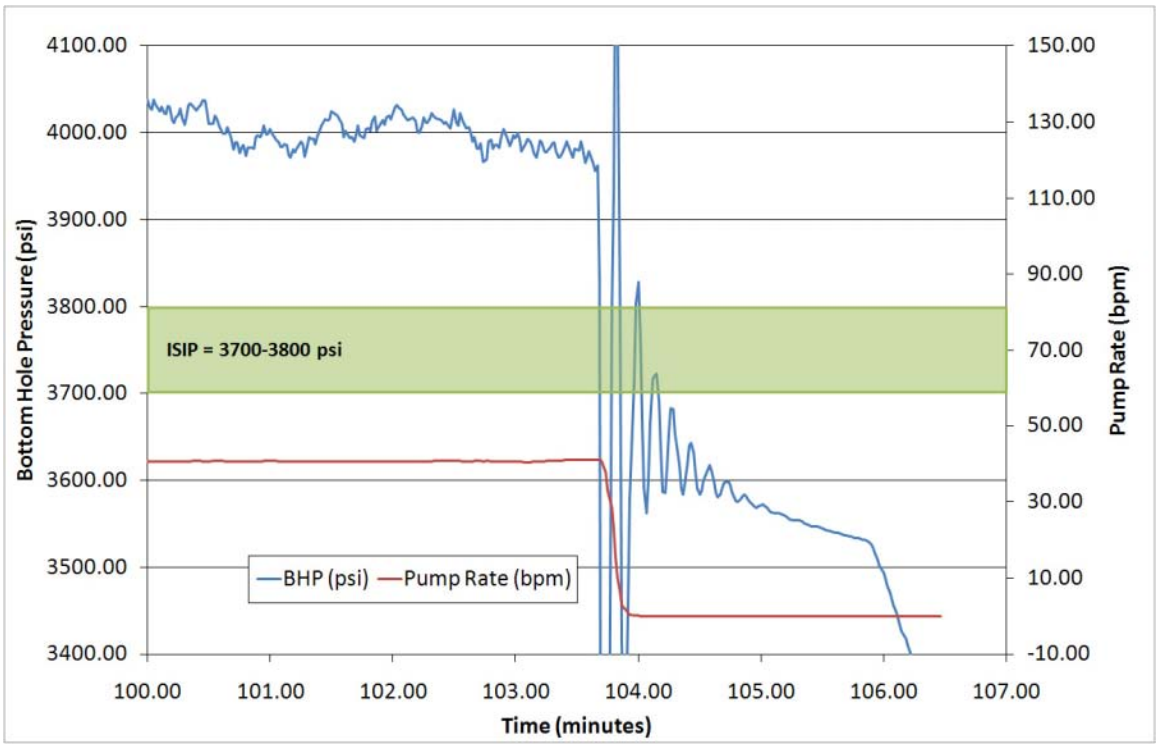

Figure 3.9: Example ISIP curve from Well C, Stage 1. A water hammer effect at the end of pumping causes the ISIP estimation precision to be ± ~50 psi.

In a normal faulting environment, as is typical for the Barnett shale, $S_V > S_{Hmax} > S_{hmin}$. Therefore, for our field area, $\sigma_1 = S_V - P_p$ and $\sigma_3 = S_{hmin} - P_p$. By directly measuring S_V through density integration, we can always put a lower bound on S_{hmin}. To get the magnitude of S_{Hmax}, we model the failures in both the vertical and horizontal image logs to constrain the possible magnitudes within reasonable bounds.

Figure 3.10 shows the stress bounds for the Well C vertical pilot, as analyzed with the program SFIB from Geomechanics International (GMI, 2010). To create this plot, called a "stress polygon", the first step is to determine the limiting stress ratios at which the rock will undergo shear failure. These limits provide the outer bounds of the feasible stress space, which in Figure 3.10 are the black lines enclosing the stress space. The next step is to use all other observations to constrain the horizontal and vertical stress magnitudes within that space. If drilling induced tensile fractures were found in the well, the rock must go into tension at some point around the well for the given stress condition. The blue line marked "0" in Figure 3.10 represents stress conditions where the minimum stress concentration in the wellbore is zero. To the outside of this line is where the

minimum stress concentration becomes negative and the wellbore wall goes into tension. Lastly, we look at the prevalence of borehole breakouts in the well. In our case, we observed no borehole breakouts, indicating that the maximum compressive stress along the well did not exceed the strength of the rock. If the rock has a strength of at least 20,000 psi, then we know that the stress state must be below the red line in Figure 3.10. If there were breakouts, the stress state would need to be outside that red line, indicating that compressive failure had occurred.

Since drilling-induced tensile fractures were only infrequently observed and breakouts were not observed at all in the Well C vertical pilot section, the stress state must lie inside the tensile failure line and below the compressive failure line. We also know that only a normal faulting stress environment is feasible based on the top and bottom position of the tensile fractures in the Well C horizontal section. Combining all these observations, the feasible stress state in the Well C vertical pilot section must lie closely to the inside of the tensile failure line, as is mapped in red in Figure 3.10. Figure 3.11 shows similar stress bounds calculated for the Well C horizontal section. Since tensile fractures were observed extensively but borehole breakouts were not, we can infer that the stress state needs to lie outside of the tensile failure line. The feasible stress state in the Well C horizontal section is mapped in red in Figure 3.11. Looking at only the overlap between the feasible stress zones determined in Figures 3.10 and 3.11 along with the S_{hmin} magnitude constraint from the ISIP analysis, we can constrain S_{hmin} to between 0.63 to 0.68 psi/ft and S_{Hmax} to below 0.88 psi/ft.

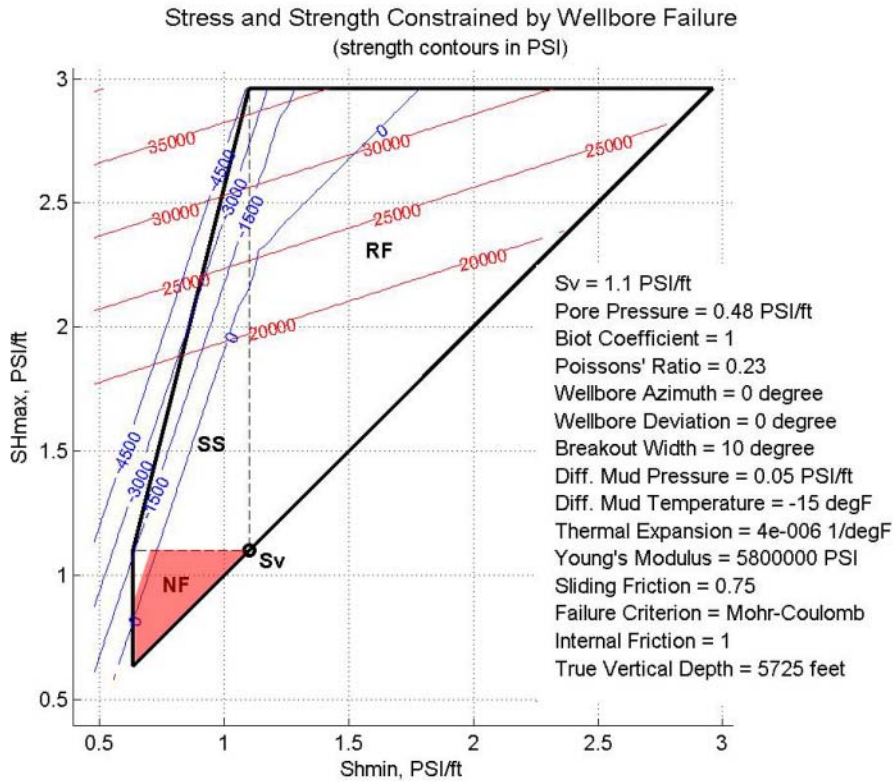

Figure 3.10: Constrained stress curve for the Well C vertical pilot, showing feasible stress state in red.

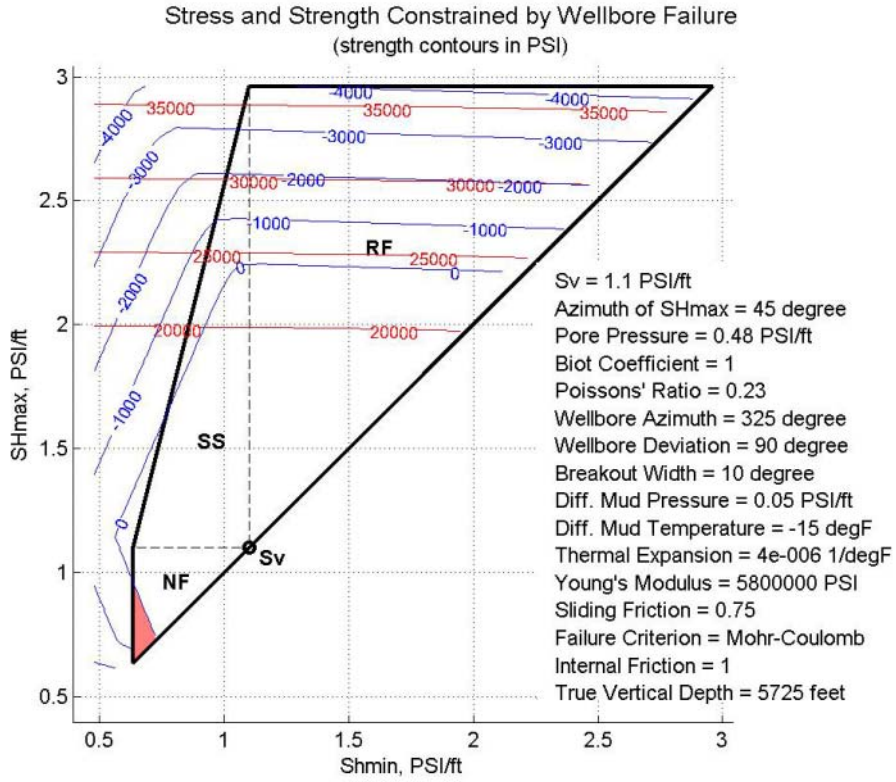

Figure 3.11: Constrained stress curve for the Well C horizontal section, showing feasible stress state in red.

The tensile failure line that is plotted in Figures 3.10 and 3.11 is based simply on the occurrence of any type of wellbore tensile failure, and includes no information on the orientation of the tensile failure. As seen in Figure 3.8, certain sections of the Well C horizontal had both axial and transverse tensile failure at the same time. To have axial failure $\sigma_{\theta\theta}$ must go into tension and to have transverse failure σ_{zz} must go into tension. Thus, we can further constrain the stress state by finding a condition where both types of tensile failure are predicted to occur. One possible stress state where both types of failure occur is seen in Figure 3.12a. Here $S_{Hmax} = 0.73$ psi/ft and $S_{hmin} = 0.65$ psi/ft. While this is only one possible stress state that satisfies the multiple modes of failure seen in Figure 3.9, it will be used as the base uniform stress state for the stress modeling in Chapter 5.

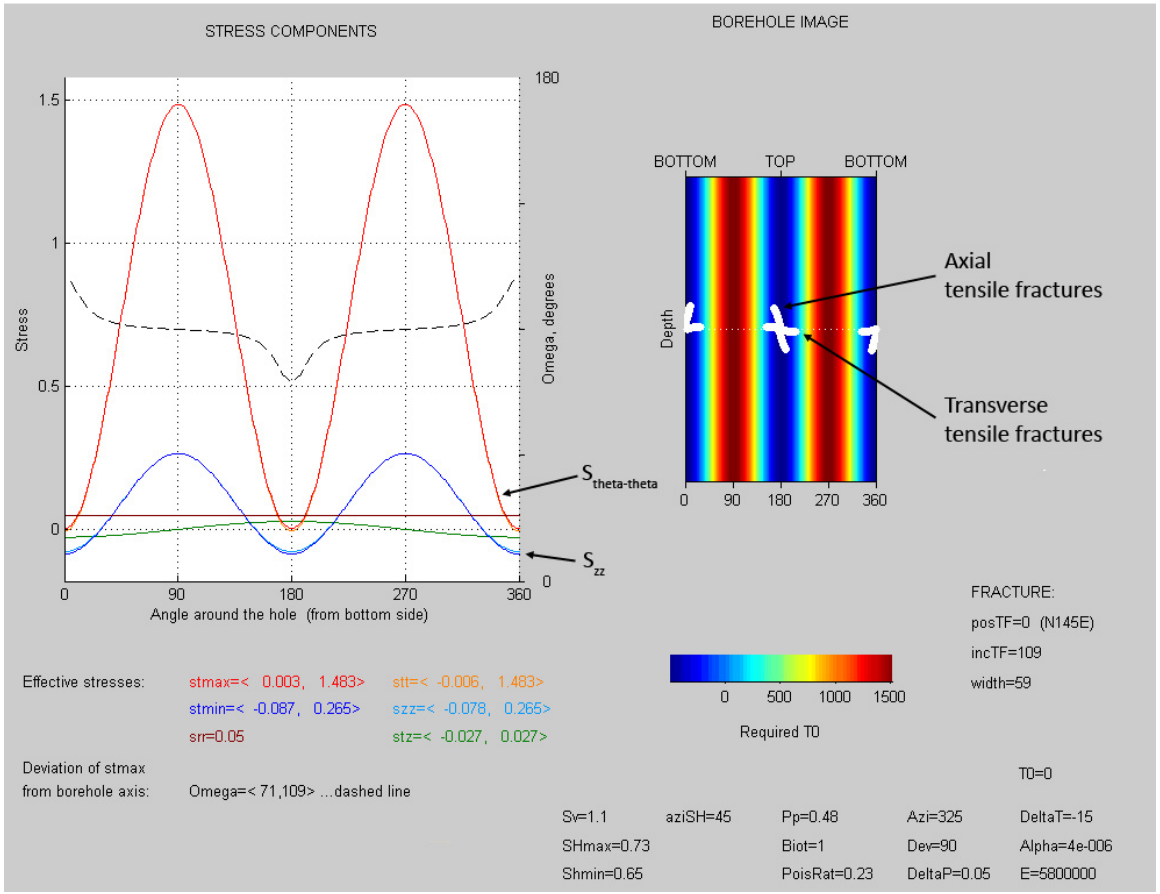

Figure 3.12a: BSFO plot for the Well C horizontal, indicating both axial and transverse tensile fracture formation at the given stress state. $\sigma_{\theta\theta}$ and σ_{zz} go into tension at the top and bottom of the well.

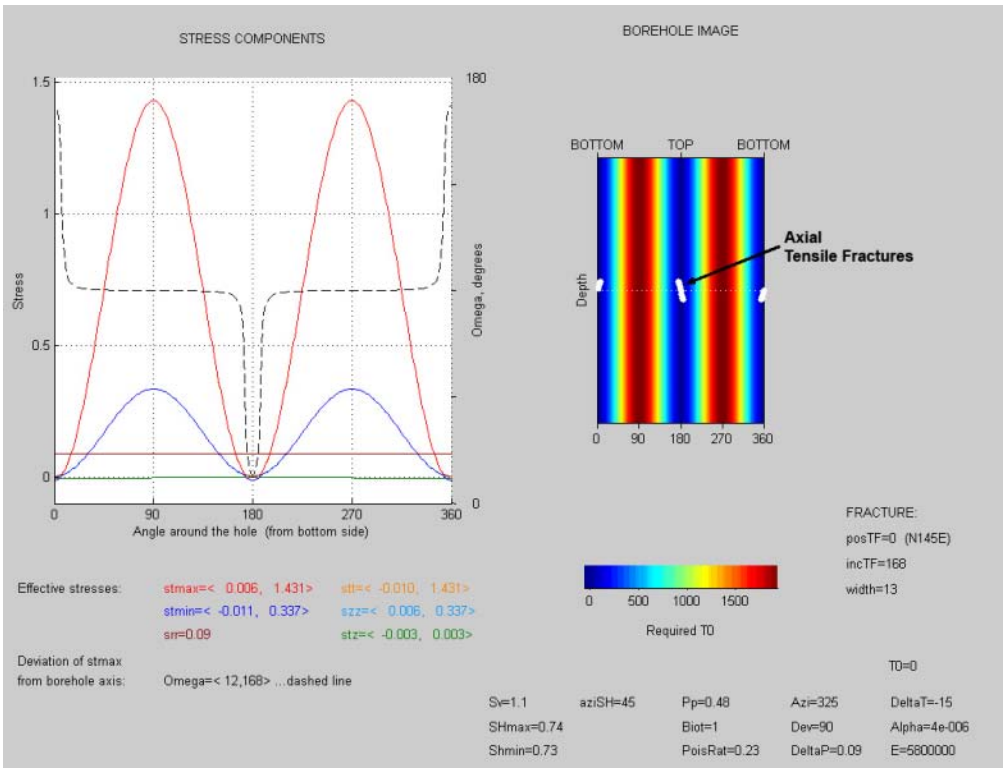

Figure 3.12b: BSFO plot for a stress state with more isotropic horizontal stresses and increased mud weight compared to the base case, indicating formation of curved axial tensile fractures only.

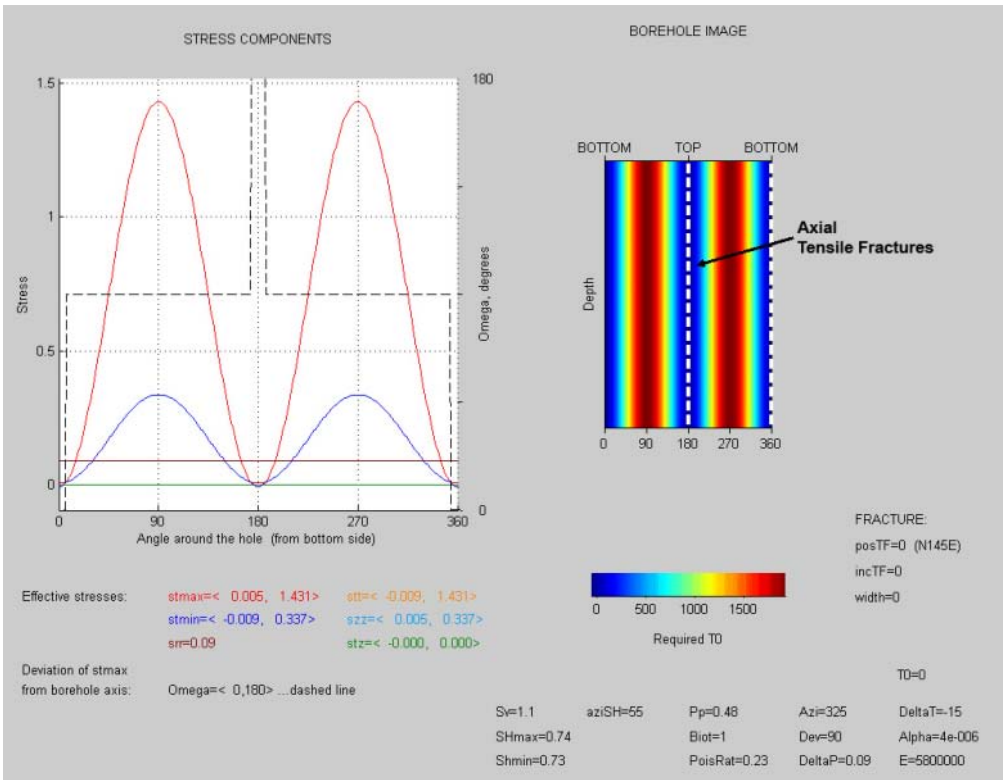

Figure 3.12c: BSFO plot for the same modified stress magnitudes as in Figure 3.12b with the stress direction rotated to be perpendicular to the well, indicating formation of well parallel axial tensile fractures.

We also perturbed our base stress state in an attempt to match the other modes of failure seen in Figure 3.8. To form axial tensile fractures only, the horizontal stress magnitudes would have to be more isotropic and elevated in magnitude to $S_{Hmax} = 0.74$ psi/ft and $S_{hmin} = 0.73$ psi/ft. By itself, this stress increase makes the well more stable and prevents either axial or transverse fractures from forming. However, by increasing the difference between the mud weight and the pore pressure (the ΔP term in Eq. (3.2)), $\sigma_{\theta\theta}$ becomes negative and axial tensile fractures form. σ_{zz}, however, is not directly affected by the difference between mud weight and pore pressure as Eq. (3.4) demonstrates. Thus, σ_{zz} does not go into tension and only axial tensile fractures form. This modified stress state is depicted in Figure 3.12b. If the horizontal stress direction rotates by 10° to the east, only well parallel tensile fractures will form, as seen in Figure 3.12c. With these slight perturbations, it is possible to match all the modes of failure seen in Figure 3.8 and thus constrain both the feasible range for the base stress state and quantify the variability in stress magnitude and direction along the length of the well.

3.5.6 Natural Fractures

We mapped over 200 natural fractures in the Well C horizontal. These fractures represent potential planes of weakness during hydraulic fracturing. Analyzing how stress is resolved on these fractures in the pre-fracturing stress state indicates whether they might slip as pore pressure is increased during hydraulic fracturing. Figure 3.13a shows a stress analysis of the Well C fractures under the pre-fracturing stress state assuming relatively weak sliding friction (μ=0.6) to provide a best case estimate of fractures near failure. The majority of fractures seem to be part of two steeply dipping conjugate fracture sets, perhaps created during a previous strike-slip stress oriented with a more easterly S_{Hmax} direction than in the current stress state. These fractures are striking E-W and NE-SW and thus have low resolved shear stress due to the current N45E S_{Hmax} stress direction and relatively low horizontal stress anisotropy. 11 fractures, however, are near failure. These fractures are oriented in the two conjugate directions expected for normal faulting slip in the modeled stress state. These fractures, and others within the reservoir of similar orientations, would likely slip under very modest pore pressure perturbations.

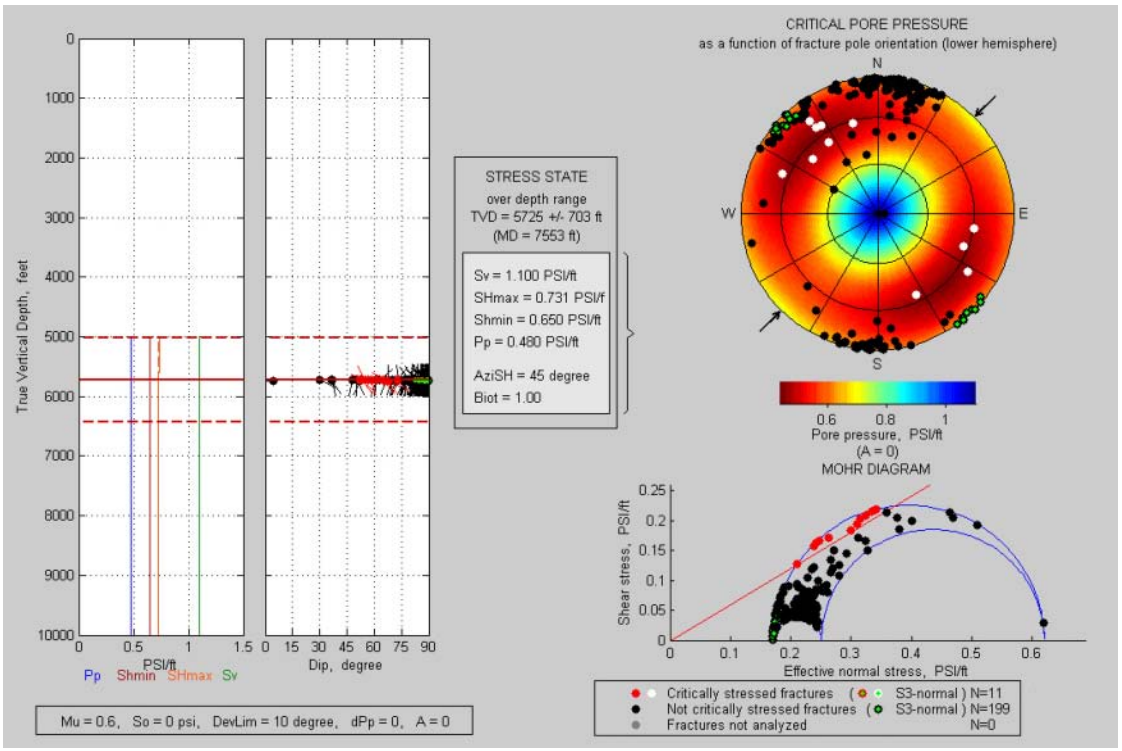

Figure 3.13a: Analysis of resolved stress on Well C fractures under the pre-fracturing stress state, indicating that 11 fractures (in white) are near failure. Colors within the stereonet at top right indicate the critical pore pressure perturbation necessary to induce slip on the specified faults.

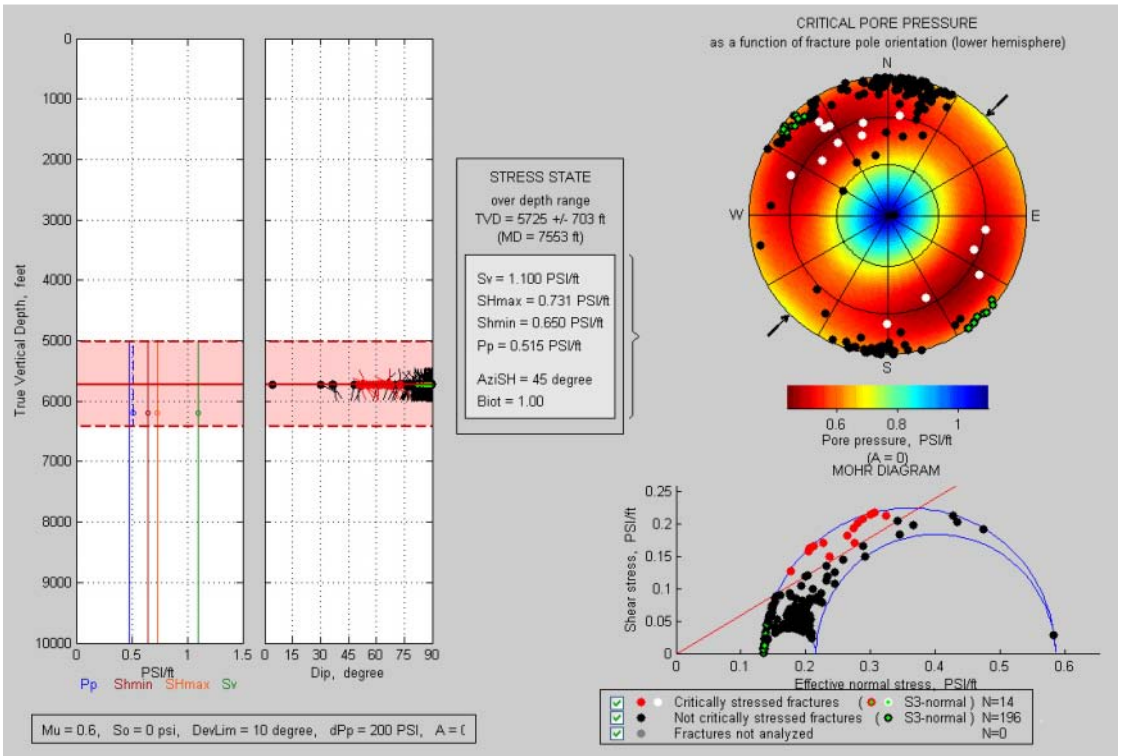

Figure 3.13b: Analysis of resolved stress on Well C fractures under the perturbed stress state where the pore pressure has increased by 200 psi at the well depth. Under this perturbed state, 14 fractures are likely to slip, which is only a small increase from the base state.

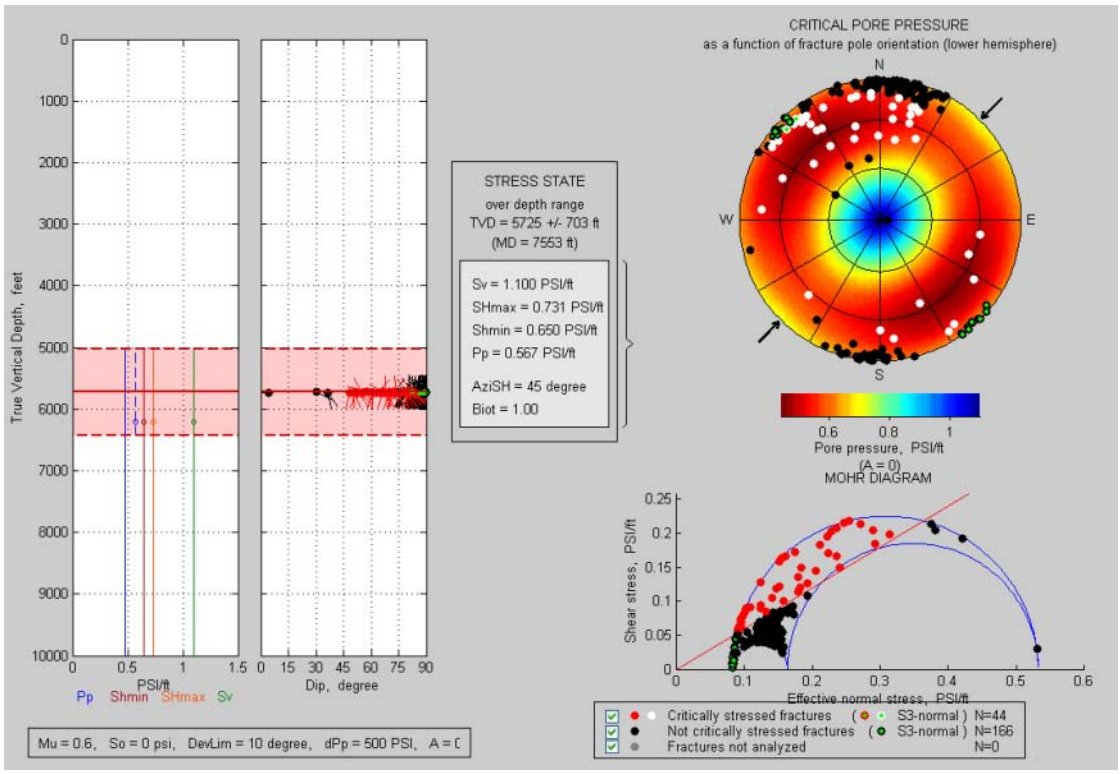

Figure 3.13c: Analysis of resolved stress on Well C fractures under the perturbed stress state where the pore pressure has increased by 500 psi at the well depth. Under this perturbed state, 44 fractures are likely to slip, which is over 20% of the fractures mapped in the Well C horizontal.

The remaining fractures may also slip if the pore pressures during stimulation increase by a large enough amount. Figures 3.13b and 3.13c show stress analyses of the Well C fractures if the pore pressure in the reservoir were to increase by 200 psi and 500 respectively. Under the 200 psi perturbed state, only 3 more fractures are expected to fail. This indicates that most of the natural fractures are quite stable in the pre-existing stress state. Under the 400 psi perturbed stress state, 44 fractures are likely to fail, a four-fold increase over the pre-fracturing stress state. Many of these fractures are steeply-dipping, and thus under regular conditions would never slip due to their low shear to normal stress ratio. If pore pressures in the reservoir can increase significantly during hydraulic fracturing, effective normal stress on these fractures will decrease, triggering slip and thus stimulation of the reservoir. Chapter 5 will provide estimates on the kinds of pore pressure perturbations likely to be found during a typical hydraulic fracturing project.

3.6 Conclusions

We integrated geological, geophysical, and geomechanical data from our Barnett shale study area in order to analyze the stress state in the reservoir before hydraulic fracturing occurred. Using the image logs from the Well C vertical pilot and the Well C horizontal section, we mapped natural fractures and wellbore failures. While there was some variation in the stress state along the length of the well, we determined a best-fit stress state of $P_P = 0.48$ psi/ft, $S_V = 1.1$ psi/ft, $S_{Hmax} = 0.73$ psi/ft, and $S_{hmin} = 0.65$ psi/ft. The other modes of stress seen in the well can be matched by making the horizontal stress magnitudes more isotropic, increasing the mud weight, and rotating the stress direction up to 10°.

Applying the base stress state to the mapped natural fractures indicates that there is significant potential for induced shear slip on natural fracture planes in this region of the Barnett, particularly close to the main fracture plane where the pore pressure increase during hydraulic fracturing is likely to be very high. The geological, geophysical, and geomechanical analyses presented in this chapter provide input parameters to the modeling and analysis conducted in Chapters 4 and 5, as well as general context for our studies of this region of the Barnett shale.

Chapter 4

MEASURING HYDRAULIC FRACTURING SUCCESS WITH MICROSEISMIC MAGNITUDE SCALING ANALYSIS

Abstract

We developed new techniques to quantify the robustness of hydraulic fracturing in gas shale reservoirs. The case study we analyzed involves five parallel horizontal wells in the Barnett shale with 51 frac stages. To investigate the numbers, sizes and types of microearthquakes initiated during each frac stage, we created Gutenberg-Richter-type magnitude distribution plots to see if the size of events follows the characteristic scaling relationship found in natural earthquakes. We found that slickwater fracturing does generate a log-linear distribution of microearthquakes, but that it creates proportionally more small events than natural earthquake sources. Finding considerable variability in the generation of microearthquakes, we used the magnitude analysis as a proxy for the "robustness" of the stimulation of a given stage. We found that the conventionally fractured well and the two alternately fractured wells ("zipperfracs") were more effective than the simultaneously fractured wells ("simulfracs") in generating microearthquakes. We also found that the later stages of fracturing a given well were more successful in generating microearthquakes than the early stages, a phenomenon which is investigated further in Chapter 5.

4.1 Introduction

In this chapter, we introduce a method to quantify the robustness of hydraulic fracture stimulation in a reservoir using the magnitude distribution of the microearthquake events generated by the hydraulic fracturing. Compared to other seismological analyses of hydraulic fracturing microseismicity, the method we develop is less sensitive to sensor distance effects and the random variation in the number of largest events. We believe this method will complement more common analyses that use either

the pressure and rate history of the fracturing job or the total fractured volume as measured from the microseismic events. Incorporating unbiased information on the distribution of event magnitudes will lead to a fuller picture of the results of a hydraulic fracturing experiment.

In the sections below, we first describe the history and evolution of hydraulic fracturing and microseismic monitoring in the Barnett Shale, and then provide background on the evidence for a consistent scaling relationship of earthquake event size down to very small magnitudes. After describing the microseismic dataset from the Barnett shale study area we investigated, we detail the methodology we used to quantify hydraulic fracturing robustness and then present an analysis from this study area using our metric. The causes of variations in fracturing robustness seen in our study area are discussed briefly and then more fully analyzed in Chapter 5.

4.1.1 Hydraulic Fracturing in the Barnett Shale

As described in Chapter 1, the development of the Barnett shale as a successful producer of natural gas was a trial and error process. This experimentation eventually led to the successful introduction of horizontal drilling and multi-stage slick-water hydraulic fracturing. Since the permeability of intact Barnett rock matrix is ultra-low and there are limited permeable natural fractures, the stimulation needs to affect a large volume of the reservoir, essentially creating a fully artificial fractured reservoir. To generate this wide fracture area, low viscosity slick-water fluid is used during injection, which encourages leak-off into the reservoir. As pore pressure in the surrounding rock increases, shear slip occurs on planes of weakness that are well-oriented in the given stress state. These shear failures (microearthquakes) create permeable pathways in the intact reservoir rock, linking back to the main tensile hydraulic fracture and the well (Cipolla et al., 2008; Palisch et al., 2008). Even with microseismic stimulation, the total drainage area is still relatively small for a single fracturing stage. Thus, most wells in the Barnett are now drilled horizontally with multi-stage fracturing. The spacing between adjacent wells has also decreased. While these techniques have become the methods of choice in the Barnett, not all gas shale reservoirs respond in the same way (Matthews et al., 2007). In particular, the Barnett has a high silica content, which many have argued makes the rock

more “brittle” than typical clay-rich shales, thus allowing for greater fracture surface area creation during stimulation (Grieser and Bray, 2007).

4.1.2 Analyzing Hydraulic Fracturing Stimulation

The ultimate determinant of the success of hydraulic fracturing is the economic production of natural gas enhanced by the fracturing process. However, the achievement of production goals may not be evident until weeks, months, or even years after stimulation occurs. Factors that can prevent rapid determination of production success include delay in connecting a well to existing production infrastructure, the time needed for flowing gas to displace the injected fracturing fluids in the reservoir, and the difficulty in determining the decline rate of a specific well during its first few months. Thus, several techniques have been developed to help predict the success of fracturing either soon after the operation concludes or even during the hydraulic fracturing job itself, thus allowing for modifications of the procedure in real-time.

The simplest technique is to analyze the bottom hole pressure and flow rate of the fluid that is pumped into the reservoir during fracturing. This information can be used to estimate the growth and extent of the created hydraulic fracture and many other important fracturing parameters (Economides and Nolte, 2000). However, the trends seen in the pumping pressure can have non-unique causes. The assumptions also tend to break down when there is no longer a single, planar, symmetric hydraulic fracture. It is challenging, therefore, to quantify the complexity of a network of tensile fractures and pressure-induced shear failures using just the pumping rate and pressure history.

Microseismic monitoring methods to directly image the fracturing process were developed to address the difficulty of interpreting fracture creation based solely on the pumping and treatment information. These techniques are presented in more detail below, but the typical outputs of microseismic monitoring are the x-y-z locations, location uncertainties, origin times, and magnitudes of detected events. Various techniques have been used to interpret this seismological information into information on the fracture network created during the stimulation process. Warpinski (2009) and Mayerhofer et al. (2010) reviewed many of the techniques used to interpret the microseismic data generated during hydraulic fracture monitoring.

The most common application of microseismic monitoring is to simply map the approximate dimensions of the stimulated region and the major fracture pathways through the stimulated volume. However, the residual error in the location of a single event is often on the order of tens to a hundred or more feet (Maxwell, 2009; Kidney et al., 2010), which in many cases approaches the lateral or vertical dimensions of the reservoir into which the fluid is being injected. The residual errors in best-fit locations combined with systematic errors from the estimate of the velocity structure make the precise mapping of the induced fracture network highly uncertain. In particular, attempts to quantify the surface area of the induced fracture network by linking events seemingly related in time and space will likely greatly underestimate the total surface area created in the reservoir. Mapping fracture planes using the focal mechanisms of detected events has been more successful (Williams-Stroud, 2008; Baig and Urbancic, 2010; Eisner et al., 2010), but this technique may unfortunately remain of limited application due to the need for multiple seismometer arrays to generate the focal mechanism solutions.

A better metric for quantitative comparison may be the total volume in which microearthquakes have occurred, a value commonly called stimulated reservoir volume (SRV). Calculating the SRV usually involves the mapping of bounding volumes around the detected events and then the summation of those volumes to determine the total SRV in a given reservoir. While affected by the uncertainty in microearthquake locations, the measurement of the total stimulated volume eliminates the bias of trying to pick fracture pathways and can allow for comparison between different stimulation projects. Case studies of SRV analysis in Mayerhofer et al. (2010) showed that SRV often correlates with production data on both a cumulative 6-month and 3-year basis.

Despite this apparently successful correlation, there are challenges to using SRV as the primary metric for hydraulic fracturing analysis. Firstly, SRV analysis ignores both the size and the density of the fractures created within the stimulated volume. The size and the density of fractures are likely the key factors controlling access to the low permeability gas shale matrix within the overall stimulated volume. Secondly, SRV analysis in practice often assumes symmetric distribution of events in regions beyond the detection limit of the seismic array, when in fact it is precisely the asymmetric distribution of the fractured volume that we are interested in observing. In addition, when

computing the SRV from multi-stage hydraulic fracturing in closely-spaced parallel wells, there is a risk of double-counting total "stimulated volume" if overlapping regions of events from separate wells or stages provide less net enhanced production than identically sized, non-overlapping regions. Lastly, the uncertainty in event locations leads to overestimates of the SRV when using a single string of seismometers. The outermost events by definition provide the boundaries of the stimulated volume, yet they have the largest uncertainties in their location due to their distance from the sensor array. Thus, total measured SRV is dependent on the details of acquisition geometry and processing methods, creating challenges when comparing different projects based on SRV.

Both SRV analysis and fracture mapping utilize only the locations of the mapped events, ignoring additional information available in the seismic signal. Urbancic and Maxwell (2002) looked at the apparent stress drop of events to differentiate between shear and non-shear components of deformation, which they suggest could allow for mapping of the most permeable pathways in the reservoir. Trying to incorporate fracture density into SRV analysis, Maxwell et al. (2006) combined total seismic moment with SRV to generate a combined stimulation metric in a Barnett Shale well. This combined metric was found to correlate with production in cases where production does not correlate with SRV alone. They also mapped the moment density of events from the stimulation to try to image the regions where the largest deformation occurred. Due to the ~32x difference in moment between events just one magnitude value apart (Hanks and Kanamori, 1979), the total measured moment as well as the moment density maps were dominated by the few largest events. Thus, it would be difficult to extend their analysis due to the high dependence of total moment on the random occurrence of the few largest events. Maxwell et al. (2008) looked at the rate of moment generated during hydraulic fracturing. This rate analysis is useful in seeing if a fracturing job has stalled in generating new fractures, allowing for on-the-fly changes in the stimulation method. However, they found that total moment correlates poorly with total injection volume, again likely due to the few largest events dominating the total moment.

4.1.3 Microearthquake Magnitude Scaling

Urbancic et al. (1999) suggested using the relative frequencies of microearthquake event magnitudes to determine the evolution and behavior of hydraulic fracturing. This method can provide an estimate of fracturing activity level that is independent of both sensor bias and the random occurrence of the largest few events. In sections 4.2, 4.3, and 4.4 of this chapter, we expand upon the technique introduced by Urbancic et al. (1999) and apply it to a case study in the Barnett Shale. Before detailing the methodology we used, we first discuss the theory and evidence for consistent earthquake magnitude scaling relationships and how it has previously been applied to microearthquake data and fracture generation in a reservoir.

Gutenberg and Richter (1944) provided evidence for a consistent scaling relationship in earthquake magnitudes. In their compilation of earthquake data from California and the world, they found that the total number of earthquakes at a given magnitude obeyed a log-linear relationship, with the logarithm of total earthquakes at a given magnitude decreasing with a slope of about 1 for each increase in magnitude unit. This slope has become known as the b-value, and has been found to be about 1 for nearly all crustal volumes containing naturally occurring earthquakes. The consistency of this earthquake scaling relationship has been extensively studied over the past six decades, both as an important parameter in estimating earthquake recurrence and as an insight into the fundamental processes of earthquake generation and fault evolution (Main, 1996).

While the consistent slope of the magnitude-frequency relationship for relatively large earthquakes has been well established, the extension of this relation down to smaller earthquakes has been subject to considerable debate. Aki (1987) found that the magnitude-frequency relation for events of $M < 3$ was not followed, leading to far fewer small events than would be predicted if self-similarity continued. Trifu et al. (1993) found departures from a constant b-value of about 1 for events between M -0.5 and M 0 from a dataset recorded in a mine. In contrast, several authors have found b-values of about 1 for events down to M -1, and even down to M -3, in careful studies from seismic networks installed in mines, boreholes, and at the surface (Sprenke et al., 1991; Abercrombie, 1996; von Seggern et al., 2003; Oye et al., 2005; Boettcher et al., 2009).

Despite the ongoing debate over the causes (and the consistency) of the earthquake magnitude-frequency relationship for small events, it is still possible to analyze the microearthquakes generated by hydraulic fracturing using the same methodologies of the studies above. Urbancic et al. (1999) analyzed the magnitude-frequency relationship from a single-well, multi-stage hydraulic fracturing microseismic dataset. They found that the scaling of events was log-linear within the range of event magnitudes that were fully detected by the seismic array. They then calculated both the b-value and the "activity level" of the generated events across space and time in the reservoir. The b-value was used to investigate the ratio of large and small events and the failure mechanisms that generated those events. The activity level was then used to quantify the rate of seismicity and thus the density of fractures created in the reservoir.

We developed a frequency-magnitude analysis method that is similar to Urbancic et al. (1999), but more appropriate for comparison of the individual stages and individual wells of complex hydraulic fracturing experiments. We present our methodology in detail below and then apply it to a case study in the Barnett shale.

4.2 Methodology

4.2.1 Magnitude Scaling in a Reservoir

As discussed above, we measure microseismic magnitude scaling to create a stimulation success metric that can compare the success of different fracture operations yet is fully independent of the seismic acquisition geometry. This technique is based on fitting a log-linear scaling relationship to the microseismic magnitude data:

$$\log_{10}(N \geq M) = a\text{-}bM \tag{4.1}$$

Fitting the event magnitudes to this equation determines the b-value, which is the slope of the log-linear curve, and the a-value, which is the log of the total number of events ≥M=0. For areas with identical b-value scaling parameters, this intercept is a robust measure of the relative activity level for the two areas. For example, when fitting a decade of seismicity from New England and a decade of seismicity from a New England-sized portion of California, the two curves will likely have a very similar b-value. However, the California curve will have a much greater a-value than the New England

curve. The a-value, therefore, is an indication of the relative seismicity levels in these two areas.

This principle also allows us to analyze differences in activity level for microseismicity found in a reservoir, acknowledging the fact that the detection of the very smallest events will be affected by the distance between the events and the monitoring arrays. For example, Figure 4.1 schematically demonstrates what the magnitude scaling curves might look like for a hydraulic fracturing stage measured by two different seismic arrays, one close to the fractures and one farther away. The closer array detects many more total events, but the scaling curves are identical above the magnitude threshold of the more distant array. Thus, fitting equation (4.1) to only the log-linear portion of the scaling curve can isolate sensor effects quite easily. In the case of multiple hydraulic fracturing stages, it is thus possible to determine the robustness of fracture creation independent of array location. For example, Figure 4.2 shows two fracture stages detected by a single seismic array. More total events are detected for the stage closest to the array. However, the farther stage is in fact more robust overall, and this difference in activity level is picked up by fitting the log-linear portions of the magnitude scaling curve.

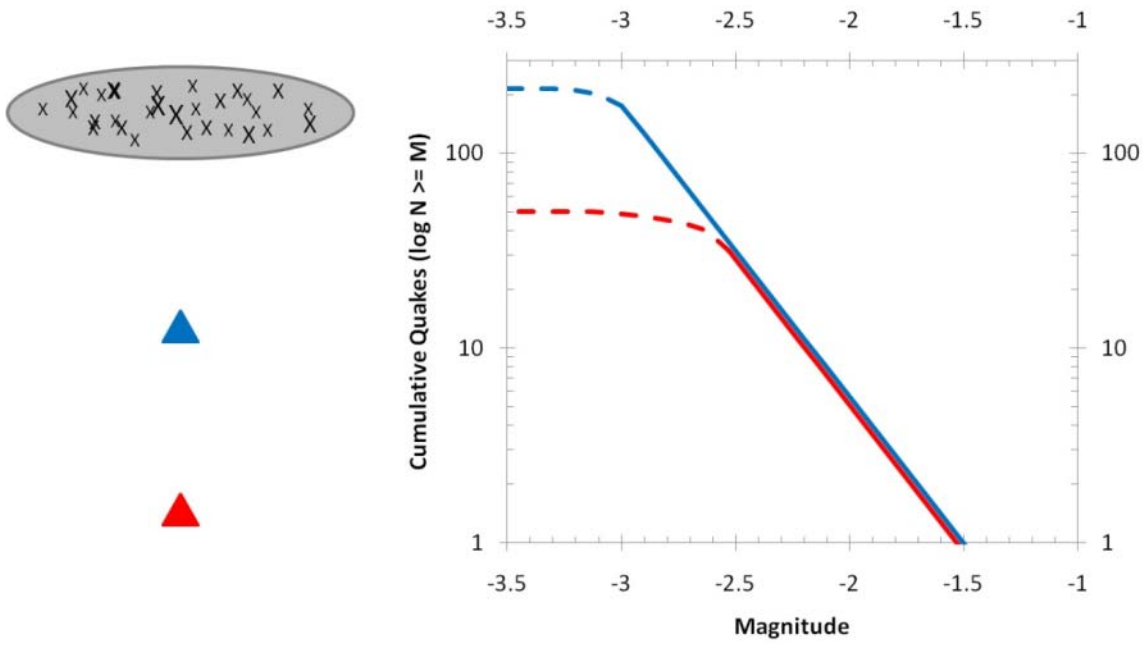

Figure 4.1: Schematic magnitude scaling curves for a hydraulic fracturing stage as measured by two different seismic arrays, one close to the fractures (blue) and one farther away (red).

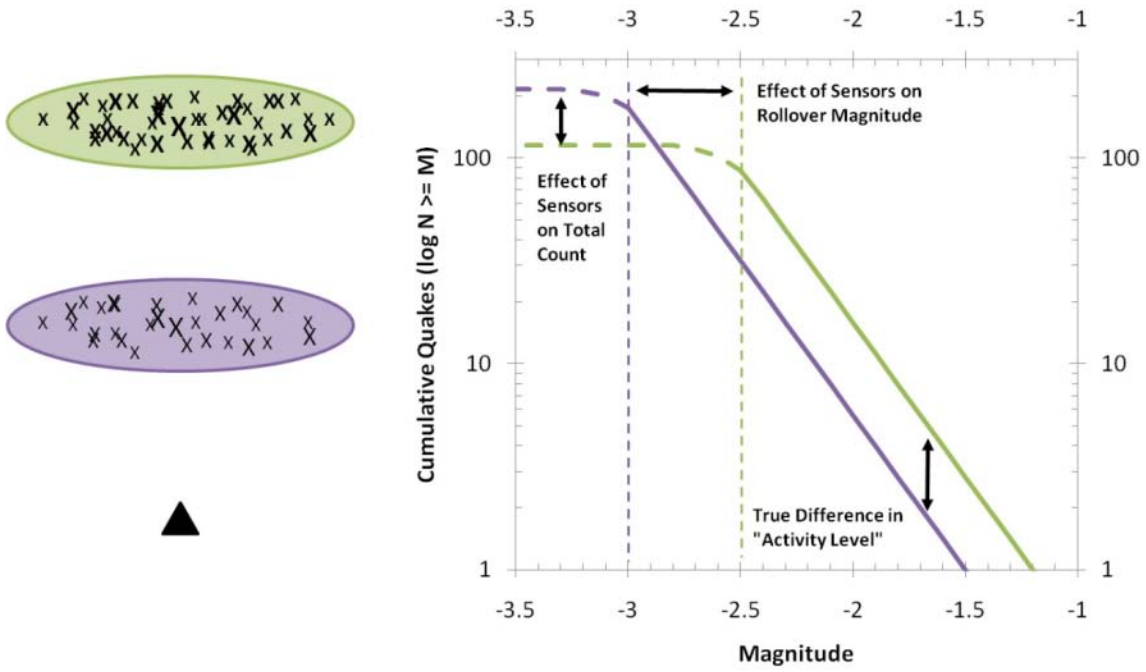

Figure 4.2: Magnitude scaling curves for two fracture stages detected by a single seismic array. More total events are detected for the stage closest to the array (purple), but the stage farther away (green) is in fact more robust.

4.2.2 Quantifying Microseismic "Activity Level"

To quantify the effects discussed above, we must first determine the magnitude threshold below which events are no longer reliably detected by the seismometer array and then calculate the a-value and b-value for the population of events above that threshold. While there is a robust literature on rigorously quantifying a-value and b-value for seismological uses (Aki, 1965; Guttorp, 1987; Wiemer, 2001; Lombardi, 2003; Marzocchi and Sandri, 2003; Felzer, 2006), we use a simple least-squares technique to quickly estimate the a-value and b-value. We include only the events above magnitude M that give the best linear fit to $\log_{10}(\mathrm{N} \geq \mathrm{M}) = a\text{-}b\mathrm{M}$.

The b-value can provide important information on the distribution of triggered events as well as insight into the mechanisms of fracture creation in the reservoir. However, the a-value is in fact a more direct measure of the success of hydraulic fracturing since it is equal to the actual number of earthquakes predicted to be $\geq$ M = 0. For two populations with the same b-value, the traditional a-value uniquely describes the difference in activity between the populations at all magnitudes. However, for

populations with different b-values, the actual quantity of events within the magnitude range of interest could differ much more than is expected from a small difference in a-values. Thus, the typical a-value from Gutenberg-Richter type analysis cannot be used as a comparative metric for populations with varying b-values.

To better measure the activity level for hydraulic fracturing, we calculate the cumulative number of events greater than or equal to the magnitude that is the detection threshold for the stage with the worst detection sensitivity. This metric is similar to Urbancic et al. (1999), but uses an empirical detection threshold that ensures that each stage can be quantitatively compared against any other stage on the same terms.

4.3 Microseismic Dataset

The microseismic dataset we analyzed for frequency-magnitude scaling is from a slick-water hydraulic fracturing experiment in the Barnett Shale. This experiment was designed to study three different hydraulic fracturing techniques through analysis of a comprehensive logging and monitoring program. A geological, geophysical, and geomechanical overview of the study area and wells was presented in Chapter 3. Next, we will describe the hydraulic fracturing program, the microseismic monitoring program, and the microseismic location and magnitude results for the experiment.

4.3.1 Hydraulic Fracturing Program

The five wells in the study area (Wells A-E) were drilled, cased, and cemented before being perforated and then fractured in stages along their horizontal sections. For each well, the staged fracturing began at the toe of the well and proceeded back up the measured depth to the heel of the well. The stages were isolated at the end using ceramic plugs and at the start using an inflatable packer. The five wells were perforated regularly along their entire horizontal laterals, with perforation clusters spaced approximately every 50 feet. The typical stages for Wells A-E were 300 feet long, encompassing six perforation clusters. Wells A, B, D, and E were fractured in 10 total stages, while well C was fractured in 11 total stages.

The pumping and pressure history for a typical stage is presented in Figure 4.3. For a typical stage, water and sand were pumped at a rate of 50-60 bpm for 150 minutes,

with pumped water totaling ~325,000 gallons and pumped sand totaling ~400,000 pounds per stage. The summary pumping statistics for each stage of each well are presented in Table 4.1. A few stages received significantly less water and sand than the average stage. In the microseismic analysis presented in section 4.4, these stages were either removed from the results or noted as atypical.

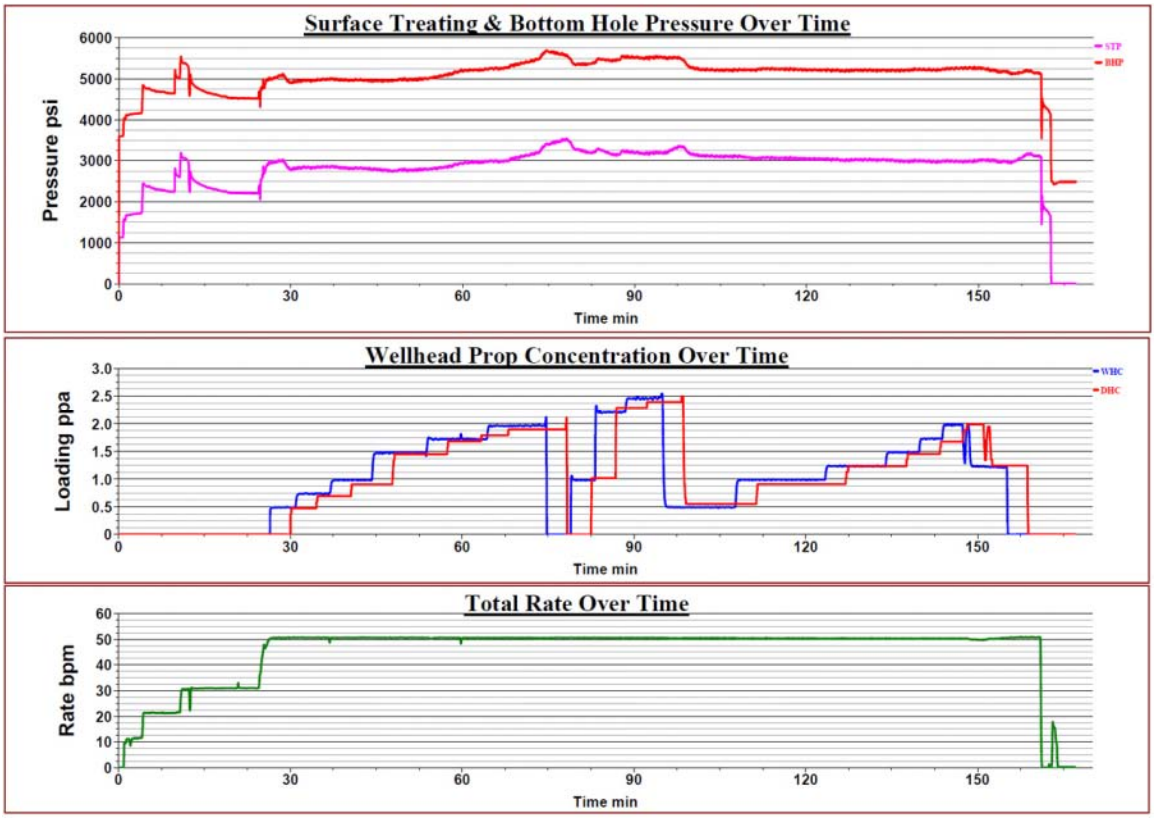

Figure 4.3: Injection history for Well C, Stage 6. Upper panel shows the surface treating pressure (STP) and bottom hole pressure (BHP). Middle panel shows the well head concentration (WHC) and down hole concentration (DHC) of proppant. Lower panel shows the injection rate in barrels per minute (bpm).

Table 4.1: Summary of treatment properties and microseismic statistics for all fracturing stages.

Well A	Injection Time (min)	Injection Rate (bpm)	Injected Water (gallons)	Injected Sand (pounds)	Quake Count (M≥-2.5)	Total Events	a-value	b-value	Detection Threshold	ISIP (psi)
Stage 1	178	55	367,626	440,000	6	69	-6.98	3.18	-2.69	3850
Stage 2	157	55	325,878	392,480	4	43.5	-4.28	2.06	-2.93	3850
Stage 3	158	55	321,888	389,175	6.5	43.5	-4.38	2.17	-2.91	4000
Stage 4	157	55	326,508	398,745	4.5	58	-4.29	2.06	-3.05	4062
Stage 5	160	55	325,038	390,000	20	87.5	-7.08	3.66	-2.78	4181
Stage 6	154	55	320,502	397,620	17.5	85	-3.17	1.86	-2.86	4500
Stage 7	155	55	324,114	346,500	40.5	79.5	-2.90	1.95	-2.54	4850
Stage 8	168	50	287,406	342,600	12	77.5	-4.03	2.17	-2.87	4875
Stage 9	153	50	285,390	338,525	14.5	109.5	-4.42	2.35	-2.82	5175
Stage 10	144	46	255,108	341,595	17.5	74.5	-3.00	1.76	-3.05	4800
Well B										
Stage 1	170	55	367,206	442,500	6	69	-6.98	3.18	-2.69	3700
Stage 2	160	55	326,046	382,600	4	43.5	-4.28	2.06	-2.93	3955
Stage 3	158	56	326,970	391,175	6.5	43.5	-4.38	2.17	-2.91	3900
Stage 4	157	55	324,786	391,625	4.5	58	-4.29	2.06	-3.05	4100
Stage 5	161	55	326,592	388,460	20	87.5	-7.08	3.66	-2.78	4550
Stage 6	154	54	298,494	299,000	17.5	85	-3.17	1.86	-2.86	4550
Stage 7	156	55	326,466	247,000	40.5	79.5	-2.90	1.95	-2.54	5250
Stage 8	169	50	294,924	304,600	12	77.5	-4.03	2.17	-2.87	4950
Stage 9	153	50	285,642	322,440	14.5	109.5	-4.42	2.35	-2.82	4850
Stage 10	196	55	403,536	524,120	17.5	74.5	-3.00	1.76	-3.05	4600
Well C										
Stage 1	104	41	151,326	169,450	0	9	-5.35	2.13	-2.98	3800
Stage 2	150	61	335,034	404,570	5	42	-5.69	2.54	-2.89	3850
Stage 3	156	60	351,918	406,350	27	89	-3.33	1.85	-2.9	3900
Stage 4	154	60	343,896	405,290	23	73	-2.30	1.47	-2.81	4000
Stage 5	180	50	426,426	512,000	20	155	-2.44	1.49	-3.24	4150
Stage 6	160	61	299,208	330,300	21	139	-3.48	1.88	-2.85	4350
Stage 7	164	62	367,626	426,000	35	142	-4.27	2.50	-2.75	4500
Stage 8	144	60	319,326	382,000	21	204	-2.41	1.51	-2.99	4650
Stage 9	131	57	312,018	380,975	33	185	-6.80	3.68	-3	4700
Stage 10	51	52	90,384	94,250	9	69	-7.85	3.49	-2.59	4450
Stage 11	31	40	45,528	42,500	5	63	-3.18	1.54	-3.25	4310

Table 4.1 (continued): Summary of treatment properties and microseismic statistics for all fracturing stages.

Well D	Injection Time (min)	Injection Rate (bpm)	Total Injected Water (gallons)	Total Injected Sand (pounds)	Quake Count (M≥-2.5)	Total Events	a-value	b-value	Detection Threshold	ISIP (psi)
Stage 1	82	47	118,126	135,450	6	53	-3.89	1.87	-3.08	3650
Stage 2	155	60	328,723	399,975	12	113	-12.15	5.24	-2.6	3850
Stage 3	152	60	333,606	399,975	16	80	-3.01	1.61	-3.21	3850
Stage 4	149	60	326,172	401,135	26	97	-3.76	2.05	-2.8	3900
Stage 5	144	61	324,576	400,875	11	100	-4.58	2.26	-2.85	4000
Stage 6	150	62	324,282	402,400	29	115	-10.93	5.13	-2.61	4000
Stage 7	140	61	317,982	391,240	25	86	-11.70	5.42	-2.62	4125
Stage 8	141	56	294,630	361,900	33	171	-5.19	2.68	-2.68	4200
Stage 9	135	55	277,284	325,085	19	123	-2.97	1.68	-3.05	4100
Stage 10	77	52	141,456	168,778	33	150	-5.75	2.89	-2.67	4550
Well E										
Stage 1	80	56	145,110	180,880	0	2	-	-	-	3600
Stage 2	147	60	319,998	404,295	2	12	-3.93	1.69	-2.95	3850
Stage 3	149	60	326,130	404,295	11	41	-14.77	6.56	-2.5	3875
Stage 4	151	60	328,944	399,975	22	100	-5.33	2.63	-2.74	3875
Stage 5	150	60	334,530	401,000	20	90	-5.28	2.65	-2.56	3742
Stage 6	150	62	340,284	405,020	13	69	-17.72	7.94	-2.37	4000
Stage 7	143	60	322,644	390,660	35	144	-3.44	1.93	-2.89	4000
Stage 8	149	55	307,146	356,000	10	93	-3.03	1.59	-3.16	3900
Stage 9	141	55	279,930	337,925	25	132	-4.43	2.31	-2.78	3950
Stage 10	82	51	148,764	167,328	21	89	-4.11	2.09	-2.93	4075

The five wells in the study area were fractured using three different techniques, here referred to as “simulfrac”, “zipperfrac”, and “conventional”. A schematic diagram of these three techniques can be seen in Figure 4.4. Wells A and B (simulfrac) were fractured first, followed by Wells D and E (zipperfrac), and finally Well C (conventional).

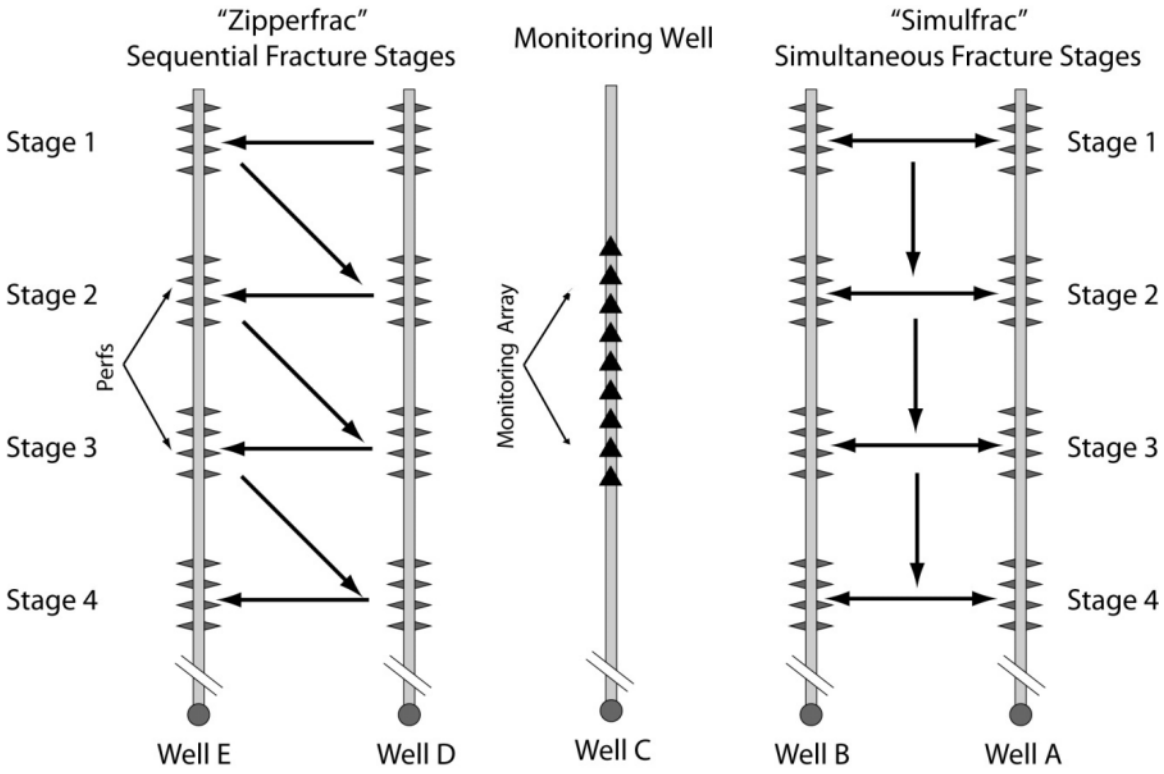

Figure 4.4: Schematic map view of stimulation procedures. Wells A and B were stimulated simultaneously ("simulfrac"). Wells D and E were stimulated sequentially ("zipperfrac"). The monitoring array was moved throughout the operations in order to reduce the distance between the array and the microseismic events.

In the simulfrac method, Stage 1 of Well A and Stage 1 of Well B were fractured simultaneously, with the hope that total connectivity between the two wells and the overall stimulated reservoir volume would be greater than if the wells were fractured individually. After Stage 1 was completed, the simulfrac continued with simultaneous fracturing of Stages 2 through 10 moving from the toe to the heel of the wells. During the simulfrac operation, injection into each well was carried out at a rate of 50-60 bpm. Wells D and E were the next group to be fractured, and were stimulated using a "zipperfrac" method. In the zipperfrac method, the fracturing of Stage 1 of Well D was followed by Stage 1 of Well E, which was followed by Stage 2 of Well D, and so on alternating until all stages were completed. Well C was fractured by itself, the last of the five wells to be stimulated. Well C was surrounded by wells that had already been fractured, thus representing the common case of a well drilled in an infill fashion between existing wells.

4.3.2 Microseismic Monitoring Program

The hydraulic fracturing of the study area wells was monitored by a single string of seismometers designed to detect the small motions generated by the microseismic events triggered during the fracturing process. While better locations can typically be found using two strings of seismometers that detect more ray paths, it is common to use only one tool string for reasons of cost or accessibility to monitoring wells. During stimulation of Wells A & B, an array of nine 3-component seismometers spaced 50 feet apart was placed at various positions in Well C. During stimulation of Wells D & E, an array of ten 3-component seismometers spaced 40 feet apart was placed at various positions in Well C. During fracturing of Well C, an array of twelve 3-component seismometers spaced 35 feet apart was placed in the vertical section of Well B.

4.3.3 Microseismic Locations

Microseismic locations were computed by the microseismic contractor in charge of the acquisition and processing of the microseismic data. The contractor used standard earthquake seismology techniques to detect events, determine their locations, and estimate location errors (Warpinski et al., 1998; Warpinski, 2009; Pinnacle, 2010). The velocity model used to locate the microseismic events was presented in Chapter 3. Typical inversion techniques, such as Geiger's method (Buland, 1976), were used to determine source distance from the P- and S-wave arrivals and triangulate the best fit location of the earthquake. However, due to the limited aperture of the single seismometer string, polarization information of the P- and S-wave arrivals was also used to determine the back azimuth of the microseismic source and thus constrain the possible location area. Advanced earthquake location techniques using double-difference algorithms and tomographic inversion (Waldhauser and Ellsworth, 2000; Zhang and Thurber, 2003) are being investigated to precisely relocate the microseismic events from this same study area (Das and Zoback, 2010).

Figure 4.5a shows the locations of the 4,485 detected events from the 51 hydraulic fracturing stages of Wells A-E. The event cloud shows significant non-uniform distribution of events, including several regions where no events at all were detected. However, when this project was initially analyzed for SRV, many of these areas were

included in the total stimulated volume under the argument that the patchiness and asymmetry were primarily the result of poor detection capabilities. The subjective addition of "missing" SRV and general location error average in the tens to hundreds of feet makes it difficult to assign a confidence to the results of the SRV analysis. Obtaining an accurate estimate of SRV that can be used to compare stimulation success, particularly on a stage-by-stage or well by well basis, remains a challenging task for a typical project.

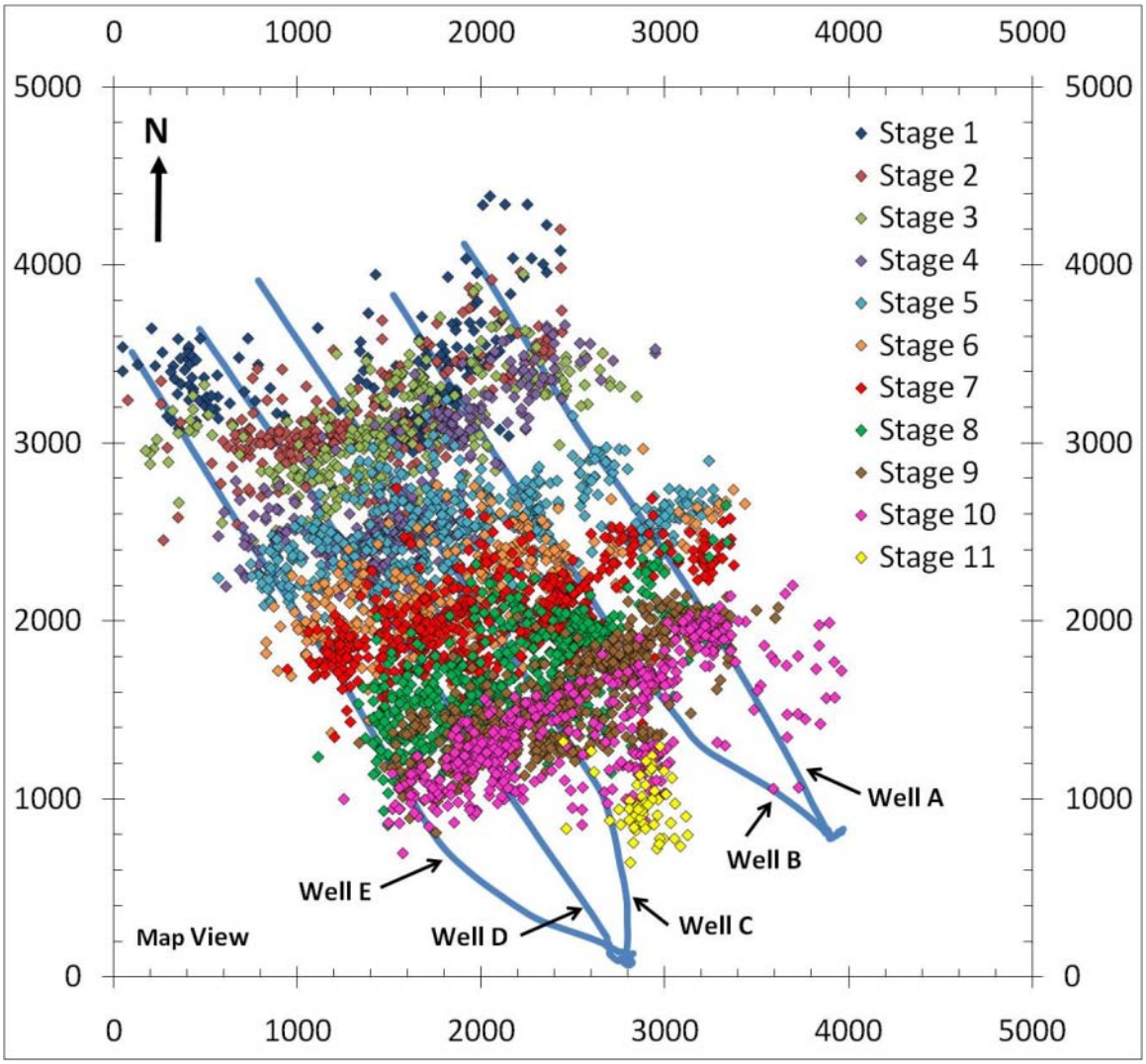

Figure 4.5a: Map view of combined microseismic monitoring results for Wells A-E. Note: wells were fractured individually or in pairs, and thus the stage numbers in this plot are each the aggregate of several independent stages associated with the individual wells.

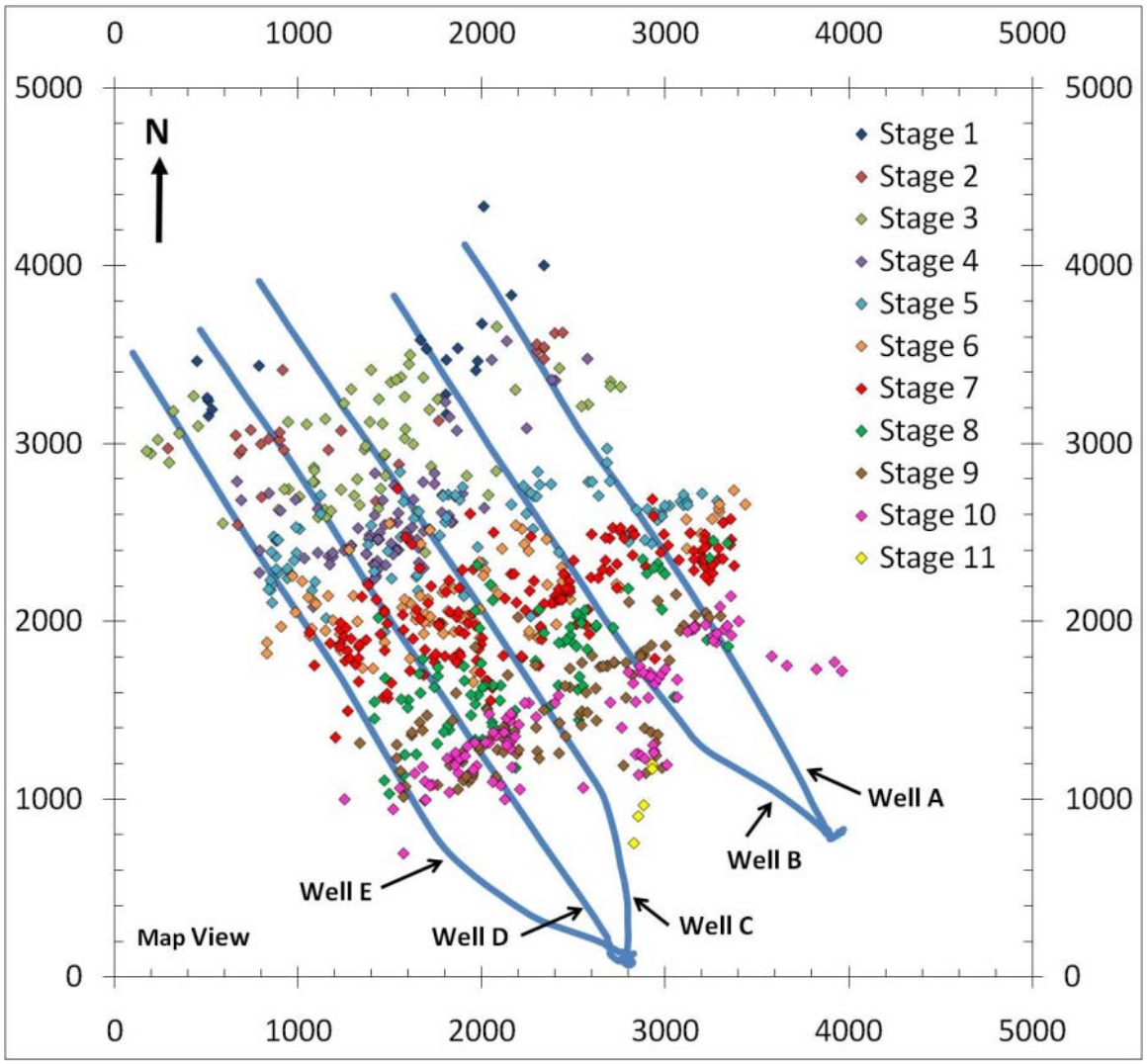

Figure 4.5b: Map view of microseismic events M ≥ -2.5 results for Wells A-E.

4.3.2 Microseismic Magnitudes

The magnitudes of the microseismic events were calculated by the microseismic contractor. Moment magnitudes were calculated from shear wave amplitudes using a modified Hanks/Kanamori equation (Hanks and Kanamori, 1979). The shear wave amplitudes were corrected for distance and attenuation effects before being used to calculate the seismic moment and the moment magnitude.

We did not attempt to re-calculate the microseismic magnitudes reported by the microseismic contractor. Thus, the accuracy of the individual event magnitudes is dependent on the original methods used by the contractor. A recent paper by Shemeta and Anderson (2010) on calculating moment magnitudes for microseismic datasets

demonstrates the uncertainties introduced by the different techniques used to analyze this type of data. While the moments and magnitudes we used in this analysis were calculated using shear wave amplitudes, the microseismic contractor also calculated magnitudes using shear wave corner frequencies and found that the calculated event magnitudes were only insignificantly different (Pinnacle, 2010). Thus, we remain confident that the magnitudes used in this study are as representative of the "true" event magnitudes as is routinely possible to determine given the uncertainty in calculating either shear wave amplitude or corner frequency for such small events.

4.4 Results

4.4.1 Gutenberg-Richter Distributions

We calculated the Gutenberg-Richter parameters for all the stages of Wells A-E using the methods discussed above. We found that nearly all the stages follow a consistent log-linear scaling relationship with a distinct rollover magnitude. Two example curves can be seen for Well C Stage 6 and Well C Stage 8 in Figure 4.6. These two stages exhibit good linear fits with slopes of b = 1.88 and b = 1.51, respectively. It was found for all the analyzed stages that the b-value was significantly greater than 1, indicating an abundance of relatively small events. Thus, the microearthquakes induced during stimulation in our study area do not follow the same magnitude scaling relation as natural earthquakes. A stage-by-stage summary of Gutenberg-Richter parameters can be found in Table 4.1.

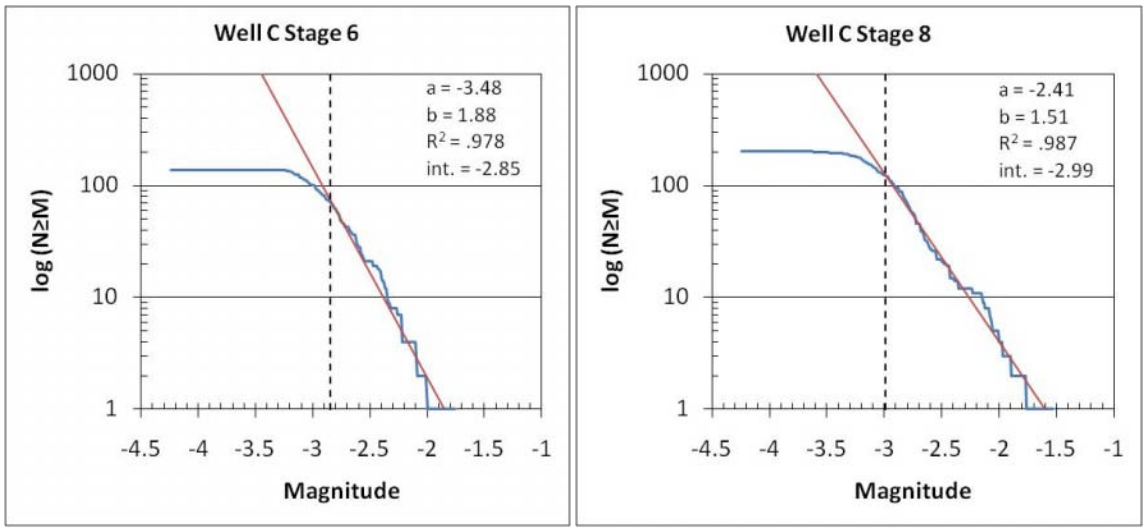

Figure 4.6: Example cumulative Gutenberg-Richter fits from Well C demonstrating steep, varying b-values that prevent direct comparison of a-value as "activity level" proxy. Note that Stage 8 has a slightly higher detection capability (M -2.99) compared to Stage 6 (M -2.85). Stage 8 is approximately 600 ft closer to the monitoring array.

4.4.2 Stimulation Success by Well and by Stage

To use Gutenberg-Richter analysis to quantify hydraulic fracturing success, we first need to establish that there are in fact significant differences in success within our dataset. As seen in Figure 4.7, there is a large variability in the cumulative Gutenberg-Richter curves for the stages of the Well A-B simulfrac. The other wells show similar amounts of variability on a stage-by-stage basis, demonstrating clear differences in activity level among the 51 stages of our dataset. Thus, we should be able to use microseismic magnitude scaling analysis on this dataset to measure the relative success of hydraulic fracturing. However, the stages of Wells A-E also have a large variation in b-value, thus necessitating an empirical activity level metric, as discussed above. In this case, we calculated the total number of events for each stage with magnitude greater than or equal to -2.5. For the set of 51 fracturing stages, M = -2.5 was the smallest magnitude with complete expected detection of events for all stages. This metric is successful at tracking the variability in activity level between the stages, as can be seen visually in Figure 4.7.

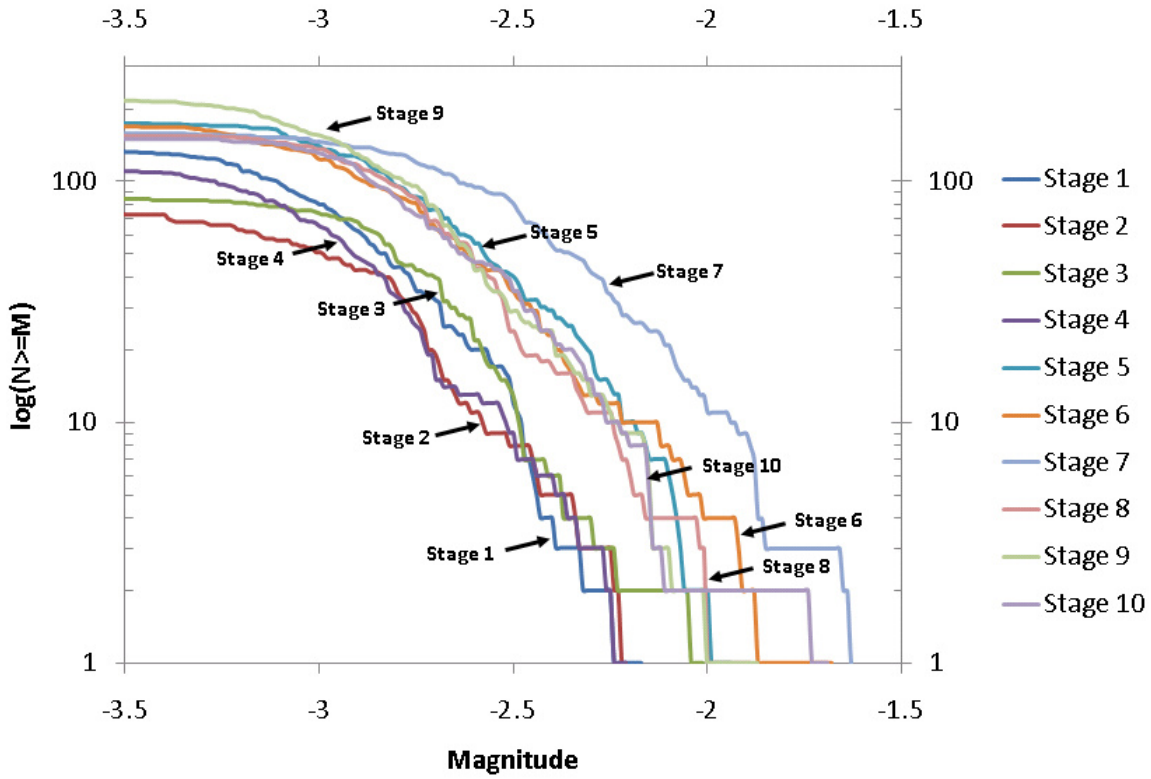

Figure 4.7: Cumulative Gutenberg-Richter plots from the Well A-B "simulfrac" demonstrating significant variability in earthquake activity between the stages.

Excluding the stages that were less than 90 minutes long, the simulfrac (Wells A & B) created 14.3 events per stage, the zipperfrac created 19.3 events per stage, and the conventional frac (Well C) created 20.5 events per stage. These results are consistent with the conclusions from the stimulated reservoir volume analysis conducted by the microseismic contractor that the zipperfrac and conventional frac outperformed the simulfrac. These average values, however, have very large standard deviations that are indicative of the significant variability in activity level on a stage-by-stage basis. Thus, there is important variability on a stage-by-stage basis that is not explained solely by stimulation technique.

4.4.3 Determinants of Stimulation Variability

To investigate this variability, we compared the activity level of the individual stages with various reservoir and operational parameters (Figure 4.8). Gamma ray (and thus clay content/TOC) does not seem to show a strong correlation with activity level, nor does total water or sand injected. However, as seen in Figure 4.8c, the correlation

with stage number indicates that fracturing success generally increases in the later stages. This is suggestive of a cumulative fracturing effect, whereby the later stages are somehow being influenced by the earlier stages to generate more and more events. This cumulative fracturing effect will be investigated in more detail in Chapter 5, where we attempt to model the stress changes in the reservoir and understand the detailed causes of fracturing success variability that we measured in the preceding sections.

4.5 Discussion

We demonstrated above that microseismic magnitude scaling is a robust way to measure stage-by-stage or well-by-well hydraulic fracture stimulation activity level. The technique is designed to compare microearthquake populations both near and far from monitoring arrays on an equivalent quantitative basis. We see this technique as an important complement to traditional means of quantifying hydraulic fracturing stimulation, SRV analysis included. While our method includes information on magnitudes that is not included in other analyses, it does not include potential spatial clustering within an earthquake population. For example, a stage could appear very robust using our statistic even if all the events were tightly clustered in a limited portion of the rock volume. Thus, SRV analysis can be used to measure the spatial extent of stimulation and our magnitude scaling analysis can be used to measure the amount of microearthquake activity within that spatial volume.

Figure 4.5b shows a map of just the events of magnitude $\geq$ -2.5. Recalculating the SRV on just this subset of events would create a more accurate SRV metric based only on events where we expect complete detection. This would eliminate the need to subjectively fill in areas of low detection sensitivity with expected events. The unbiased stimulated volume estimate could then be directly used with our activity level metric to rigorously quantify both the spatial extent of fracturing and the relative robustness of that fracturing.

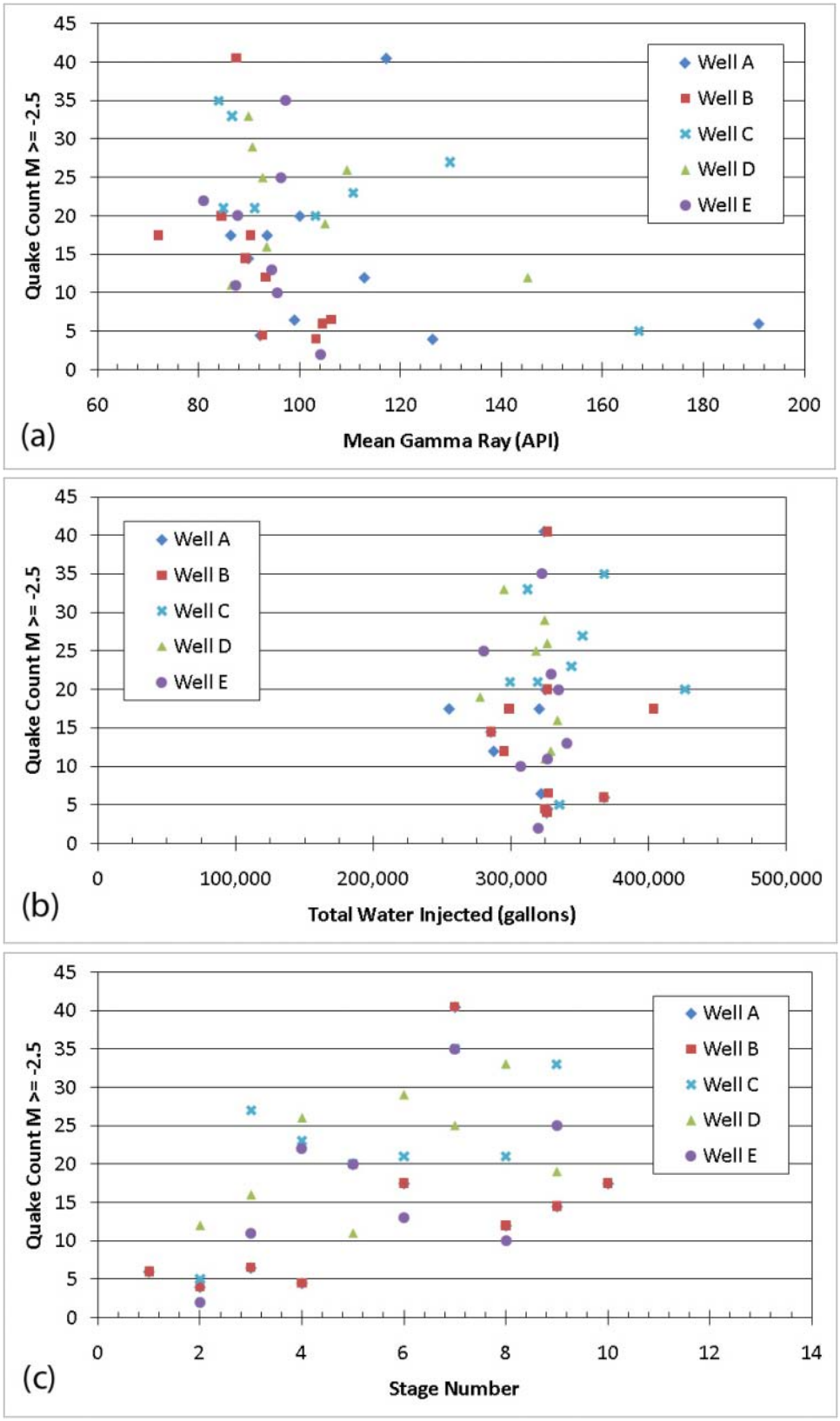

Figure 4.8: Quake count ($M \geq -2.5$) for all wells shows little correlation with (a) gamma ray or (b) total injected water. (c) Stage number does show some correlation.

One possible bias of our stimulation metric is that we indirectly assume that the "true" magnitude distribution follows a log-linear scaling. We calculated our detection threshold cutoff based on fitting the observed data to this assumed distribution of events. This is a reasonable assumption based both on previous studies of microearthquakes in stimulated reservoirs and on the consistent log-linear shapes of the magnitude distributions for our event populations. However, it may possible to determine the "true" distribution of events making no a priori assumptions on the shape of that distribution. Schorlemmer and Woessner (2008) demonstrate how to measure the probability of detecting an event at the individual stations in a network based solely on the history of detection in that network. Thus, rather than imposing an empirical magnitude threshold based on assumptions of log-linearity in the magnitude distribution, it should be possible to use the data itself to create an estimate of the "true" event distribution, with no prior assumptions on the shape of that distribution. This type of analysis will be important in further seismological investigations of the unusually high b-values observed in the microseismic populations generated by hydraulic fracturing. These further analyses should generate insight into why induced microearthquake populations differ from natural earthquake populations and what that may mean for successful stimulation design.

4.6 Conclusions

We used microseismic magnitude scaling analysis to compare the "activity level" of a fracture stage, suggesting a new way to measure stimulation success that does not involve subjective mapping of fractured volumes. As demonstrated above, this metric is easy to calculate using typical magnitude scaling analysis techniques from earthquake seismology. When using this magnitude-based metric, we found significant differences in stimulation robustness for the different fracturing procedures seen in our study area. Our independent analysis of stimulation activity confirmed the results of an earlier analysis using established SRV techniques. Within an individual well, we found stimulation activity level increasing for later stages, a phenomenon we investigate more fully in Chapter 5.

Chapter 5

STRESS EVOLUTION AND PERMEABLE VOLUME CREATION DURING HYDRAULIC FRACTURE STIMULATION

Abstract

We tracked stress evolution in our study reservoir by measuring the instantaneous shut-in pressure (ISIP) at the end of each stage. The ISIP increased stage by stage for all wells, but the simulfrac wells showed the greatest increase and the zipperfrac wells the least. We modeled the stress increase in the reservoir with a simple sequence of 2-D cracks along the length of the well. When using a spacing of one crack per stage, the modeled stress increase was nearly identical to the measured stress increase in the zipperfrac wells. When using three cracks per stage, the modeled final stage stress magnitude matched the measured final stage stress magnitude from the simulfrac wells, but the rate of stress increase in the simulfrac wells was much more gradual than the model had predicted.

To further investigate the causes of these ISIP trends, we began numerical flow and stress analysis to more realistically model the processes in the reservoir. One of our hypotheses was that the shorter total time needed to complete all the stages of the simulfrac wells was the cause of the greater ISIP increase compared to the zipperfrac wells. The microseismic activity level measured in Chapter 4 also correlates with total length of injection, suggesting leak-off into the reservoir encouraged shear failure. Numerical modeling using the coupled FEM and flow software GEOSIM was able to model some cumulative stress increase the reservoir, but the full trend was not replicated. Further work to model field observations of hydraulic fracturing will enhance our understanding of the impact that hydraulic fracturing and stress change have on fracture creation and permeability enhancement in gas shales.

5.1 Introduction

Successful hydraulic fracturing is highly dependent on the in situ stress state in the reservoir. The stress state determines if the hydraulic fracture propagates in a direction that maximizes total connectivity. If stresses are too isotropic, hydraulic fractures might not propagate at all. To generate the widely distributed fracture network seen in reservoirs like the Barnett shale, natural fractures or other planes of weakness must be able to slip in shear as water leaks off during injection and pore pressure increases. Thus, to predict the enhancement of permeability through hydraulic fracturing, it is necessary to characterize the pre-existing stress state in the reservoir and to understand how the stress state evolves during and after hydraulic fracturing. Chapter 3 focused on the pre-existing stress conditions in our Barnett shale study area reservoir; this chapter focuses on direct measurements of stress changes from hydraulic fracturing and the modeling done to explain those stress changes.

5.1.1 Causes of Stress Change

There are three general causes of stress change in the reservoir from hydraulic fracturing. The first source is the dilation of tensile fractures in the reservoir, in particular the dilation of the main hydraulic fracture planes. The primary effect of this dilation is an increase in the magnitude of the least principal stress. Dilation of the main fracture occurs when the active pumping pressure exceeds the least principal stress magnitude. Once pumping ends, pore pressure declines and the fractures have a tendency to close. However, some of the dilation and resultant stress change may become permanent due to the emplacement of proppant in the tensile fractures.

A second source of stress change is caused by poroelastic effects when fluid leaks off from the main hydraulic fracture and increases the pore pressure in the reservoir. While these poroelastic stress changes will in general decrease with distance from the injection source, the resultant stress field distribution will be complicated by the interactions with natural fractures and non-uniform increases in reservoir permeability. The distribution of this pore pressure change is highly coupled to stress-dependent permeability changes and thus cannot be modeled in isolation.

The last major source of stress change is that induced by fracture creation itself. This takes the form of stress concentrations, when Mode I tensile fractures and Mode II/III shear fractures propagate, and stress relaxation, when differential stresses are relieved after shear failure. While these failure-induced stress changes will generally be limited to small, localized reservoir volumes, they may still have significant impact on the spatial distribution of fracture network creation and permeability enhancement.

5.1.2 Analytical and Numerical Stress Modeling

There has been an extensive literature on the process of hydraulic fracturing and its impact on stress in the reservoir. These studies can generally be divided into attempts to model the processes analytically and attempts to model the processes numerically.

To model the stress impact from the dilation of the main hydraulic fracture, it has been common to use analytical models of a crack in an elastic volume. Sneddon (1946) introduced a simple two-dimensional analytical crack model and Green and Sneddon (1950) introduced a significantly more complicated model for an elliptical crack in three-dimensions. Applying the 2-D Sneddon model to stress changes in a reservoir situation, Warpinski and Branagan (1989) modeled the reorientation of hydraulic fractures due to stress changes induced by nearby, earlier hydraulic fractures. Soliman et al. (2000) used the 2-D Sneddon model to investigate the cumulative stress interference from crack opening in multi-stage hydraulic fracturing projects. Both of these studies focused only on the main fracture opening, ignoring the poroelastic stress changes from fracture fluid leak-off into the reservoir. Smith (1985) created an analytical model of fluid leak-off and calculated the impact that the resultant poroelastic stress changes would have on hydraulic fracture design. They found significant changes in reservoir stress for liquid-saturated reservoirs. In order to predict the extent of shear failure in gas shale reservoirs, Palmer et al. (2007) combined the simple, 2-D Sneddon crack model with elliptical poroelastic stress disturbances around the main fracture. Warpinski et al. (2004) created the most rigorous analytical model of hydraulic fracturing in the reservoir, combining the full Green and Sneddon solution for a 3-D elliptical crack with solutions for poroelastic stress changes from the fluid leak-off. They applied their model to the prediction of

microseismicity around a hydraulic fracture and studied the sensitivity of the microseismic cloud to reservoir properties and stimulation design.

Numerical methods of analyzing hydraulic fracturing and microseismic stimulation have been developed to overcome the simplifications and limitations of analytical modeling. Rahman et al. (2002) developed an overall numerical framework for modeling shear dilation and propagation of fractures in the reservoir. They used a stochastically generated natural fracture distribution coupled with models of fracture slip to look at the magnitude and dimensions of permeability enhancement after stimulation. Olson and Dahi-Taleghani (2009) created a numerical model to investigate the interactions between tensile fractures, induced shear fractures, and pre-existing natural fractures with applications to multi-stage hydraulic fracturing projects. They found that fracturing complexity was controlled both by the geometry of the natural fractures and by the magnitudes, directions, and anisotropy of the principal stresses. Nassir et al. (2010) developed a coupled geomechanics and flow model that allowed induced shear failure to dynamically update both the reservoir permeability and the mechanical properties of the fractured volume, with specific application to modeling stimulation in gas shales like the Barnett. Lastly, Roussel and Sharma (2010) looked at interference from multi-stage, multi-well hydraulic fracturing. Their numerical model replicates the results from analytical models of simple well and stage geometries, but enables the modeling of far more complex hydraulic fracturing procedures, as is now typical in the Barnett shale and other gas shale reservoirs.

5.2 Measuring Stress Changes in the Reservoir

One of the challenges of modeling stress changes is tying back model predictions to actual ground-truth measurement from the reservoir. A unique aspect of our Barnett shale study area is that we have multiple sources of information on stress in the reservoir. The first source is our base stress model, as we developed in Chapter 3. Our base stress model for the study area is a normal faulting stress environment with relatively low stress anisotropy and mild overpressure: $S_V = 1.1$ psi/ft, $S_{Hmax} = 0.73$ psi/ft, $S_{hmin} = 0.65$ psi/ft, and $P_p = 0.48$ psi/ft.

A second source of information is the microseismic events detected during the hydraulic fracturing stages. While there is of course uncertainty in the locations of these events, they give general dimensions of the regions in which shear failure has occurred. As discussed in Chapter 3, shear failure is likely to occur on a fracture when shear stress exceeds the effective normal stress multiplied by the coefficient of friction. For an optimally oriented plane, this transition happens when the ratio of maximum effective stress to minimum effective stress exceeds the following ratio:

$$\sigma_1/\sigma_3 = \left(\sqrt{\mu^2+1}+\mu\right)^2 \tag{5.1}$$

where the maximum principal effective stress is $\sigma_1 = S_1 - P_p$, the minimum principal effective stress is $\sigma_3 = S_3 - P_p$, and the coefficient of sliding friction is μ. Since we know the magnitudes of the principal stresses, S_1 and S_3, from our initial stress modeling, we can calculate the pore pressure necessary to trigger slip in the reservoir. We can thus match the dimensions of the microseismic cloud with the pore pressure and stress perturbation that is predicted by stress modeling efforts.

The final source of stress information is the pumping histories from the 51 fracture stages completed in the project. Recordings of bottom-hole pumping pressure versus time can be used to ensure that any injection model properly matches the conditions that were actually observed during the project. More importantly, the pressure history right at the end of pumping reveals information about the least principal stress. After pumping is shut off, the instantaneous shut-in pressure (ISIP) is measured at the point where the slope of the pressure decline curve changes, as seen schematically in Figure 5.1. This change in the pressure decline curve is indicative of the main hydraulic fracture closing as the pore pressure drops below the minimum principal stress (Economides and Nolte, 2000). The ISIP, therefore, is a measurement of the magnitude of the least principal stress. Since we have the pressure history for all of the stages in our study area, we can directly measure the magnitude of the least principal stress as it evolves during the fracturing project. Thus, we can match the stress changes measured in the reservoir with the magnitudes predicted by our modeling efforts.

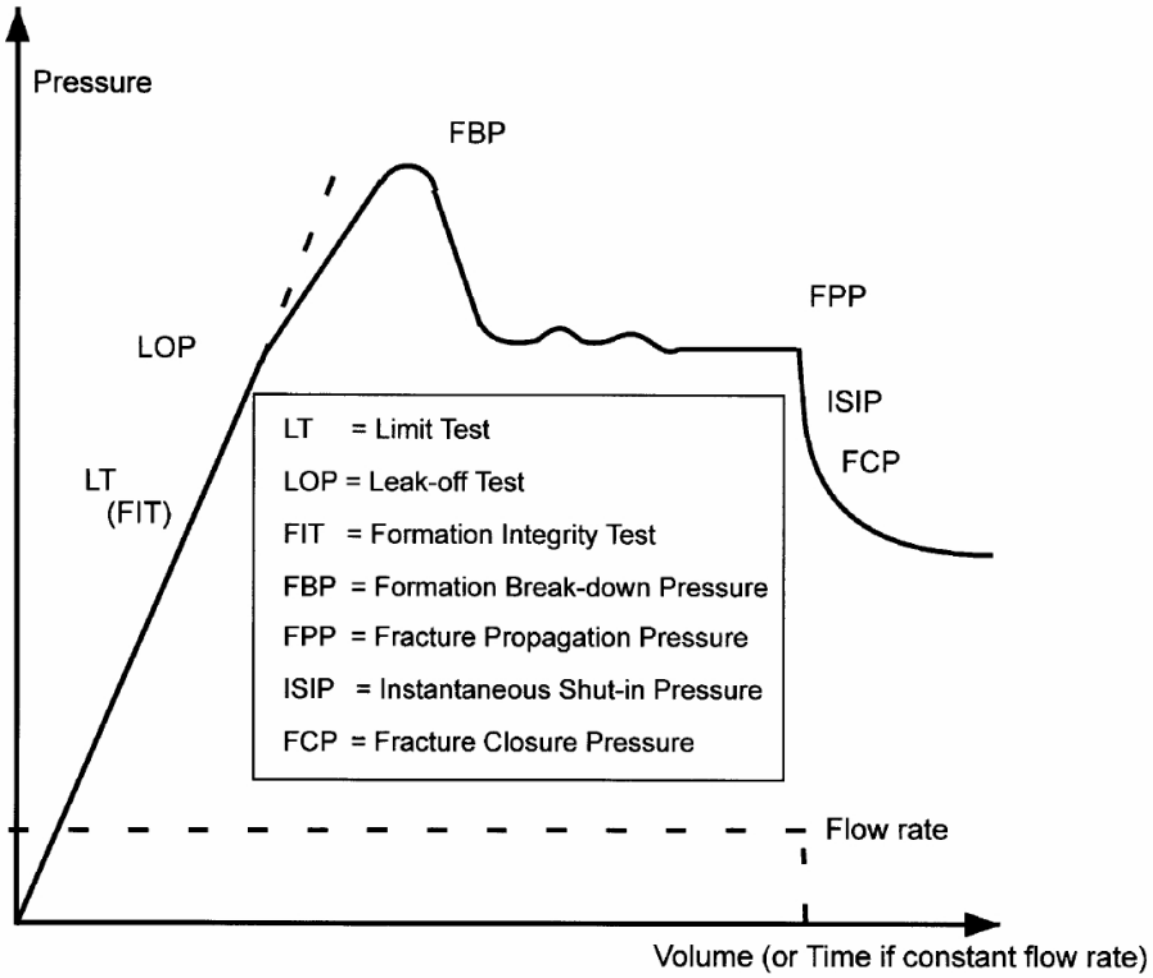

Figure 5.1: Schematic representation of a pumping pressure history, demonstrating instantaneous shut-in pressure (ISIP) at end of test. Source: Zoback et al. (2003), modified from Gaarenstroom, et al. (1993).

An actual example of the ISIP from Well C, Stage 1 is seen in Figure 5.2. The pressure declines very quickly due to the low viscosity of the fracturing fluid. There was also a large water hammer effect, leading to the accuracy of the measured ISIPs to be no better than ±50 psi. In cases where pumping rates and total pumping duration are low, ISIP can give a very accurate determination of this magnitude. However, for a typical Barnett stage with over two hours of pumping water and sand at a high rate, the ISIP is only an approximation of the least principal stress magnitude.

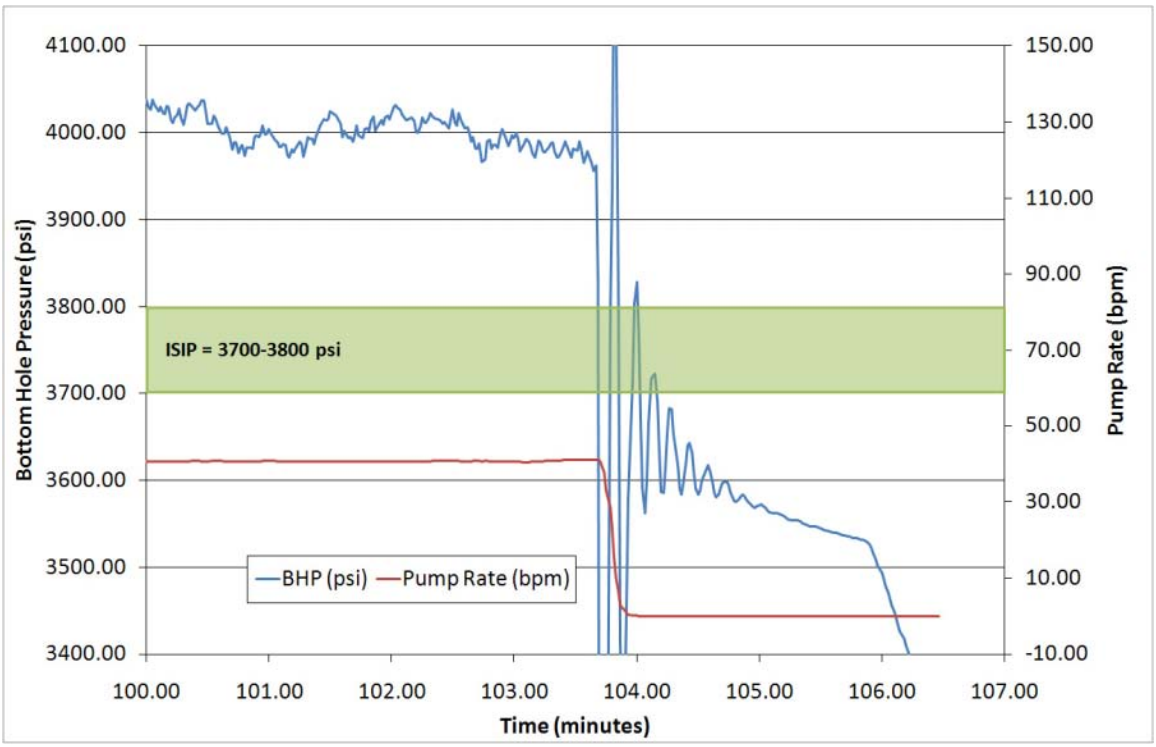

Figure 5.2: Example ISIP curve from Well C, Stage 1. A water hammer effect at the end of pumping causes the ISIP estimation precision to be ± ~50 psi.

Calculated ISIP values for all wells, all stages are seen in Figure 5.3. For all the wells, the ISIP values increase in a steady progression from the early stages to the later stages. A similar effect has been reported in the gas shale literature and explained as a "stress shadow" related to sequential propped planar fractures (East et al., 2004; Fisher et al., 2004; Soliman et al., 2008; Waters et al., 2009). For Wells A, B, and C there is also a fall-off in ISIP magnitude for the last few stages. In section 5.3 below, we test the simple "stress shadow" model as an explanation for the stress increase seen in our study area.

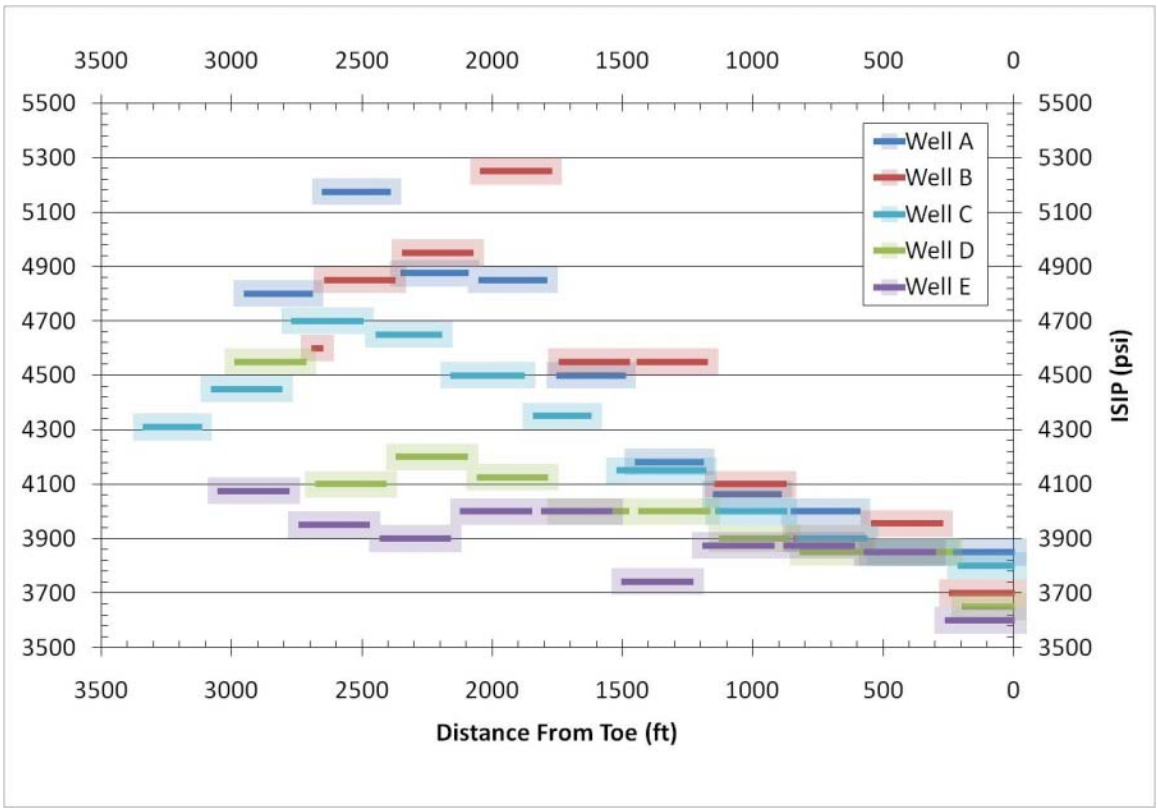

Figure 5.3: ISIPs escalate from toe to heel in all wells. The simulfrac wells, A & B, escalate the most, while the zipperfrac wells, D&E, escalate the least. The length of each solid line represents the length of that fracturing stage and the shaded region represents the uncertainty of each ISIP calculation.

Interestingly, the simulfrac wells (A and B) exhibit the greatest increase in ISIP, while the zipperfrac wells (D and E) exhibit the least. The ISIP for wells A and B increases by over 1200 psi, while it increases by less than 600 psi for wells D and E, with well C in the middle. Tying this measurement of stress change back to the microseismic activity level discussed in Chapter 4, we plot ISIP versus microseismic activity level in Figure 5.4. As seen in the figure, there is a correlation between microseismic activity level and the ISIP value for an individual stage. However, this correlation follows a different trend for the simulfrac wells and the zipperfrac wells. The simulfrac wells escalate to a higher ISIP by the end than the zipperfrac, but actually show less total seismic activity. Thus, while an increase in the minimum principal stress is correlated with additional microearthquake production, the exact impact of these stress changes on the reservoir seems to be controlled by the method of fracturing.

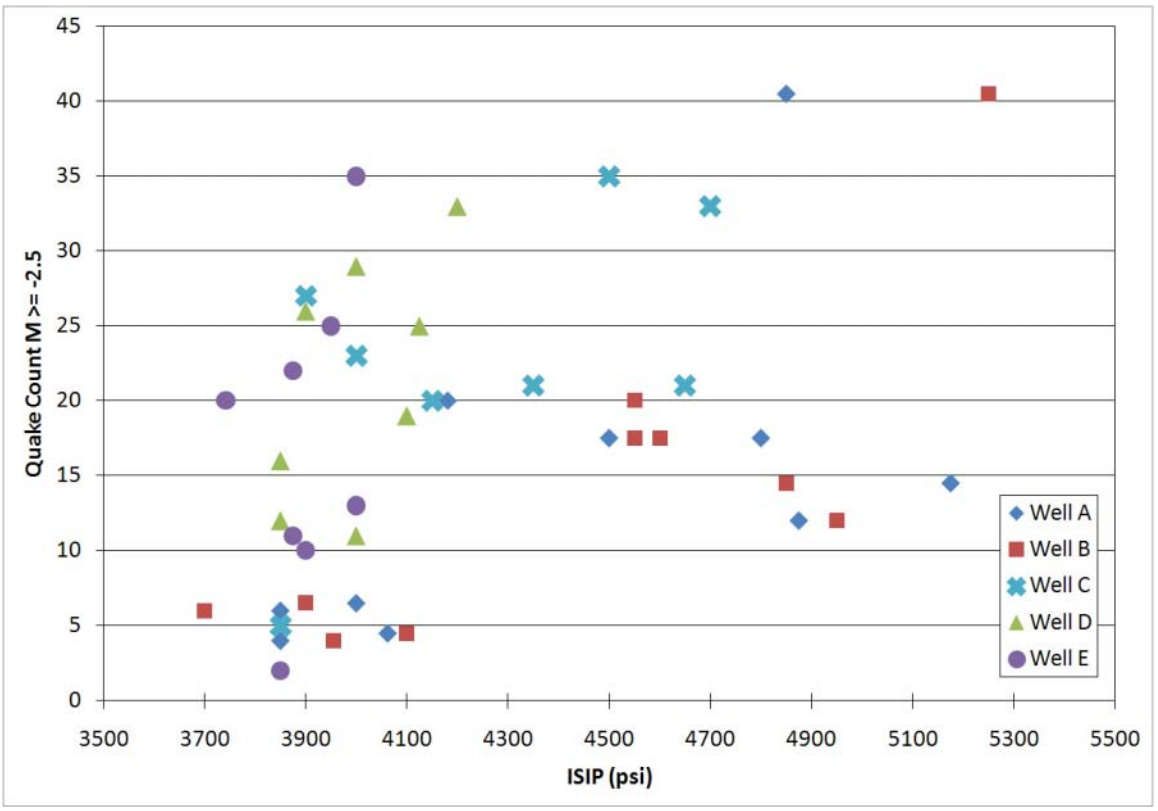

Figure 5.4: The correlation between ISIP and quake count follows a different trend for the simulfrac wells (A and B) and the zipperfrac wells (D and E).

5.3 Analytical Crack Models

To test the claims that the ISIP increases we observed are simple "stress shadows" caused by closely-spaced hydraulic fractures, we utilized the relatively simple 2-D analytical crack model of model of Sneddon (1946). There is some theoretical support that stress changes in the reservoir could be the result of such a simple process. In our study area, the ten stages of an individual well create at a minimum ten large, planar fractures spaced on average 300 feet apart. These main fractures, which are orthogonal to the direction of S_{hmin}, could cumulatively interact with each other to increase the minimum horizontal stress magnitude in the reservoir, and thus the measured ISIP. This increase is likely to be transient when the main fractures are held open by the pumping pressure, but may be permanent if the emplaced proppant can keep the main fracture plane propped open. Thus, the hydraulic fracture from the previous stage may impact the stress felt by the hydraulic fracture of the following stage even if the pore pressure in the

previous stage has declined. After reviewing the theory behind this simple model, we present our attempts to fit the observed stress changes using this model only.

5.3.1 Sneddon Theory and Model Dimensions

In the Sneddon (1946) model, the fractures are 2-dimensional and are modeled as infinite in the S_{Hmax} direction (which is a reasonable approximation since fracture length for our wells is greater than three times the fracture height). The equations used to model the fractures are as follows:

$$
\begin{aligned}
\sigma_A &= -P\left\{\frac{L}{\sqrt{L_1 L_2}}\cos\left[\theta - 1/2\left(\theta_1+\theta_2\right)\right]-1\right\} \\
\sigma_B &= P\left\{\frac{L\sin\theta}{h/2}\left(\frac{h^2/4}{L_1 L_2}\right)^{3/2}\sin\left[\frac{3}{2}\left(\theta_1+\theta_2\right)\right]\right\} \\
\tau_{xy} &= -P\left\{\frac{L\sin\theta}{h/2}\left(\frac{h^2/4}{L_1 L_2}\right)^{3/2}\cos\left[\frac{3}{2}\left(\theta_1+\theta_2\right)\right]\right\} \\
\sigma_y &= 2\mu\sigma_A \\
\sigma_z &= \sigma_A + \sigma_B \\
\sigma_x &= \sigma_A - \sigma_B \\
L &= \sqrt{x^2+z^2} \\
\theta &= \tan^{-1}\left(\frac{x}{-z}\right) \\
L_1 &= \sqrt{x^2+\left(z+h/2\right)^2} \\
\theta_1 &= \tan^{-1}\left(\frac{x}{-z-h/2}\right) \\
L_2 &= \sqrt{x^2+\left(z-h/2\right)^2} \\
\theta_1 &= \tan^{-1}\left(\frac{x}{h/2-z}\right)
\end{aligned}
\qquad (5.2)
$$

where σ_x is the S_{hmin} magnitude, σ_y is the S_{Hmax} magnitude, σ_z is the S_V magnitude, P is the effective "pressure" keeping the fracture open, h is the fracture height, z is the distance above or below the centerline of the fracture, and x is the distance away from the fracture plane, following the nomenclature of Warpinski and Branagan (1989).

For our model, fracture height was set at 300 feet, which is representative of the lengths seen in the microseismic monitoring. Opening pressure was set at 750 psi, which is equivalent to an approximately 2 cm crack for typical Barnett elastic moduli. This pressure is above the average net pumping pressure observed in these wells, and is used to illustrate maximum sensitivity to the stress shadow effect.

5.3.2 Results

Results from a single crack are seen in Figure 5.5. The stress increase from a single crack decays quite quickly away from the fracture plane, leading to a 200 psi stress increase at the center of the next stage. In Figure 5.6, we compare the impact that three different fracture spacing densities would have on the cumulative stress increase in our wells. For a single hydraulic fracture plane per stage, the net stress increase is less than 400 psi. This is approximately the same increase in ISIP seen on average for the zipperfrac wells D and E, but it is significantly less than the over 1200 psi increase seen on average for the simulfrac wells A and B. If we model the effect of three main fracture planes propagating per stage, the stress increases quickly and reaches over 1250 psi by the final stage. If we model six main fractures per stage, each with the same original crack opening distance, the net stress increase reaches over 2500 psi by the final stage.

Thus, to match the net stress increase seen in the simulfrac there would need to be three main fracture planes created per stage; to match the net stress increase seen in the zipperfrac there would need to be only a single main fracture plane per stage. However, the simulfrac wells exhibit a more gradual increase in ISIP than the model predicts. By the third stage, the model predicts over 1000 psi of stress increase, but we measure an ISIP increase of less than 200 psi. In contrast, the single frac per stage model tracks the ISIP measured in the zipperfrac in both magnitude and rate of increase.

The gradual increase in ISIP in the simulfrac wells could be explained if the number of propped fractures were greater in the latter stages than in the early stages. However, no flow tests were conducted after fracturing and we are unable to directly test this hypothesis. To further investigate the contrast in stress increase between the different fracturing methods (and in microseismicity activity as discussed in Chapter 4), we attempt to numerically model stress and flow in the reservoir in the sections below.

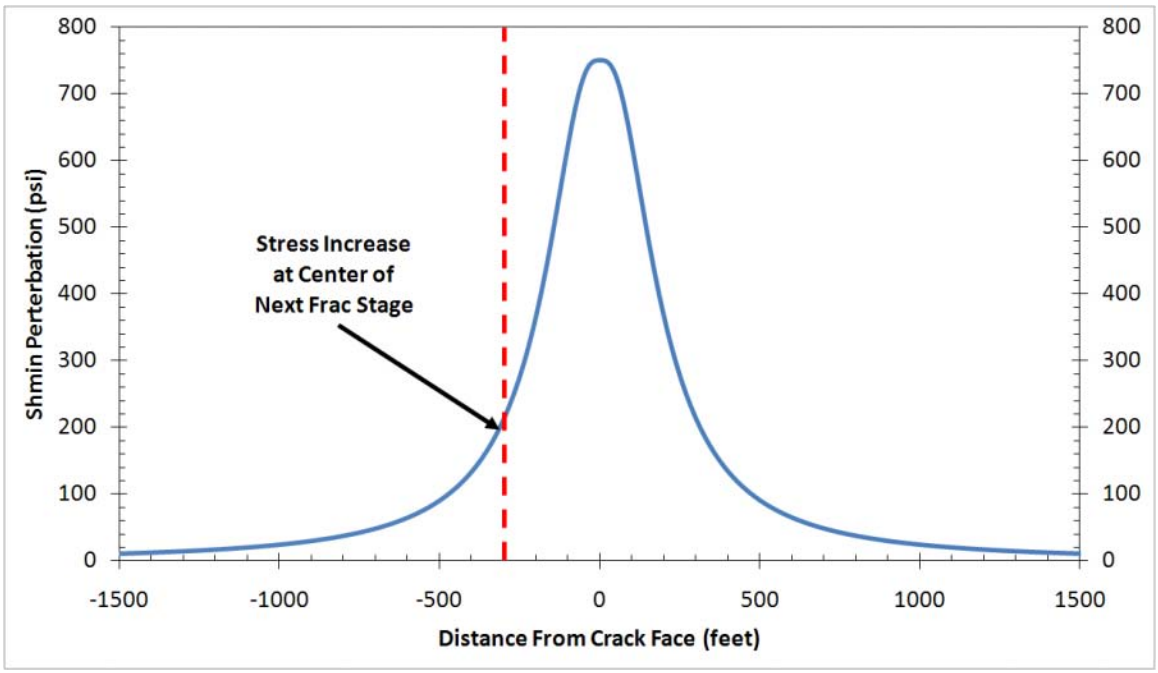

Figure 5.5: Stress increase from a single, semi-infinite Sneddon-type crack 300 ft high. Fluid pressure opening crack in model is 750 psi, equivalent to ~2 cm of total opening.

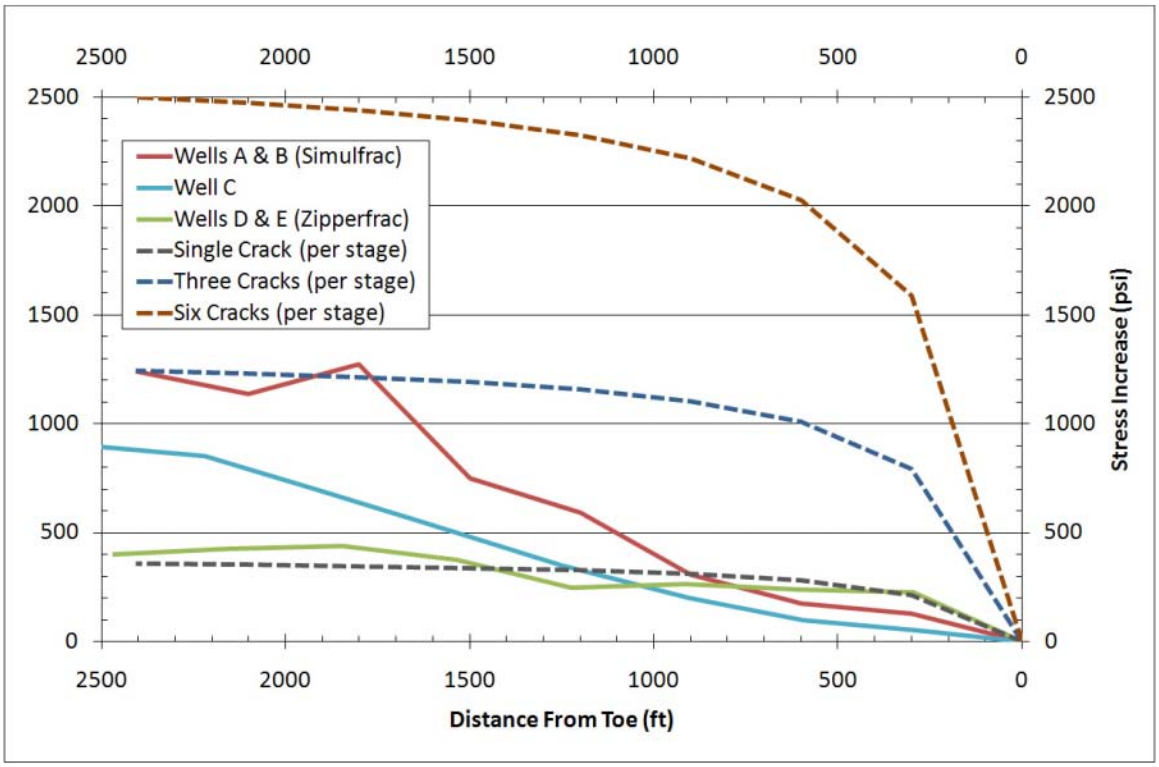

Figure 5.6: Measured ISIP increases from our study area compared against stress increases from a sequential crack model. The simulfrac curve and zipperfrac curve are the averaged ISIP increases for the respective well pairs. The dashed curves represent the stress increase measured at the center of next stage due to the sequential crack propagation. Three models are presented: one hydraulic fracture per stage (300 ft spacing), three per stage (100 ft spacing), or six per stage (50 ft spacing).

5.4 Coupled Numerical Stress and Flow Modeling

One of the major differences between a simulfrac and a zipperfrac is the total amount of time it takes to complete a fracturing job. In our case, since the zipperfrac switched back and forth between wells D and E, it took twice as long to complete all 10 stages as compared to wells A and B. Thus, with only half the time for pressure to leak off, the measured ISIPs in the simulfrac wells are much greater than those seen in the zipperfrac wells. In Figure 5.7, the increase in ISIP as a function of the elapsed time from the first stage shows two different trends, a larger increase for the simulfrac wells and a lower increase for the zipperfrac wells. Well C again shows a trend in the middle of the other wells. Plotting total elapsed time versus the quake count metric we generated in Chapter 4 (Figure 5.8), we see that the quake count correlates well total elapsed time, better than the correlation with stage number (Figure 4.8c). These two plots suggest there may be poroelastic controls to the stimulation phenomena we see in our study area. In the sections below, we discuss our attempts to model poroelastic stress changes.

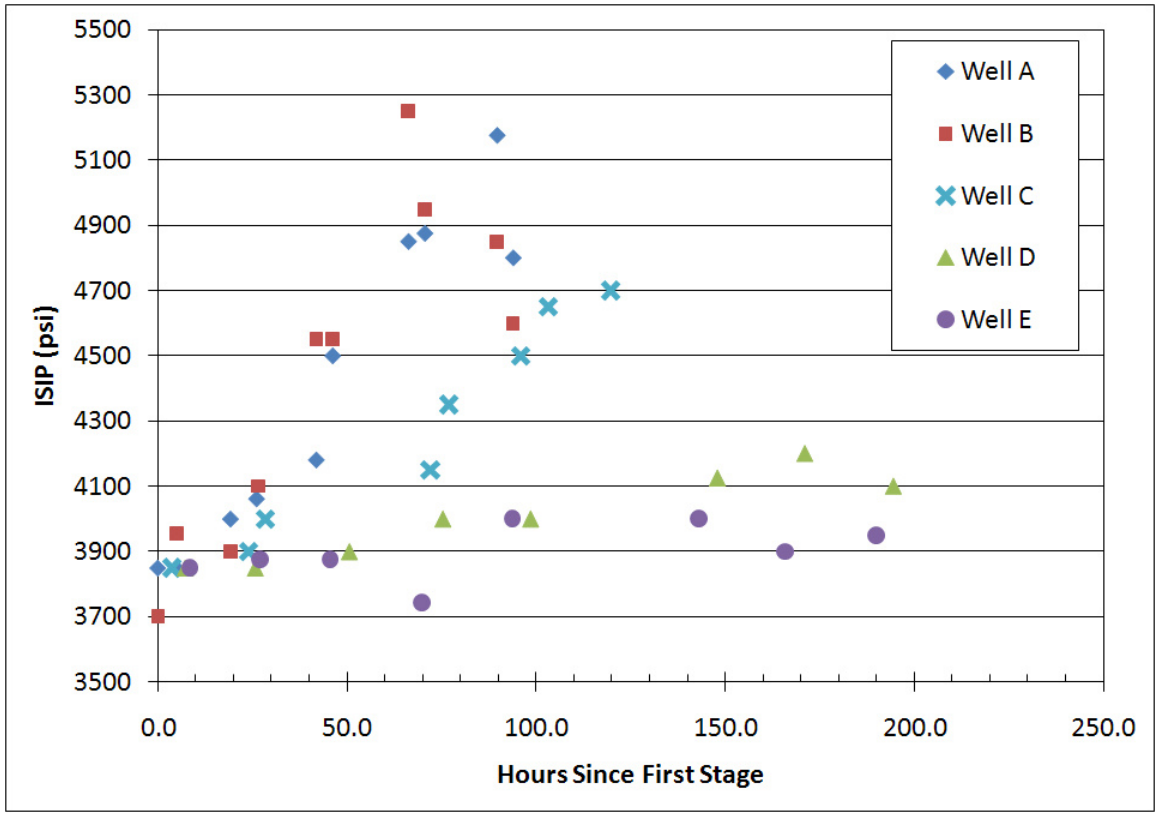

Figure 5.7: ISIP versus elapsed time since the end of the first stage for Wells A-E. Wells A and B (simulfrac) and Wells D and E (zipperfrac) follow significantly different trends. Well C is in the middle, having taken slightly more time than the simulfrac wells but not as long as the zipperfrac wells.

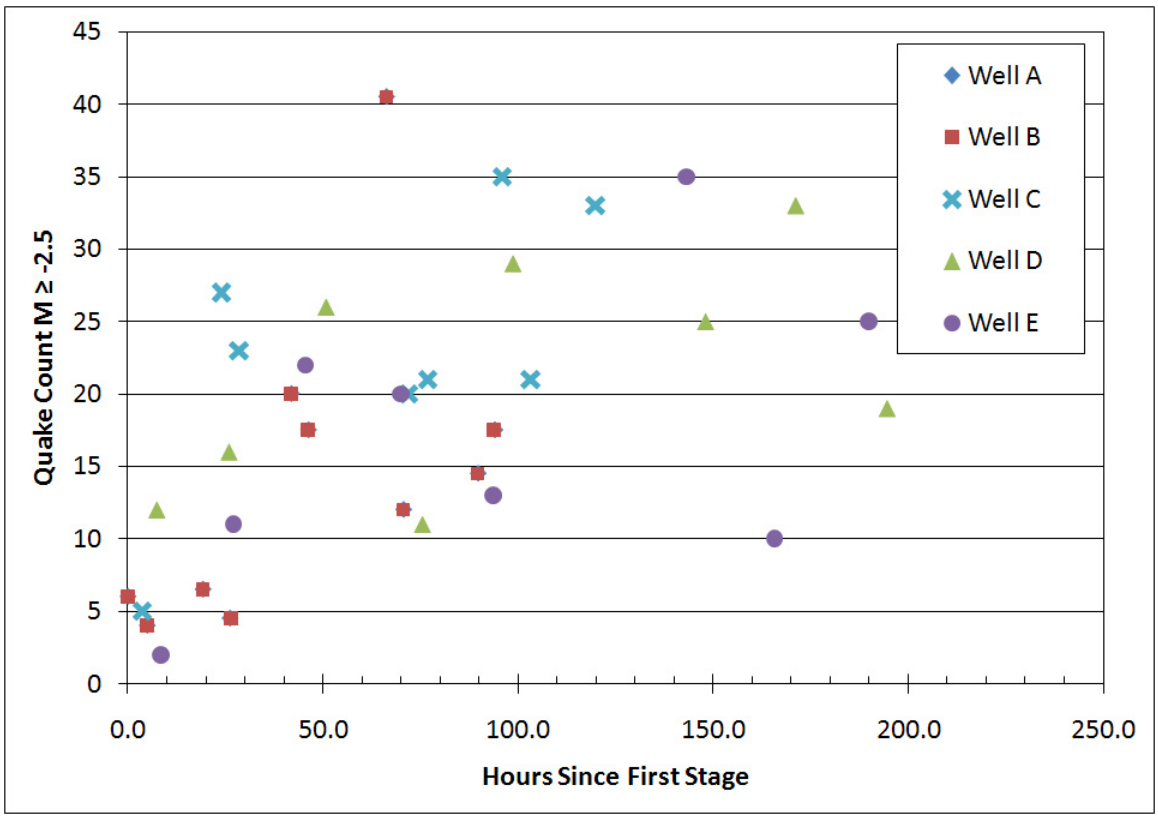

Figure 5.8: Quake count (M ≥ -2.5) versus time since the end of the first stage for Wells A-E. All data points seem to follow the same trend, with total earthquake generation increasing as a function of total elapsed time. This trend may be indicative of beneficial pore pressure diffusion leading to shear failure over a wider area for the late stages in wells D and E.

5.4.1 GEOSIM Software

We investigated poroelastic stress changes in our reservoir through coupled geomechanics and flow simulation using GEOSIM, a commercial software program developed by TAURUS Reservoir Solutions (Settari and Mourits, 1998; Settari and Walters, 2000). GEOSIM couples a finite element stress code (FEM3D) with a black-oil reservoir simulator (TRS). At each time step, the pore pressures within the reservoir simulator are transmitted to the finite element module for calculation of stress changes. These stress changes are sent back to the simulator to update the permeability and porosity of the reservoir model.

5.4.2 Model Setup

We based our numerical models on idealized geometry of our wells and an average of injection parameters for the stages in our study area. We started with best estimates for other input parameters and modified them to match field observations from

the reservoir, including injection pressures, ISIP increases, and the microseismic cloud dimensions. A summary of the key parameters used in our models is shown in Table 5.1. The model has extremely low porosity, much lower than is found in the Barnett shale matrix rock. This mimics flow through a macro-fracture network only. Given the short timescale of water injection, our assumption is that flow through both the matrix and the micro-fractures in the Barnett is negligible during the hydraulic fracture process itself. Thus, it is important to note the macro-fracture permeability used in our numerical models modeling the reservoir numerically is very different from the micro-fracture permeability we measured on intact Barnett samples in Chapter 2.

Table 5.1: Summary of base parameters used in GEOSIM modeling.

Injection Rate (bpm)	Injection Time (min)	Base Porosity	Base Horiz. Perm. (md)	Base Vert. Perm. (md)	Young's Modulus (psia)	Poisson's Ratio	Matrix Bulk Modulus (psia)	Biot Coefficient
0	250	0.0001	1.1	0.11	2.90E+06	0.23	3.59E+06	0.5

We use GEOSIM in dual-phase flow mode (gas and water) with single porosity and permeability. Geomechanics are simplified as linear Mohr-Coulomb. Each grid cell has a base permeability, which is then modified with a permeability multiplier function that is dependent on the current minimum effective stress in that cell (Figure 5.9). At low pore pressures (high effective stresses), the permeability multiplier is low. As pore pressure increases and the effective stress is reduced, the permeability multiplier in each grid cell is increased. This mimics the continuous increase in permeability during hydraulic fracturing as shear planes slip and new fractures are created. We also impose a pseudo-hydraulic fracture plane at the injection point by specifying a stress-dependent permeability multiplier that increases rapidly when the effective stress goes into tension. This mimics the creation and propagation of the main hydraulic fracturing plane in a reservoir. The hydraulic fracture permeability multiplier function is shown in Figure 5.10. We modeled both the simulfrac and zipperfrac wells for the case of a single hydraulic fracture per stage, and also modeled the simulfrac scenario for the case of three hydraulic fractures per stage.

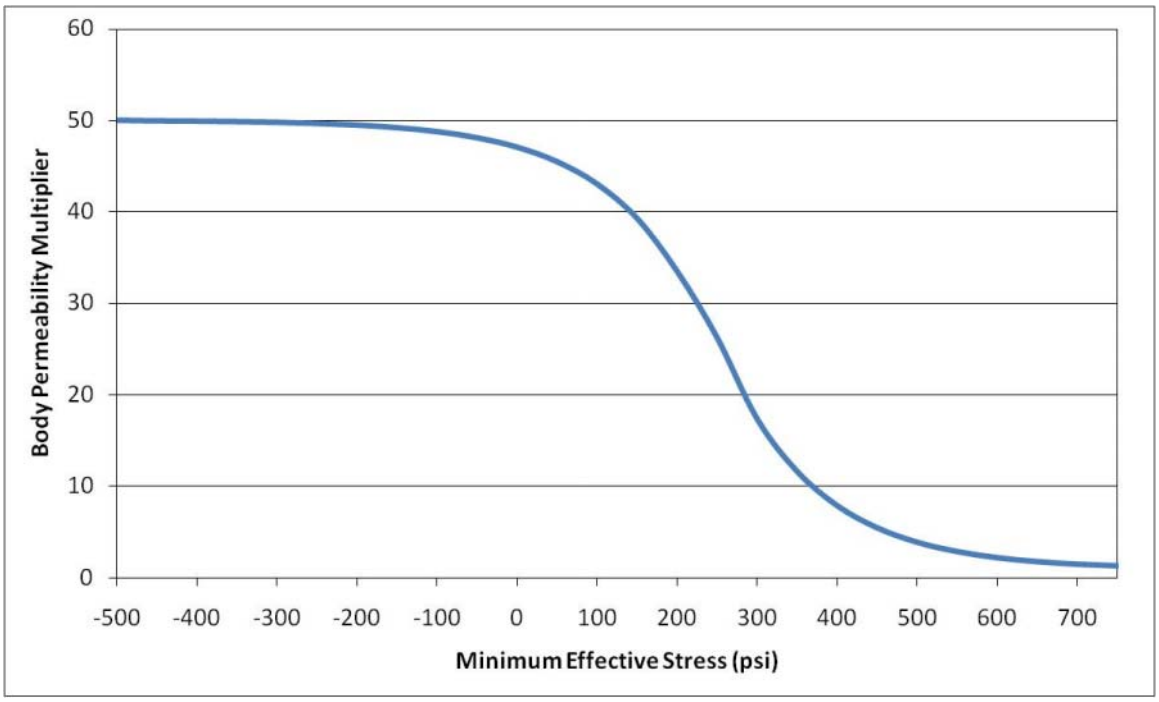

Figure 5.9: Body permeability multiplier versus minimum effective stress. This function mimics the enhanced permeability due to shear failure of fractures in the reservoir.

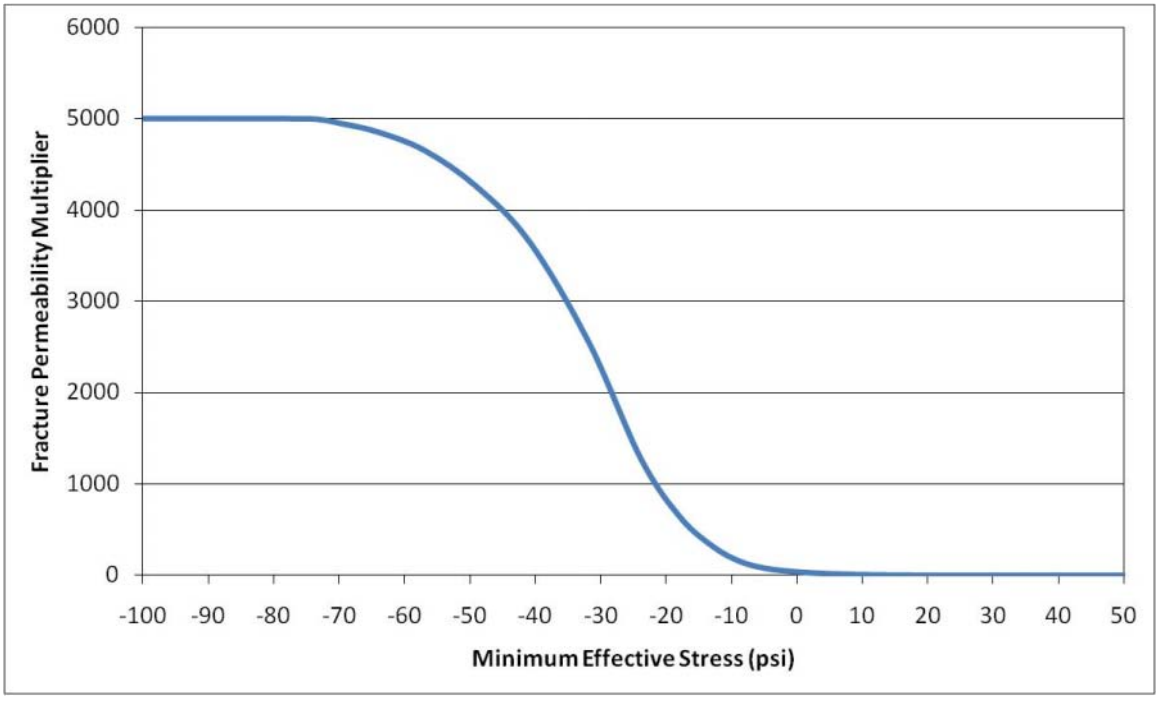

Figure 5.10: Fracture permeability multiplier versus minimum effective stress. This function mimics the opening of a hydraulic fracture when the minimum effective stress goes into tension.

5.4.3 Results

A map view of the water pressure distribution at the end of the first stage of one of our model runs is shown in Figure 5.11. For this same model run, a plot of the injection pressure just before shut-in for the first four stages is shown in Figure 5.12. The end-stage injection pressure is equivalent to the fracture propagation pressure (FPP) in Figure 5.1. Since the fracture propagation pressure is simply the ISIP plus extra pressure related to frictional effects from injection, changes in the FPP serve as a proxy for changes in S_{hmin}. The first two stages show a significant increase in pressure, on the same order as those seen in our study area. However, after the first two stages, the stress increase plateaus quickly and never reaches the 400+ psi increase seen in the wells in our study area. Moreover, the difference in measured pressure between the simulfrac and zipperfrac wells is insignificant, despite the simulfrac pressures dissipating during the long periods between sequential fracture stages. Despite varying porosity and permeability and changing the sensitivity of the reservoir poroelastic parameters, we have not been able to model the difference in simulfrac and zipperfrac behavior using GEOSIM.

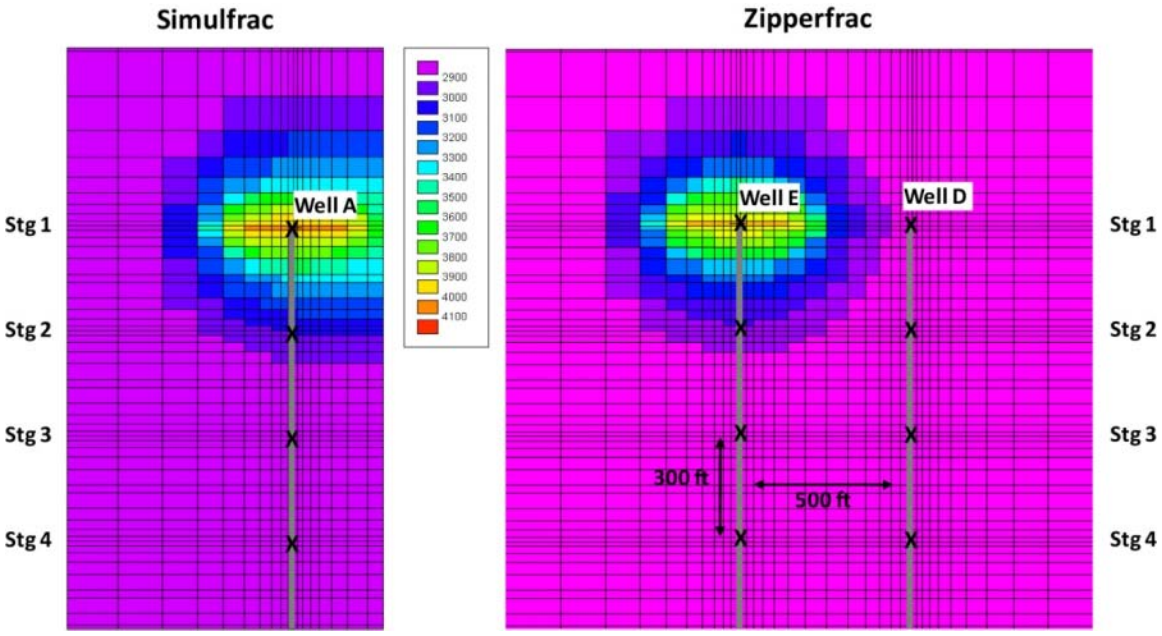

Figure 5.11: Map view of water pressure distribution at end of Stage 1 for simulfrac and zipperfrac models with one hydraulic fracture per stage.

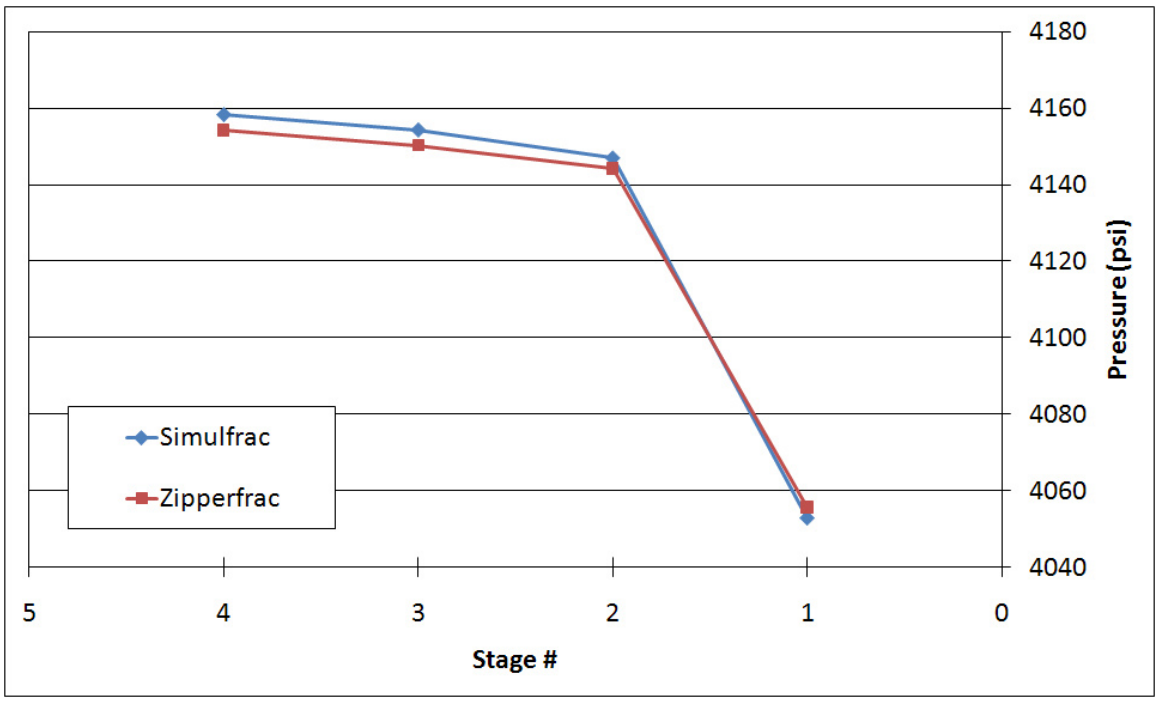

Figure 5.12: End-stage injection pressure for the first four stages of the modeled simulfrac and zipperfrac. The pressures for the first two stages are consistent with pumping data from the field, but the subsequent stages do not exhibit the continual pressure increases seen in Figure 5.3. In addition, the simulfrac and zipperfrac behave similarly, despite the differences in injection procedure and total injection time.

Figure 5.13 shows the water pressure distribution at the end of Stage 1 for a simulfrac model with three hydraulic fractures per stage. The pressure has distributed more widely than in the case of the single fracture per stage model in Figure 5.11. While this leads to high pressures in the reservoir overall (and thus higher stresses), the trend in stress increase in the later stages is similarly modest as that seen in Figure 5.12 for the single fracture per stage case. Thus, even when using multiple fractures per stage, we have been unable to match the primary features we observed in the field – the large increase in stress in later stages and the difference in stress and microearthquake creation between the simulfrac and zipperfrac wells.

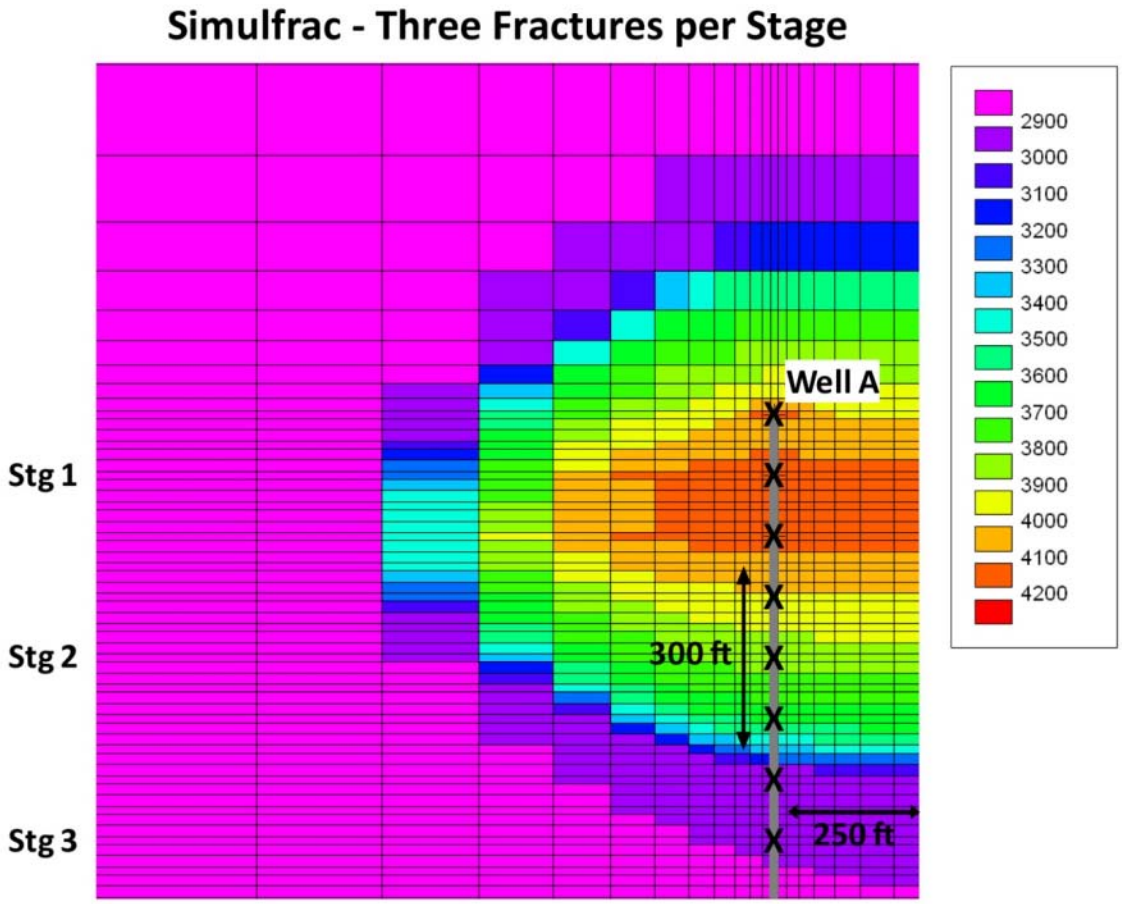

Figure 5.13: Map view of water pressure distribution at end of Stage 1 for a simulfrac with three fractures per stage.

5.5 Discussion and Conclusions

We believe that the multiple observations in this study (including the variation in microseismic activity level, the increase in ISIP in the later hydraulic fracturing stages, and the differences between the simulfrac and zipperfrac results) are related phenomena generated through the same or similar processes. To attempt to comprehensively and cohesively explain these observations, we modeled the hydraulic fracturing process using both analytical and numerical modeling.

We first attempted to model the observed stress increase in the reservoir using a simple sequence of 2-D cracks along the length of the well. When using a spacing of one crack per stage, the modeled stress increase was nearly identical to the measured stress increase in the zipperfrac wells. When using three cracks per stage, the modeled final

stage stress magnitude matched the measured final stage stress magnitude from the simulfrac wells, but the rate of stress increase in the simulfrac wells was much more gradual than the model had predicted. In addition, these simple analytical crack models offer no insight as to why zipperfrac and simulfrac wells would behave differently.

One of our hypotheses was that the shorter total time needed to complete all the stages of the simulfrac wells led to the greater ISIP increase compared to the zipperfrac wells. The microseismic activity level measured in Chapter 4 also correlates with total length of injection, suggesting leak-off into the reservoir encouraged shear failure. Numerical modeling using the coupled FEM and flow software GEOSIM was able to model some cumulative stress increase the reservoir, but the full trend was not replicated. Further work to model field observations of hydraulic fracturing will enhance our understanding of the impact that hydraulic fracturing and stress change have on fracture creation and permeability enhancement in gas shales.

REFERENCES

Abercrombie, R.E., 1996, The magnitude-frequency distribution of earthquakes recorded with deep seismometers at Cajon Pass, southern California: Tectonophysics, v. 261, p. 1-7.

Aki, K., 1965, Maximum Likelihood Estimate of b in the Formula log N = a - bM and its Confidence Limits: Bulletin of the Earthquake Research Institute, v. 43, p. 237-239.

Aki, K., 1987, Magnitude-Frequency Relation for Small Earthquakes: A Clue to the Origin of f max of Large Earthquakes: Journal of Geophysical Research, v. 92, p. 1349-1355.

Baig, A., and Urbancic, T., 2010, Microseismic moment tensors: A path to understanding frac growth: The Leading Edge, v. 29, p. 320-324.

Bernabe, Y., 1986, The effective pressure law for permeability in Chelmsford granite and Barre granite: International Journal of Rock Mechanics and Mining Sciences & Geomechanics Abstracts, v. 23, p. 267-275.

Bernabe, Y., 1987, The Effective Pressure Law For Permeability During Pore Pressure and Confining Pressure Cycling of Several Crystalline Rocks: Journal of Geophysical Research, v. 92, p. 649-657.

Boettcher, M.S., McGarr, A., and Johnston, M., 2009, Extension of Gutenberg-Richter distribution to M < -1.3, no lower limit in sight: Geophysical Research Letters, v. 36, p. L10307.

Bowker, K.A., 2007, Barnett Shale gas production, Fort Worth Basin: Issues and discussion: AAPG Bulletin, v. 91, p. 523-533.

Brace, W.F., Walsh, J.B., and Frangos, W.T., 1968, Permeability of Granite under High Pressure: Journal of Geophysical Research, v. 73, p. 2225-2236.

Brunauer, S., Deming, L.S., Deming, W.E., and Teller, E., 1940, On a Theory of the van der Waals Adsorption of Gases: Journal of the American Chemical Society, v. 62, p. 1723-1732.

Brunauer, S., Emmett, P.H., and Teller, E., 1938, Adsorption of Gases in Multimolecular Layers: Journal of the American Chemical Society, v. 60, p. 309-319.

Buland, R., 1976, The mechanics of locating earthquakes: Bulletin of the Seismological Society of America, v. 66, p. 173-187.

Busch, A., Alles, S., Gensterblum, Y., Prinz, D., Dewhurst, D.N., Raven, M.D., Stanjek, H., and Krooss, B.M., 2008, Carbon dioxide storage potential of shales: International Journal of Greenhouse Gas Control, v. 2, p. 297-308.

Bustin, R.M., Bustin, A.M.M., Cui, A., Ross, D., and Pathi, V.M., 2008, Impact of Shale Properties on Pore Structure and Storage Characteristics: SPE Shale Gas Production Conference.

Cipolla, C.L., Warpinski, N.R., Mayerhofer, M.J., Lolon, E., and Vincent, M.C., 2008, The Relationship Between Fracture Complexity, Reservoir Properties, and Fracture Treatment Design: SPE Annual Technical Conference and Exhibition, 115.

Cui, X., Bustin, A.M.M., and Bustin, R.M., 2009, Measurements of gas permeability and diffusivity of tight reservoir rocks: different approaches and their applications: Geofluids, v. 9, p. 208-223.

Das, I., and Zoback, M.D., 2010, Feasibility study of using travel-time tomography to map variations of shale gas reservoir properties and improve microearthquake locations: Stanford Rock Physics and Borehole Geophysics Project, v. 121.

East, L.E., Grieser, W., McDaniel, B.W., Johnson, B., Jackson, R., and Fisher, K., 2004, Successful Application of Hydrajet Fracturing on Horizontal Wells Completed in a Thick Shale Reservoir: SPE Eastern Regional Meeting.

Economides, M.J., and Nolte, K.G., 2000, Reservoir Stimulation: Chichester, England ; New York, John Wiley.

EIA, 1998, Natural Gas 1998 Issues and Trends.

EIA, 2010a, Annual Energy Outlook 2010.

EIA, 2010b, Annual Energy Review 2009.

EIA, 2010c, International Energy Outlook 2010.

EIA, 2010d, Shale Gas Plays, Lower 48 States.

EIA, 2010e, U.S. Crude Oil, Natural Gas, and Natural Gas Liquids Proved Reserves, 2009.

Eisner, L., Williams-Stroud, S., Hill, A., Duncan, P., and Thornton, M., 2010, Beyond the dots in the box: Microseismicity-constrained fracture models for reservoir simulation: The Leading Edge, v. 29, p. 326-333.

Felzer, K., 2006, Calculating the Gutenberg-Richter b value: Eos Trans. AGU Fall Meet. Suppl., v. 87.

Fisher, M.K., Heinze, J.R., Harris, C.D., Davidson, B.M., Wright, C.A., and Dunn, K.P., 2004, Optimizing Horizontal Completion Techniques in the Barnett Shale Using Microseismic Fracture Mapping: SPE Annual Technical Conference and Exhibition, 90051-MS.

Gaarenstroom, L., and Tromp, R.A.J., 1993, Overpressures in the Central North Sea: implications for trap integrity and drilling safety: Petroleum Geology of Northwest Europe: Proceedings of the 4th Conference, London.

GMI, 2010, Stress and Failure in Inclined Boreholes (SFIB).

Goodway, B., Varsek, J., and Abaco, C., 2006, Practical applications of P-wave AVO for unconventional gas Resource Plays - I: Seismic petrophysics and isotropic AVO: CSEG Recorder, v. Special Edition.

Green, A.E., and Sneddon, I.N., 1950, The distribution of stress in the neighbourhood of a flat elliptical crack in an elastic solid: Mathematical Proceedings of the Cambridge Philosophical Society, v. 46, p. 159-163.

Grieser, W.V., and Bray, J.M., 2007, Identification of Production Potential in Unconventional Reservoirs: Production and Operations Symposium, 106623-MS.

Gutenberg, B., and Richter, C.F., 1944, Frequency of earthquakes in California: Bulletin of the Seismological Society of America, v. 34, p. 185-188.

Guttorp, P., 1987, On least-squares estimation of b values: Bulletin of the Seismological Society of America, v. 77, p. 2115-2124.

Hanks, T.C., and Kanamori, H., 1979, A moment magnitude scale: Journal of Geophysical Research, v. 84, p. 2348-2350.

IPCC, 2005, Carbon Dioxide Capture and Storage.

Jaeger, J.C., 1979, Fundamentals of rock mechanics: London :, Chapman and Hall ;.
Kang, S.M., Fathi, E., Ambrose, R.J., Akkutlu, I.Y., and Sigal, R.F., 2010, CO2 Storage Capacity of Organic-Rich Shales: SPE Annual Technical Conference and Exhibition, 134583-MS.
Kassis, S.M., and Sondergeld, C.H., 2010, Gas Shale Permeability: Effects of Roughness, Proppant, Fracture Offset, and Confining Pressure: International Oil and Gas Conference and Exhibition in China, 131376-MS.
Kidney, R.L., Zimmer, U., and Boroumand, N., 2010, Impact of distance-dependent location dispersion error on interpretation of microseismic event distributions: The Leading Edge, v. 29, p. 284-289.
Klinkenberg, L.J., 1941, The Permeability Of Porous Media To Liquids And Gases: Drilling and Production Practice, 41-200.
Kovscek, A.R., Tang, G.-Q., and Jessen, K., 2005, Laboratory and Simulation Investigation of Enhanced Coalbed Methane Recovery by Gas Injection: SPE Annual Technical Conference and Exhibition, 95947-MS.
Kwon, O., Kronenberg, A.K., Gangi, A.F., and Johnson, B., 2001, Permeability of Wilcox shale and its effective pressure law: Journal of Geophysical Research, v. 106, p. 19339-19353.
Langmuir, I., 1916, The Constitution and Fundamental Properties of Solids and Liquids. Part I. Solids: Journal of the American Chemical Society, v. 38, p. 2221-2295.
Li, M., Bernabé, Y., Xiao, W.I., Chen, Z.Y., and Liu, Z.Q., 2009, Effective pressure law for permeability of E-bei sandstones: Journal of Geophysical Research, v. 114, p. B07205.
Lin, W., 2009, Gas Sorption and the Consequent Volumetric and Permeability Change of Coal, Stanford University Dissertation.
Lombardi, A.M., 2003, The Maximum Likelihood Estimator of b-Value for Mainshocks: Bulletin of the Seismological Society of America, v. 93, p. 2082-2088.
Loucks, R.G., Reed, R.M., Ruppel, S.C., and Jarvie, D.M., 2009, Morphology, Genesis, and Distribution of Nanometer-Scale Pores in Siliceous Mudstones of the Mississippian Barnett Shale: Journal of Sedimentary Research, v. 79, p. 848-861.
Loucks, R.G., and Ruppel, S.C., 2007, Mississippian Barnett Shale: Lithofacies and depositional setting of a deep-water shale-gas succession in the Fort Worth Basin, Texas: AAPG Bulletin, v. 91, p. 579-601.
Lu, X.-C., Li, F.-C., and Watson, A.T., 1995a, Adsorption measurements in Devonian shales: Fuel, v. 74, p. 599-603.
Lu, X.-C., Li, F.-C., and Watson, A.T., 1995b, Adsorption Studies of Natural Gas Storage in Devonian Shales: SPE Formation Evaluation, v. 10, p. 109-113.
Main, I., 1996, Statistical physics, seismogenesis, and seismic hazard: Reviews of Geophysics, v. 34, p. 433-462.
Martineau, D.F., 2007, History of the Newark East field and the Barnett Shale as a gas reservoir: AAPG Bulletin, v. 91, p. 399-403.
Marzocchi, W., and Sandri, L., 2003, A review and new insights on the estimation of the b-value and its uncertainty: Annals of Geophysics, v. 46, p. 1271-1282.
Matthews, H.L., Schein, G.W., and Malone, M.R., 2007, Stimulation of Gas Shales: They're All the Same - Right?: SPE Hydraulic Fracturing Technology Conference.

Maxwell, S.C., 2009, Assessing the Impact of Microseismic Location Uncertainties On Interpreted Hydraulic Fracture Geometries: SPE Annual Technical Conference and Exhibition, SPE-125121-MS.

Maxwell, S.C., Shemeta, J.E., Campbell, E., and Quirk, D.J., 2008, Microseismic Deformation Rate Monitoring: SPE Annual Technical Conference and Exhibition, 116596-MS.

Maxwell, S.C., Waltman, C., Warpinski, N.R., Mayerhofer, M.J., and Boroumand, N., 2006, Imaging Seismic Deformation Induced by Hydraulic Fracture Complexity: SPE Annual Technical Conference and Exhibition, 102801-MS.

Mayerhofer, M.J., Lolon, E., Warpinski, N.R., Cipolla, C.L., Walser, D.W., and Rightmire, C.M., 2010, What Is Stimulated Reservoir Volume?: SPE Production & Operations, v. 25, p. pp. 89-98.

McKinsey, 2008, Carbon Capture & Storage: Assessing the Economics.

McKinsey, 2009, Pathways to a Low-Carbon Economy: Version 2 of the Global Greenhouse Gas Abatement Cost Curve.

Montgomery, S.L., Jarvie, D.M., Bowker, K.A., and Pollastro, R.M., 2005, Mississippian Barnett Shale, Fort Worth basin, north-central Texas: Gas-shale play with multi-trillion cubic foot potential: AAPG Bulletin, v. 89, p. 155-175.

Nassir, M., Settari, A., and Wan, R.G., 2010, Modeling Shear Dominated Hydraulic Fracturing as a coupled fluid-solid interaction: International Oil and Gas Conference and Exhibition in China, 131736-MS.

NETL, 2010, Fossil Energy Cost and Performance Baseline Studies.

NIST, 2007, NIST Reference Fluid Thermodynamic and Transport Properties Database (REFPROP): Version 9.0.

Nuttall, B.C., Eble, C.F., Drahovzal, J.A., and Bustin, R.M., 2005, Analysis of Devonian Black Shales in Kentucky for Potential Carbon Dioxide Sequestration and Enhanced Natural Gas Production.

Olson, J.E., and Taleghani, A.D., 2009, Modeling simultaneous growth of multiple hydraulic fractures and their interaction with natural fractures: SPE Hydraulic Fracturing Technology Conference.

Oye, V., Bungum, H., and Roth, M., 2005, Source Parameters and Scaling Relations for Mining-Related Seismicity within the Pyhasalmi Ore Mine, Finland: Bulletin of the Seismological Society of America, v. 95, p. 1011-1026.

Palisch, T.T., Vincent, M.C., and Handren, P.J., 2008, Slickwater Fracturing: Food for Thought: SPE Annual Technical Conference and Exhibition.

Palmer, I.D., Moschovidis, Z.A., and Cameron, J.R., 2007, Modeling Shear Failure and Stimulation of the Barnett Shale After Hydraulic Fracturing: SPE Hydraulic Fracturing Technology Conference.

Peters, K.E., 1986, Guidelines for evaluating petroleum source rock using programmed pyrolysis: AAPG Bulletin, v. 70, p. 318-329.

Peters, K.E., and Cassa, M.R., 1994, Applied Source Rock Geochemistry, *in* Magoon, L.B., and Dow, W.G., eds., The Petroleum System: From Source to Trap, Volume 60, AAPG Memoir.

Pinnacle, 2010, Personal communication.

Pollastro, R.M., 2007, Total petroleum system assessment of undiscovered resources in the giant Barnett Shale continuous (unconventional) gas accumulation, Fort Worth Basin, Texas: AAPG Bulletin, v. 91, p. 551-578.

Potential Gas Committee, 2008, Potential Supply of Natural Gas in the United States.

Rahman, M.K., Hossain, M.M., and Rahman, S.S., 2002, A shear-dilation-based model for evaluation of hydraulically stimulated naturally fractured reservoirs: International Journal for Numerical and Analytical Methods in Geomechanics, v. 26, p. 469-497.

Ross, D.J.K., and Bustin, R.M., 2007, Impact of mass balance calculations on adsorption capacities in microporous shale gas reservoirs: Fuel, v. 86, p. 2696-2706.

Roussel, N.P., and Sharma, M.M., 2010, Optimizing Fracture Spacing and Sequencing in Horizontal Well Fracturing: SPE International Symposium and Exhibiton on Formation Damage Control, 127986.

Schorlemmer, D., and Woessner, J., 2008, Probability of Detecting an Earthquake: Bulletin of the Seismological Society of America, v. 98, p. 2103-2117.

Settari, A., and Mourits, F.M., 1998, A Coupled Reservoir and Geomechanical Simulation System: SPE Journal, v. 3.

Settari, A., and Walters, D.W., 2000, Reservoir Geomechanics: New approach to reservoir engineering analysis and a powerful tool for reservoir management: 16th World Petroleum Congress, 30137.

Shemeta, J., and Anderson, P., 2010, It's a matter of size: Magnitude and moment estimates for microseismic data: The Leading Edge, v. 29, p. 296-302.

Smith, M.B., 1985, Stimulation Design for Short, Precise Hydraulic Fractures: SPE Journal, v. 25, p. 371-379.

Sneddon, I.N., 1946, The Distribution of Stress in the Neighbourhood of a Crack in an Elastic Solid: Proceedings of the Royal Society of London. Series A. Mathematical and Physical Sciences, v. 187, p. 229-260.

Soliman, M.Y., and Boonen, P., 2000, Rock mechanics and stimulation aspects of horizontal wells: Journal of Petroleum Science and Engineering, v. 25, p. 187-204.

Soliman, M.Y., East, L., and Adams, D., 2008, Geomechanics Aspects of Multiple Fracturing of Horizontal and Vertical Wells: Spe Drilling & Completion, v. 23, p. pp. 217-228.

Sondergeld, C.H., Ambrose, R.J., Rai, C.S., and Moncrieff, J., 2010a, Micro-Structural Studies of Gas Shales: SPE Unconventional Gas Conference, 131771.

Sondergeld, C.H., Newsham, K.E., Comisky, J.T., Rice, M.C., and Rai, C.S., 2010b, Petrophysical Considerations in Evaluating and Producing Shale Gas Resources: SPE Unconventional Gas Conference.

Sone, H., and Zoback, M.D., 2010a, Strength, Creep And Frictional Properties of Gas Shale Reservoir Rocks: 44th U.S. Rock Mechanics Symposium and 5th U.S.-Canada Rock Mechanics Symposium, 10-463.

Sone, H., and Zoback, M.D., 2010b, Stress heterogeneity observed in Barnett Shale, TX, and its relation to the distribution of clay-rich ductile formations: AGU Fall Meeting.

Sprenke, K.F., Stickney, M.C., Dodge, D.A., and Hammond, W.R., 1991, Seismicity and tectonic stress in the Coeur d'Alene mining district: Bulletin of the Seismological Society of America, v. 81, p. 1145-1156.

Texas Railroad Commission, 2010, Texas Gas Well Gas Production in the Newark, East (Barnett Shale) Field - 1993-2009.

Trifu, C., Ioan, Urbancic, T.I., and Young, R.P., 1993, Non-similar frequency-magnitude distribution for M < 1 seismicity: Geophysical Research Letters, v. 20, p. 427-430.

Urbancic, T.I., and Maxwell, S.C., 2002, Source Parameters of Hydraulic Fracture Induced Microseismicity: SPE Annual Technical Conference and Exhibition, 77439-MS.

Urbancic, T.I., Shumila, V., Rutledge, J.T., and Zinno, R.J., 1999, Determining hydraulic fracture behavior using microseismicity: Vail Rocks 1999, The 37th U.S. Symposium on Rock Mechanics (USRMS), 99-0991.

von Seggern, D.H., Brune, J.N., Smith, K.D., and Aburto, A., 2003, Linearity of the Earthquake Recurrence Curve to M < -1 from Little Skull Mountain Aftershocks in Southern Nevada: Bulletin of the Seismological Society of America, v. 93, p. 2493-2501.

Waldhauser, F., and Ellsworth, W.L., 2000, A Double-Difference Earthquake Location Algorithm: Method and Application to the Northern Hayward Fault, California: Bulletin of the Seismological Society of America, v. 90, p. 1353-1368.

Walls, J., and Nur, A., 1979, Pore pressure and confining pressure dependence of permeability in sandstone: 7th Formation Evaluation Symposium, Can. Well Logging Soc.

Wang, F.P., and Reed, R.M., 2009, Pore Networks and Fluid Flow in Gas Shales: SPE Annual Technical Conference and Exhibition, 124253-MS.

Warpinski, N., 2009, Microseismic Monitoring: Inside and Out: SPE Journal of Petroleum Technology, v. 61, p. 80-85.

Warpinski, N.R., and Branagan, P.T., 1989, Altered-Stress Fracturing: SPE Journal of Petroleum Technology, v. 41, p. 990-997.

Warpinski, N.R., Branagan, P.T., Peterson, R.E., Wolhart, S.L., and Uhl, J.E., 1998, Mapping Hydraulic Fracture Growth and Geometry Using Microseismic Events Detected by a Wireline Retrievable Accelerometer Array: SPE Gas Technology Symposium, 40014-MS.

Warpinski, N.R., and Teufel, L.W., 1992, Determination of the Effective-Stress Law for Permeability and Deformation in Low-Permeability Rocks: SPE Formation Evaluation, v. 7, p. 123-131.

Warpinski, N.R., Wolhart, S.L., and Wright, C.A., 2004, Analysis and Prediction of Microseismicity Induced by Hydraulic Fracturing: SPE Journal, v. 9, p. 24-33.

Warren, B.E., 1969, X-ray diffraction: Reading, Mass., Addison-Wesley.

Waters, G.A., Dean, B.K., Downie, R.C., Kerrihard, K.J., Austbo, L., and McPherson, B., 2009, Simultaneous Hydraulic Fracturing of Adjacent Horizontal Wells in the Woodford Shale: SPE Hydraulic Fracturing Technology Conference.

Waters, G.A., Heinze, J.R., Jackson, R., Ketter, A.A., Daniels, J.L., and Bentley, D., 2006, Use of Horizontal Well Image Tools to Optimize Barnett Shale Reservoir Exploitation: SPE Annual Technical Conference and Exhibition.

Wiemer, S., 2001, A Software Package to Analyze Seismicity: ZMAP: Seismological Research Letters, v. 72, p. 374-383.

Williams-Stroud, S., 2008, Using Microseismic Events to Constrain Fracture Network Models and Implications for Generating Fracture Flow Properties for Reservoir Simulation: SPE Shale Gas Production Conference.

Zhang, H., and Thurber, C.H., 2003, Double-Difference Tomography: The Method and Its Application to the Hayward Fault, California: Bulletin of the Seismological Society of America, v. 93, p. 1875-1889.

Zhao, H., Givens, N.B., and Curtis, B., 2007, Thermal maturity of the Barnett Shale determined from well-log analysis: AAPG Bulletin, v. 91, p. 535-549.

Zoback, M.D., Barton, C.A., Brudy, M., Castillo, D.A., Finkbeiner, T., Grollimund, B.R., Moos, D.B., Peska, P., Ward, C.D., and Wiprut, D.J., 2003, Determination of stress orientation and magnitude in deep wells: International Journal of Rock Mechanics and Mining Sciences, v. 40, p. 1049-1076.

Zoback, M.D., and Byerlee, J.D., 1975, Permeability and Effective Stress: AAPG Bulletin, v. 59, p. 154-158.

Zoback, M.D., Kitasei, S., and Copithorne, B., 2010, Addressing the Environmental Risks from Shale Gas Development.